ADDIS ABABA UNIVERSITY
SCHOOL OF GRADUATE STUDIES
SCHOOL OF EARTH SCIENCES

MAGMATIC EVOLUTION OF BOKO MAGMATIC COMPLEX, MAIN ETHIOPIAN RIFT, USING PETRO-CHEMICAL APPROACH AND CO_2 FLUX MEASUREMENT

BY

AMDEMICHAEL ZAFU TADESSE

A thesis submitted to the School of Graduate Studies of Addis Ababa University in partial fulfillment of the requirements for the degree of Master of Science in Earth Sciences (Petrology)

July 2016
Addis Ababa, Ethiopia

ADDIS ABABA UNIVERSITY
SCHOOL OF GRADUATE STUDIES
SCHOOL OF EARTH SCIENCES

MAGMATIC EVOLUTION OF BOKO MAGMATIC COMPLEX, MAIN ETHIOPIAN RIFT, USING PETRO-CHEMICAL APPROACH AND CO_2 FLUX MEASUREMENT

BY

AMDEMICHAEL ZAFU TADESSE

ADVISOR: DEREJE AYALEW (Prof.)

A thesis submitted to the School of Graduate Studies of Addis Ababa University in partial fulfillment of the requirements for the degree of Master of Science in Earth Sciences (Petrology)

July 2016
Addis Ababa, Ethiopia

ADDIS ABABA UNIVERSITY
SCHOOL OF GRADUATE STUDIES
SCHOOL OF EARTH SCIENCES

MAGMATIC EVOLUTION OF BOKO MAGMATIC COMPLEX, MAIN ETHIOPIAN RIFT, USING PETRO-CHEMICAL APPROACH AND CO_2 FLUX MEASUREMENT

BY

AMDEMICHAEL ZAFU TADESSE

Approved by the Examining Committee

Dr. Balemwal Atnafu	_____	_____
Head, School of Earth Sciences	Signature	Date
Prof. Dereje Ayalew	_____	_____
Advisor	Signature	Date
Prof. Gezahegn Yirgu	_____	_____
Examiner	Signature	Date
Dr. Mulugeta Alene	_____	_____
Examiner	Signature	Date

Declaration of Originality

I hereby declare that the thesis is my original master's degree work under the supervision of Prof. Dereje Ayalew, School of Earth Sciences, Addis Ababa University during the year 2016. I further declare that this work has not been presented or submitted to any other university or institution for the award of any degree or diploma. All sources and materials used for the thesis have been duly acknowledged.

Amdemichael Zafu Tadesse _____ _____

Signature Date

This is to certify that the above declaration made by the candidate is correct to the best of my knowledge.

Prof. Dereje Ayalew (Advisor) _____ _____

Signature Date

Abstract

Boko magmatic complex is situated in transitional zone between Central and Northern MER segments. The area is located approximately 92.02 Km from Addis Ababa. The main objective of the research study is to understand the magmatic evolution and the extent of the main collapse zone of the complex. To meet the objectives, starting from the beginning different methods have been applied. The methods are; remote sensing, field observation, petrography, structural data analysis, geochemistry and soil CO_2 degassing. The Boko magmatic complex is characterized by two main phase of eruption; Boko caldera forming eruptive activity and post caldera eruptive activity. These episodes give volcanic products that constitute the complex. The major volcanic units are rhyolitic lava flow, pumice flow, ignimbrite, lower pumice fall, rhyolitic lava dome, obsidian, lower basalt, upper ash flow, scoria and upper basalt. The surface thermal manifestation and anomalous CO_2 degassing suggests Boko has currently active volcanic activity beneath the volcano. The volcanic products are affected by extensional tectonics which is manifested by appearance of geological structures like, joint and NNE-SSW trending major normal faults. The geochemical analysis results indicates the Boko rocks are bimodal in composition, mafic and silicic, lacking intermediate composition. The mafic rocks are transitional to weakly subalkaline basalt and the silicic rocks are dominantly peralkaline rhyolites. The two groups of rocks are co-genetic and related to each other by fractional crystallization process starting from mantle-derived basaltic magma with slight crustal material involvement. The soil CO_2 degassing measurement result shows that it has biogenic and volcanic-hydrothermal source. The total flux from the two sources is 74.71 t d^{-1}. The mean of CO_2 flux from the biogenic source is 0.041 g m^{-2} d^{-1} and from volcanic-hydrothermal origin is 2.14 g m^{-2} d^{-1}. The combination of remote sensing, soil CO_2 flux value distribution, field observations and structural data analysis suggest the main collapse zone of Boko Caldera has elliptical geometry with a dimension of 6 Km (E-W) by 4 Km. The major caldera axis is along E-W which is in agreement with the Main Ethiopian Rift regional stress direction.

Key words: Boko Magmatic Complex, Fractional crystallization, Crustal contamination, CO_2 degassing, Caldera forming eruption, Caldera collapse and Main collapse area.

Acknowledgment

This research work is done by contribution of different organizations and individuals. Firstly I would like to give my sincere gratitude to Addis Ababa University School of Earth Sciences for providing an opportunity to study my master's degree and funding the research project.

My second deepest gratitude goes to my advisor Prof. Dereje Ayalew for his follow up, constructive comment, valuable suggestion, encouragement and tireless support. Prof. Gezahegn Yirgu is the second person to give my respect and acknowledgement for having valuable technical discussion with him and guidance; it's really meant a lot to me. The geochemical samples are analyzed and the PP system gas analyzer is provided by the support of Action Marge research project, France. I want to express my deepest sincere thanks for Prof. Pik Raphael for facilitating things in order to reach the geochemical analysis result on time. My gratitude also extends to the former and current School of Earth Sciences chairman Dr. Siefu Kebede, Dr. Balemwal Atnafu and all academic staff of the School.

During the research work I got a lot of support from my friends, colleagues and volcanology team from university of Oxford specially Mr. Bahru Zinaye, Mr. Samuel Getachew, Dr. Biniam Tesfaw, Mr. Wendwossen Sisay, Dr. Karen Fontijn, Dr. William Hutchison and Prof. Tamsin Mather. I ran out of words to express my great appreciation and gratitude for your critical support from the beginning to the end of this project work.

My acknowledgement goes to my family for giving me courage and unforgettable support while I'm in the project work. The last but not the least my gratitude goes to government officials and local peoples of Adama woreda for allowing and helping me during the field work.

Table of Contents

List of Figures

List of Tables

List of Acronyms

a.s.l	above sea level
BMC	Boko Magmatic Complex
CIPW	Cross, Iddings, Pirsson and Washington
CRPG	Centre de Recherché Petrographiques et Geochimiques
DDS	Diffuse Degassing Structures
DEM	Digital Elevation Model
EAGL	Ethiopia Afar Geoscientific Lithospheric Experiment
EARS	East African Rift System
EGM+4	Environmental Gas Monitor versions plus four
ENVI	ENvironment for Visualizing Images
ETM+	Enhanced Thematic Mapper Plus
GPS	Global Positioning System
GSA	Graphical Statistical Approach
HREE	Heavy Rare Earth Element
ICP-MS	Inductively Coupled Plasma Mass Spectroscopy
ICP-OES	Inductively Coupled Plasma Optical Emission Spectroscopy
LOI	Loss of Ignition
LREE	Light Rare Earth Element
MER	Main Ethiopian Rift
NDVI	Normalized Difference Vegetation Index
PPL	Plane Polarized Light
REE	Rare Earth Element
SGeMS	Stanford Geostatistical Modeling Software
SRC-1	Soil Respiration Chamber version 1
TAS	Total Alkali Silica
WFB	Wonji Fault Belt
XPL	Cross Polarized Light
YTVL	Yerer-Tullu Wellel Volcano-tectonic Leneament

Chapter One

1. Introduction

1.1. Background

Continental rift zones are sites of lithospheric stretching, which occurs in response to far-field plate forces like slab pull, ridge push and tractions at the lithosphere-asthenosphere boundary induced by mantle flow (Ring, 2014). The extension of the crust is achieved through normal faulting that thins the brittle crust. Dense lithospheric mantle rocks rise upward to replace the thinning crust (Weissel and Karner, 1989).

Ring (2014) imply that the East African Rift System (EARS) can be taken as the model example of a continental rift. Eduard Suess was probably the first to realize that the EARS is a result of continental extension and thinning of the crust (Ring, 2014). The EARS is a 5,000 km long series of fault-bounded depressions that marks divergent boundary between two major tectonic plates, Somalia and Nubia (Calais et al., 2006). It is connected to the world wide system of oceanic rifts via the Afar Triangle to the Gulf of Aden and Red Sea (Morley, 1999 see on Fig.1.1). Stamps et al. (2008) suggests that the initial stages of rift development in East Africa are characterized by a series of strongly asymmetric graben, which are typically some 40 to 50 km wide and 60 to 120 km long and open at rates of ~3 mm/yr. Rifting of East Africa in the last 13 My can be grouped into two branches, the Eastern and Western branches (Macgregor, 2015*;* Morley, 1999 see Fig.1.1). The EARS eastern branch rifts extend continuously from the Afar of Ethiopia to northern Tanzania.

Previous works (e.g., Ebinger et al., 2000) suggest Main Ethiopian Rift (MER) within the EARS represents the link region between the Afar triple junction and Turkana rift in Kenya where extensional deformation start to develop in late Oligocene-early Miocene times. The MER is ~80 km wide (Mohr, 1983b) and separates the uplifted western (Ethiopian) and eastern (Somalian) plateaus. The MER is divided into three main segments; Northern, Central and Southern (Corti, 2009; Mohr, 1983b; Gidey Woldegabriel et al., 1990; Hayward and Ebinger, 1996). These segments reflect different

stages of the continental extension process that are interpreted from different fault architecture, timing of volcanism and deformation, crustal and lithospheric structure (e.g., Hayward and Ebinger, 1996).

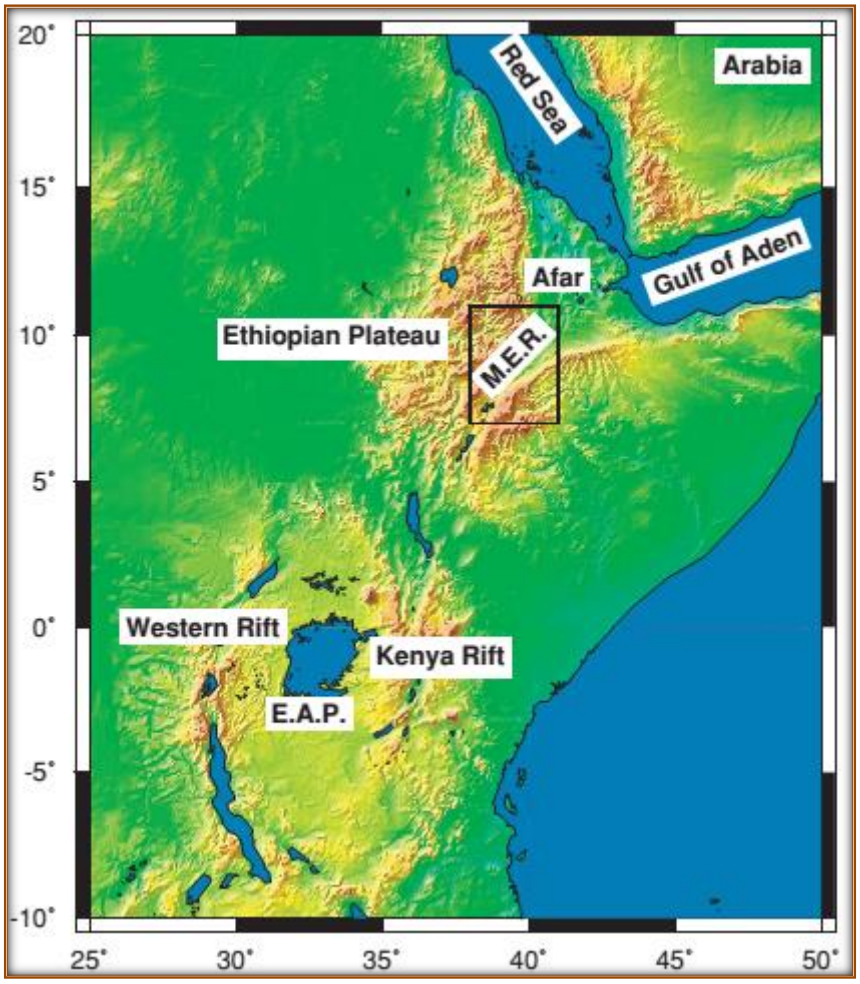

Figure 1.1: *Regional map of the East African Rift. E.A.P stands for East African Plateau and M.E.R for Main Ethiopian Rift on which the study area is located. (Maguire et al., 2005 pp. 270).*

Mulugeta Dugda et al. (2007) advocates' African super plume located in the lower mantle beneath southern Africa is the main extensional force for rifting in the overall East Africa; that persists in the last 30 Ma. Thinning and weakening lithosphere leading to reactivation of pre-existing weakness that eventually becomes departed in to different blocks. In the MER, according to Corti (2009), deformation started in the Early Miocene (20–21 Ma) in the Southern MER sector. This is interpreted as northward propagation of the Kenya rift; rift propagation from different sector in MER is the main debate in recent research; e.g., Wolfenden et al. (2004); Gidey Woldegabriel et al. (1990); Bonini et al. (2005); Rooney et al. (2007). This event lasted until 11 Ma, and then deformation decreased drastically

(Bonini et al., 2005). During this time (from Early Miocene to 11 Ma) no major extensional deformation undertaken in the Central and Northern MER. During initiation of rifting in the MER there is activation of long, widely spaced and large offset boundary faults. This large offset border fault system developed along the rift between 11 and 6 Ma, has been mostly active until 2 Ma (Corti, 2009). Keir et al. (2006), from historic and local seismicity pattern, suggests $N45^0E$ trending border faults are currently inactive. The rifting is associated with diffuse bimodal volcanism that gives Mio-Pliocene aged volcanic product. According to Corti (2009) at 2 Ma, drastically the deformation style changed from boundary fault in to right stepping arrangement of dense swarms of Wonji Fault Belt (WFB). This shift in deformation style corresponds with Quaternary volcanic activity on the rift floors. Several different models have been applied to explain the deformational shifting from Border fault to WFB (eg., Wolfenden et al., 2004).

Volcanism generally occurred in the MER in two phases. In the first phase wide spread volcanism that mainly localized along boundary fault systems. In the second is Quaternary volcanism occurred at the end of Pliocene due to new activation of Wonji fault belt.

1.2. Geographic setting of the Study Area

1.2.1. Location and Accessibility

This research project is conducted in the MER, in a transitional zone between the Central and Northern MER segments. The research area lies on the Dera and Nazret Sub-sheet with sheet number 0839 C2 and 0839 A4 according to topographic map distribution of Ethiopian Mapping Agency (EMA). The area is located about 92.02 Km far from Addis Ababa and 2.32 Km from the center of Nazret town (or Adama that is the largest city of the Oromia Region) in south east direction. In UTM (Universal Transverse Mercator) the area is bounded by a grid of Easting from 529000 to 539000 m and Northing of 933000 to 942000 m (Fig.1.2). The study area has coverage of approximately 90 Km^2.

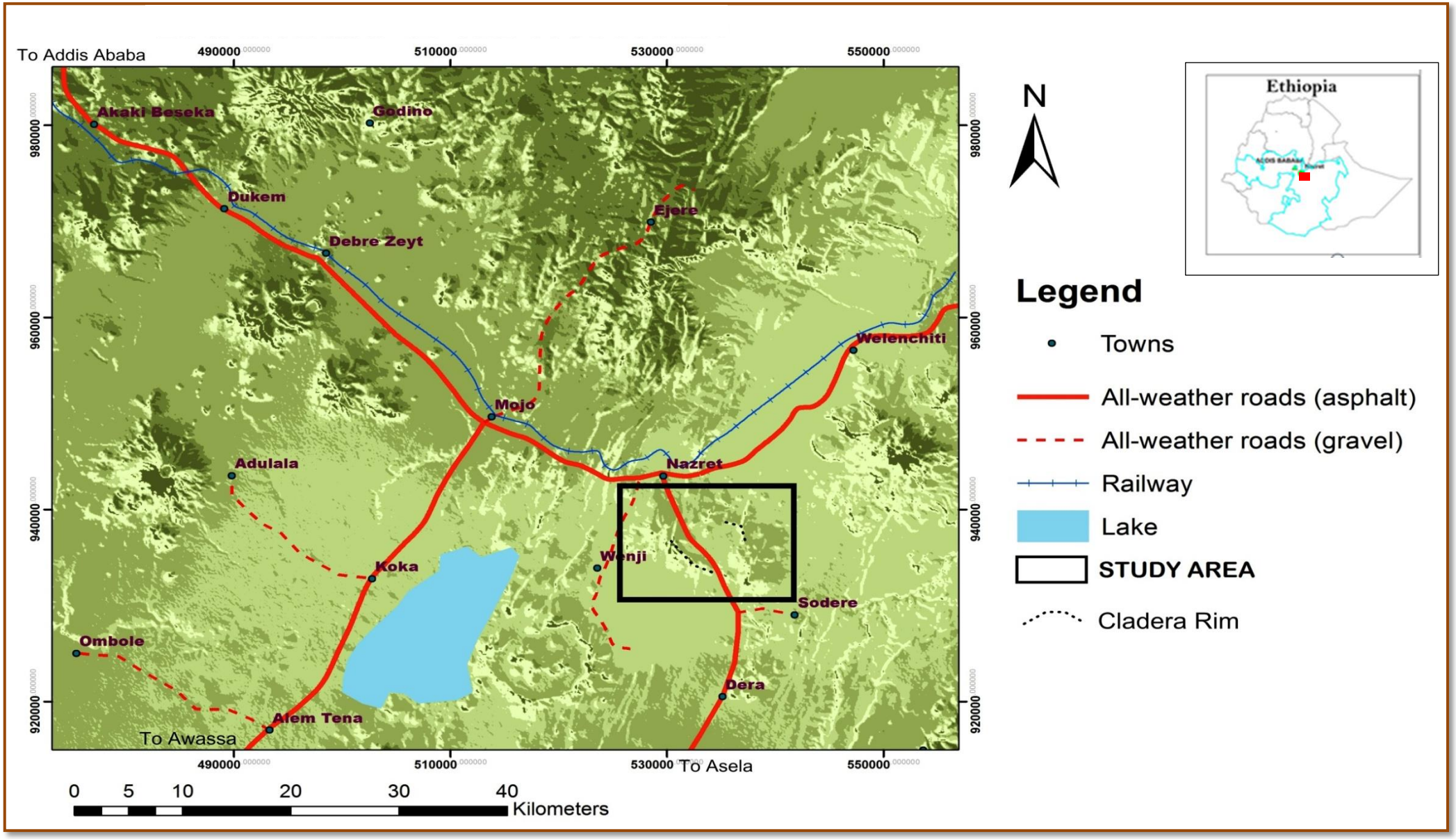

Figure 1.2: *Location map of the study area*

The study area is nearly divided equally into two, toward north east and south west, by a main road that runs from Nazret (or Adama) to Awash Melkasa town. This main road makes the study area easy to access using a vehicle. Further to the east and west of the study area there are foot trails developed by the local peoples for their day to day activity. This foot trails help to access the portion of the study area that is located far away from the main road. In addition to the foot trails some gravel roads are constructed for raw material transportation from quarries of scoria and pumices. That makes the area more accessible.

1.2.2. Physiography and Drainage

The studied area is located in the central part of the MER. The enormous volcanic and tectonic activities that took place in the Quaternary period (Boccaletti et al., 1998) created distinct physiographic groups in the study area identified as the mountain, ridges and cliff blocks bounding the caldera floor (which is flat land see on Fig.1.3).

The ridges and cliff blocks are characterized by big faults, each producing a steep fault escarps and flat top domes ranging from 1860 m above sea level (a.s.l) to 1,660 m a.s.l (Fig.1.3). In contrast, the extensional rifting and the caldera collapse form a downward throw of a flat landmass of about 1,600 m a.s.l. The caldera floor is the main portion of the geographic land aimed at cultivating crops for the local people. The caldera rim and the fault scarps are transitional land between ridges and caldera floor characterized by a gentle slope with elevation ranging from 1,700 to 1,860 m a.s.l. The caldera floor is characterized by having numerous scoria cones those are elliptical in geometry with NNE-SSW major axis direction.

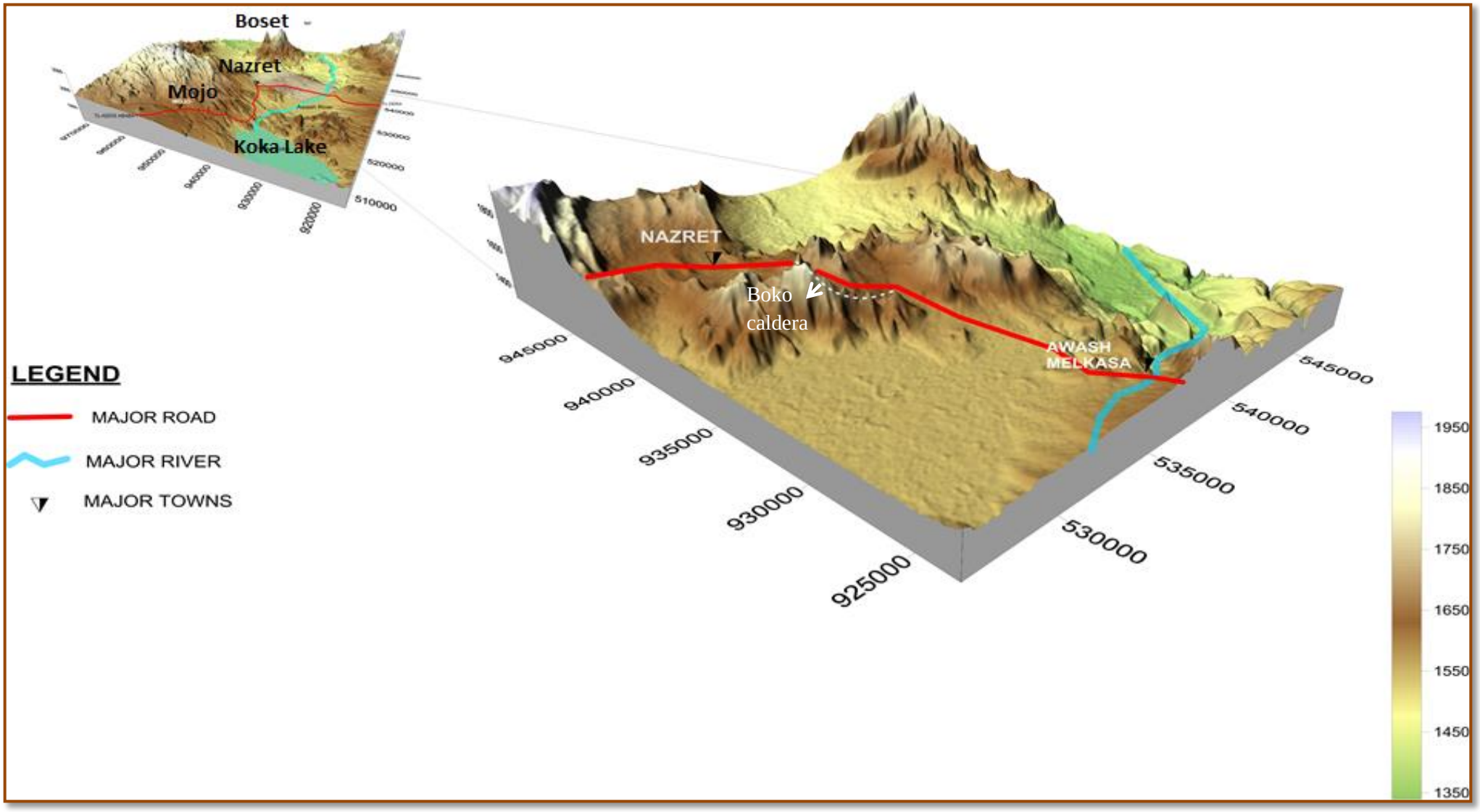

Figure 1.3: *Physiographic map of the Boko volcano region.*

The area is located in Adama-Wonji drainage basin which has a main feature of intersecting and interrupting features of several fault systems with intermingled volcanic products. The geological and structural aspects of the area make the drainage pattern complex. The network of the streams is dendritic (Fig.1.4). This is due to flow of streams from the elevated areas toward a low land, especially the caldera floor. Some stream lines show a parallel drainage pattern by following the WFB along NNE-SSW direction. The streams (almost all of them) are seasonal; which is filled by water only on the rainy season.

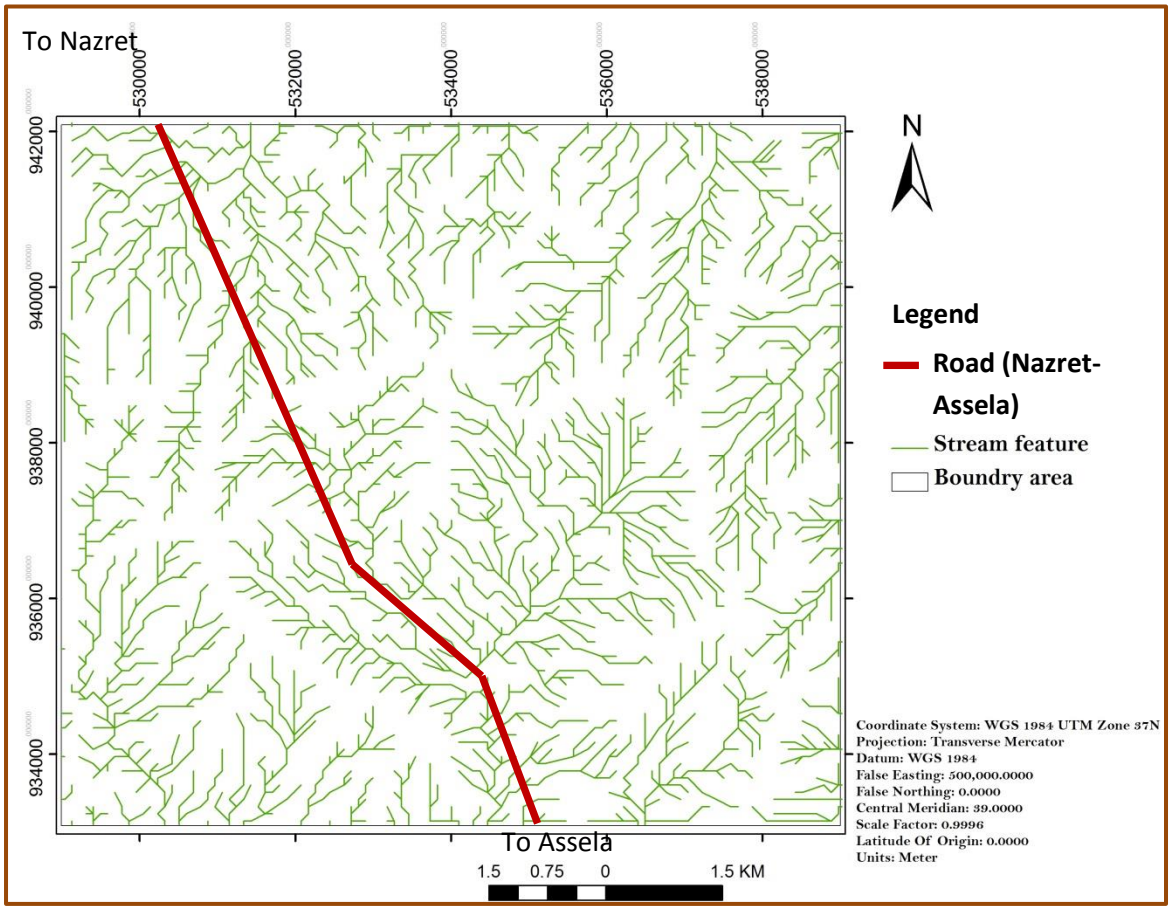

Figure 1.4: *Drainage pattern map of the Boko volcanic area.*

1.2.3. Climatic condition and Vegetation

The climate around the area of the study shows a tropical condition. The climatic condition of the area is mainly expressed by average temperature and average precipitation. According to Climate-Data.org in http://en.climate-data.org/location/2108/ the daily average high temperature is 30.1 ^{o}C measured during April while the low

temperature is 10.6 ^{o}C during December (see on Fig.1.5). The average annual precipitation becomes high during the August (210 mm) and low during December (7 mm). Generally the climatic condition around the study area is very hot during the day time and become slightly chilly and windy during the evening.

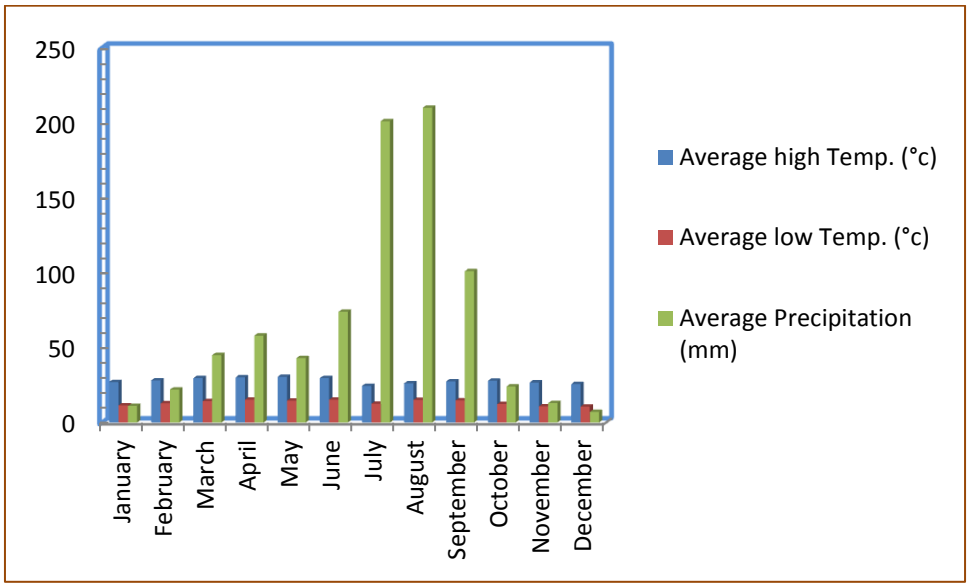

Figure 1.5: *A bar chart that show climatic condition of area around Nazret. Sourced from Climate-Data.org in http://en.climate-data.org/location/2108/.*

The vegetation distribution is mainly dependent on the climatic condition of the area. As explained on the above paragraph, the climate is characterised as tropical. On this type of climate vegetation is scarce and unique types of vegetation are present. The typical example that occurred in the area is Shrubs, Acacia (Grar) and Eucalyptus (Bahirzaf). Eucalyptus is grown by the local people in soil conservation program that is mainly applied in the MER to protect the soil from erosion. The local people cultivate some types of crops on the gentle slope landmass that is especially on the caldera floor. The common types of crops cultivated in the area are Teff, Wheat, Barley, Sorghum and Maize. The harvesting season is between October and December at which the rainfall becomes lower in amount. In addition to the trees and crops cultivated by the local people a Sugar cane plantation cover some portion of the study area which is planted by Wonji Sugar factory.

1.2.4. Population and Settlement

The population density in the area is low. The closest big town to the study area is Nazret and there are small villages like Adulala, Enyur and Kersa that are found within the study area. These small villages that are found in the center of the study area have small number of population relative to Nazret town. Small portion of the study area superposed with the administrative boundary of the town, Nazret. Based on the 2007 Census conducted by the Central Statistical Agency of Ethiopia (CSA), Nazret rural and urban area has a total population of 220,212. The four largest ethnic groups in the area were the Oromo (39.02%), the Amhara (34.53%), the Guraghe (11.98%) and the Silte (5.02%): all other ethnic groups made up 9.45% of the total population. Amharic is spoken as a first language by 59.25%, 26.25% spoke Oromiffa and 6.28% spoke Guragiegna. The majority of the inhabitant beliefs are Ethiopian Orthodox, Muslim and Protestant religion.

1.3. Problem statement

The MER is an area where tectonic and magmatic evolution is studied by different scholars, who have different fields of specialization. In spite of the extensive studies, many scientific problems remain satisfactorily unsolved. For instance, after widespread Miocene-Pliocene volcanism, the Quaternary magmatic activity became mostly localized on the rift axis, with products showing a typical bimodal composition (dominantly basaltic and rhyolitic composition). The compositional gap (Daly gap) of these volcanic rocks remains a poorly understood aspect of the rift-related magmatism (e.g., Gasparon et al., 1993; Peccerillo et al., 2003; 2007; Rooney et al., 2007). This controversy leads different authors to different ways of modeling the petrogenesis (see section 1.7 for further elaboration). In addition to this there is no agreement among scholars on the origin of silicic rocks and their relation to mafic rocks (Peccerillo et al., 2007). Explaining the daily gap is beyond the scope of this work. This study is motivated by the controversy related to genesis and relationship between the two groups of rocks.

The second issue is that of volcanic hazard from active MER volcanoes. According to Aspinall et al. (2011) significant knowledge gaps exist regarding the past and current activity of the silicic peralkaline volcanoes of the MER. Large caldera forming eruption that happen on volcanoes like Gedemsa, Aluto, Kone and Fant'Ale have been studied on

their eruptive history and geochemical characteristics to some extent, but others, like the BMC, have not been studied in detail.

1.4. Objectives

1.4.1. General Objective

The main objective of this research study is to better understand the magmatic evolution and the extent of the main collapse zone of the Boko magmatic complex (BMC) located in the central section of the MER.

1.4.2. Specific Objectives

- To produce a geological map at a scale of 1:25,000 that elucidates the distribution of major lithological units and major geological structures.
- To construct a composite volcanic stratigraphy (rock succession) of the magmatic complex.
- To characterize major and trace elements signature of rocks that constitutes the BMC.
- To determine the petrogenesis of the silicic rocks.
- To quantify the total amount of CO_2 degassing and major sources of the CO_2.
- To analyze and synthesize different geological structures those are found in the area and,
- Finally to outline the caldera edifice main collapse area.

1.5. Methodology

1.5.1. Introduction

The overall works of the research are mainly divided into three phases; pre-field work, field work and post-field work. In the pre-field work assessment on literatures about the methods that would be applied and about the study area accessibility, extent..etc are done. During field work and post-field work collecting, analyzing, synthesizing, presenting and interpreting of data are done. Two types of data are collected for the research; secondary and primary data.

During the preparatory stages of the fieldwork, a logistic plan is made, and major geological structures are delineated and different lithologies are differentiated by using ArcGIS and ENVI software by using Landsat ETM+ satellite image. Data collected during the field work include structural data, CO_2 flux distribution on soil, rock physical characteristics and collection of representative samples from each encountered variety of lithologies.

After collecting data the next step is to analyze those relevant data. Most analyses are done in the laboratory. The samples collected from the field work are prepared for two purposes. The first purpose is for geochemical analysis and second is for the petrographic study. Data synthesis involves collecting and integrating different data sets into coherent information for interpretation. A fundamental aspect in this study is geological mapping at a scale of 1:25,000. The other means to synthesize data are using software package like Stereonet for geological structures, Petrograph beta or/and Microsoft excel for geochemical data and SGeMS for CO_2 flux distribution.

All data, including both collected during this study and those from literature, are been analyzed, interpreted and presented together. The presented data is been put into a regional context by comparing relevant literature on nearby or similar volcanic centers. All collected data and a discussion of the interpretation is finally being written up in a final thesis report.

During the different phases, a variety of tools are used, including topographic and geological maps at a scale of 1:50,000, PP system, standard field sampling and measuring tools, and ArcGIS, ENVI, Google earth, Global mapper, Petrograph beta, Strater, SGeMs and Stereonet software packages. In the following sections the main methods that applied in the research work is presented.

1.5.2. Field work and Geological mapping

In addition to the secondary data that originate from different sources that existed before this research; primary data are used. The main way of collecting the primary data is by means of field work. The field work had two phases. The first phase of the field work is undertaken between October 05 to October 25/2015. The main aim of this field work is to

know the distribution of the lithologies and geological structures (both vertically and horizontally) and to take representative samples for further laboratory analysis (especially for petrographic and geochemical analysis). The lithology variation and geological structures are transferred to a geological map of scale 1:25,000. The geological mapping is undertaken by following traverses and based on visible outcrops.

The second phase of the field work was done in between February 10 to February 22/2016. These fieldwork aims to collect data about the soil degassing of CO_2 on the diffuse degassing structures. The measurement is done by following preplanned GPS points and systematic sampling method. The second aim is to check the stratigraphy of the rocks by considering the laboratory results of the geochemical and petrographic analysis.

1.5.3. Laboratory and Data analysis

A) Geochemical sampling, analysis and data presentation

Geochemical samples are collected in the first phase of the field work which is discussed in section 1.5.2. The sample preparation for geochemical analysis includes making a rock powder after removing the weathered part of the rock. To do this three steps has been followed; the first step is to remove the weathered part from the surface of the rock sample and break it in to desirable sizes, the second step is to crush the broken fresh sample in a jaw crusher and finally the crushed sample will be milled down to micron-size particles in an agate ball automatic milling machine. The sample preparation is done in Addis Ababa University School of Earth Sciences Mill room. To minimize cross contamination of samples, after crushing and milling every single rock sample, the Jaw crusher and the ball mills are blown by an air compressor and washed out to remove any possible contaminant, then dried to continue with the second sample. The samples of felsic are prepared first then after finishing all felsic rocks the mafic rocks are prepared. In case of ignimbrite after crushing, the rock fragments is sorted manually to minimize the introduction of the lithic fragment to the final analyze (powdered sample) before going to the milling process.

The powdered rock samples are thirty (30) in number. These samples are sent to a commercial laboratory called Centre de Recherché Petrographiques et Geochimiques (CRPG) in Nancy, France for determinations of major and trace element concentration of the prepared samples. The elemental composition of each rock samples were determined using Inductively Coupled Plasma Optical Emission Spectroscopy (ICP-OES) and Inductively Coupled Plasma Mass Spectroscopy (ICP-MS).

B) Petrographic analysis

Ten thin section samples are prepared in School of Earth Science at Addis Ababa University thin section laboratory and sample examination undertaken in the School petrology laboratory. The thin section samples are selected based on the variety of the lithologies, their importance and their ambiguities to identify while in the field work.

The main output of the thin section analysis is modal proportion of minerals, largest grain size diameter along their longest dimension of each mineral, the average grain shape of those existed minerals and grain to grain relationship of the phenocrysts. This information will help lastly in the rock classification and understanding the magmatic evolution.

C) Structural data analysis

Structural data are collected during the first and second phase of the field work. These data are mainly measured for structures such as faults, joints and flow banding by using Brunton compass and clinometer. The major structures like fault are also visible and easily delineated in a satellite image. The collected structures are portrayed on the geological map at a scale of 1:25,000 and those data are synthesized by an easy software package called Stereonet.

1.5.4. Remote Sensing and GIS

In this study remote sensing and GIS is mainly applied for presenting-identifying lithologies, geological structures and hydrothermal alteration zones distribution. Soil CO_2 and geochemical sample points are also presented by this method. For presentation of hydrothermal alteration zone, Landsat ETM+ image is used. The satellite image is downloaded from the link http://earthexplorer.usgs.gov/ that is taken on date February 26,

2015. The assumption is in hydrothermally altered zones there exist abundant hydroxyl-bearing minerals like clay that is assured during field work. Hydroxyl bearing minerals like clays have a major absorption feature around 1.9, 2.35 and 2.5 μm wavelength (Gupta, 2013). To enhance the spectral contrast, ratio is taken between different band range that help and successful in mapping alteration zones (Segal, 1983). Using the theoretical knowledge about the spectral properties of most rocks and minerals; ETM+ bands 5/7 ratio were selected for hydroxyl bearing mineral analysis, especially clay minerals. To crosscheck influence of vegetation on the spectral signature Normalized Difference Vegetation Index (NDVI) is developed. NDVI is the mostly used index in studying vegetation distribution and is calculated by the relationship:

$$NDVI=\frac{IR-R}{IR+R}$$; where IR is the infrared and R is the red band

In addition to presentation of data in two dimensions; analysis are made to understand the caldera main collapse zone. For this purpose Digital Elevation Model (DEM) data with 30 m resolution is used. The analyses are mainly done by using software packages; Global mapper11, Google earth and ArcGIS10.

1.5.5. Soil CO_2 Flux and Concentration

Hundred and sixty three (163) measurement points are taken for the CO_2 degassing study. For the measurement of soil CO_2 the sampling technique applied is preplanned GPS points and systematic sampling. The preplanned GPS points are mainly applied on areas that show a similar CO_2 concentration and flux but for areas that show a bit variation in the measurement the sample spacing is made a bit closer (up to 30 m). The preplanned GPS points have a sample spacing of 1 Km and 500 m. The 1 Km sample spacing is for areas those are expected to have lower measurement result and similar soil CO_2 flux and concentration. The expectation of similar soil CO_2 flux and concentration is mainly depend on remote sensing analysis, structural mapping and previous literatures done on the same geological condition (e.g. Hutchison et al., 2015). Areas which have highly affected by brittle structure will have high measurement result because of those structures will act as a conduit and make the lithology plus the soil more permeable and finally enable us to get high value; those are called diffuse degassing structures (DDS). DDS constitute drilling targets for geothermal energy exploitation, and can be accurately

mapped by CO_2 flux measurements. The 500 m sample spacing is applied mainly on fault zones. The non-systematic sampling is mainly applied on areas which show an erratic variation in the result.

The measurement is taken by the equipment called PP System. This equipment contains EGM+4 CO_2 gas analyzer and SRC-1 chamber. EGM+4 CO_2 analyzer is a non-dispersive, portable, infrared gas analyzer. For measuring soil CO_2 the system uses accumulation chamber method; which is within an inverted chamber placed on the soil surface. The accumulation method calculates CO_2 flux by placing a 200 mm diameter accumulation chamber on the soil surface and pressing it into the soil to obtain a seal (Chiodini et al., 1998). Gases flowing into the chamber are pumped to an infrared gas analyzer. The gases will pass down the sample cell. Gases with di-atomic molecules such as CO_2 strongly absorb photons in the infrared range. In the gas analyzer there is a sensor emplaced, that is sensitive to photons at 4.26 microns. The 4.26 microns infrared range is one region which has a strong absorption for CO_2. The measurement result given lastly with a unit of ppm. After every measurement the equipment has an "Auto-Zero" feature which occurs at regular intervals, allows for fast warm-up, adaptation to changing ambient conditions and excellent stability of the CO_2 signal. The action of auto-zeroing minimizes the effects on span (gas sensitivity) of sample cell contamination, source aging, changes in detector sensitivity and changes in pre-amplifier gain. For measuring the CO_2 fluxes the instrument use the chamber volume and area that is inserted manually to the system and concentration difference in the measuring spot.

After measurements are made, survey post processing has two key elements. Firstly, the identification of the biological background component of CO_2 flux, so this is not confused with the geothermal signal. The approaches used to identification of background flux is by the graphical statistical approach (GSA) that partitions separately distributed populations using log-probability plots (Chiodini et al., 1998) by SGeMS software package. Secondly, total CO_2 releases were calculated by multiplying the arithmetic mean value of CO_2 fluxes by the surveyed areas called Sichel's t estimator (after David, 1977).

The CO_2 soil flux and concentration is strongly influenced by external factors, such as the barometric pressure (atmospheric pressure, P_{atm}), the air and soil temperature and

humidity, the wind speed, the amount of rain and vegetation (Reimer, 1980). According to Chiodini et al. (1998) the influence of rainfall and soil humidity can be avoided by trying to work in dry periods, whereas possible changes in soil CO_2 flux induced by variable P_{atm} are almost inevitable. To minimize the effect of the environmental factor the month February, which has low humidity and precipitation is selected for the survey. The variation that can come from the wind speed is can be minimized by carefully placing the chamber in the soil during measurement that does not allow exchange of air with atmosphere during the measurement. The increment in instrument reading that is comes from vegetation abundance is minimized by taking measurement far from vegetated areas.

1.6. Expected outcome and Research relevance

As mentioned in the problem statement the Boko area has not been studied in the aspect of petrology and geochemistry in detail, and this will be the very first detail study on its petro-chemical characteristics. The main expected research outputs will be as follows:

- A clear volcanic stratigraphy of the area that is finally needed to interpret the volcanic history by taking BMC as a center.
- An interpretation, based on geochemical analyses, of the petrogenesis of the felsic rocks that are exposed in the area to determine whether the rock formed by fractional crystallization from basaltic melt, crustal melting or other processes?
- Characterize the current activity from CO_2 degassing and surface manifestations.
- The extent of the caldera main collapse zone.

The research study is mainly done for the partial fulfillment of my Master's degree in petrology. Furthermore, it has relevance to the scientific community by providing wealth information on the aspects listed on the above bulletin. It gives detailed geological study for BMC in the MER and may also be considered to explain the genesis of other peralkaline products, from various localities, whose origin has been enigmatic. Beside this it provide preliminary information for detail geothermal exploration that will be undertaken in the study area for the future.

1.7. Review of Previous Works

The MER which occupies the central part of the country is made of Pliocene to Quaternary aged volcanic products represented by fissural basaltic lava flows and acidic central volcanoes (Mohr, 1971). Many geological works in the MER have been done for the last decades. According to Tamiru Alemayehu and Vernier (1997) the axial part of the rift is dominated by acidic volcanoes that mainly erupted along NNE-SSW tectonic lines. The volcanoes are characterized by either a big volcano or collapsed circular caldera.

Among the numerous central silicic volcanoes, there are some previous works on the genetic relationship of the mafic and felsic volcanic products, stratigraphy and clear outline of the main collapse zone. On Corbeti (Hutchison, 2015; Di Paola, 1971), Aluto (Hutchison, 2015), Gedemsa (Dereje Ayalew et al., 2003; Peccerillo et al., 2003; Giordano et al., 2014), Kone (Rampey et al., 2010) and Fanta'Ale (Giordano et al., 2014) volcano are some examples of previous works. These major volcanoes are aligned in NNE-SSW direction in the axis of the rift.

From those different studies, lack of overlap and nesting of collapse structures and different volcanic product in each phase of the volcanism suggests the volcanism has independent collapse events. Besides these, the volcanism is strongly bimodal (Bekele Abebe et al., 2007). One of the explanations for the bimodal composition is made by Peccerillo et al. (2003; 2007); the silicic volcanoes have compositionally zoned magma chambers. In the magma chamber based on density peralkaline melt zones found on above and mafic melts on below. The peralkaline melt zones are commonly assumed to form a density barrier that prohibits mafic melts from reaching the surface (Hutchison, 2015). So the dense mafic melt is erupted when the zoned peralkaline melt found beneath the earth become weakened by faults and other structures. The other explanation is made by Trua et al. (1999) from major, trace and isotope geochemistry study; for the genesis of the huge volumes of peralkaline rhyolites must be explained by a two stage model. On the first stage small degree (~10%) of halogen fluxed melting of the basaltic lower crust followed by moderate degrees (~40%) of the low-pressure fractionation. Trua et al. (1999) argue that fractionation model generally accepted for small volumes of felsic rocks associated to basaltic centers of related to small caldera collapses in the MER.

Some works are done previously on the Central MER silicic volcanoes with respective of defining the main collapse zone of the caldera structures and understanding the recent activity (e.g. Hutchison et al., 2015; Rampey et al., 2010). In those studies surface mapping and remote sensing are used as a method. In addition to the two methods Hutchison et al. (2015) used CO_2 concentration and flux variation by insitu measurement along expected major ring faults that is not clearly visible from the surface mapping and satellite images.

A shallow knowledge exists in the respective of petrology and geochemistry about the BMC. The work done by Boccaletti et al. (1999) and a sketch map prepared by Alula Damte et al. (1992) are the only works that give some information on the distribution, stratigraphy, and geochemical property of BMC rocks in large scale. Alula Damte et al. (1992) did a geological map at a scale of 1:50,000 that reveal the lithologies and structures distribution of Nazret-Dera area. Boccaletti et al. (1999) studied the area based on the geological map done by Alula Damte et al. (1992) on Nazret-Dera and Bekele Abebe et al. (1998) on Asela-Ziway area that pointed out the chronologic volcanic succession of the rocks found in the overall area. The Nazret-Dera area is composed of older volcanic rocks that outcrop along the fault scarps of the eastern margin with an age of 1.8 Ma and named as Eastern margin unit. The Eastern margin unit is overlain by Quaternary volcanic products which can be correlated to the WFB volcanism (Wonji group). Boccaletti et al. (1999) identify seven geological units in Nazret-Dera area that are correlated with Wonji group and the authors named the overall volcanic product from the Boko caldera as Boku-Tede Unit.

In addition to petrological studies, there are few studies on the hydrological and geophysical characteristics that basically focus on the fluid dynamics of the ground water. Tamiru Alemayehu and Vernier (1997) work on the conceptual model on the fluid movement from depth. The geothermal fluids in the Boko area come to the surface along deep fractures. The fractures on the rhyolites are tension and laminar fractures that increase the permeability up to a minimum depth of 400 m.

Tamiru Alemayehu and Tigistu Haile (2008) did an integrated geophysical study involving thermal, magnetic, electrical, electromagnetic and gravimetric surveys on the Boko geothermal area. The purpose of the research work is to elucidate the geothermal

areal extent, controlling parameters and relation to major local geologic structures, as well as to map shallow thermal aquifers. Geophysical investigations have clearly mapped the shallow low resistivity zones that are likely to indicate the presence of thermal aquifers and the location of major faults that allow downward and upward fluid flow. From vertical electrical sounding and magnetic geophysical method, Tigistu Haile et al. (2000) advocate vapor-dominated geothermal fields are located on or close to volcanoes. This verifies that shallow magma chamber is their source. At the Boko field, hydrothermal alterations apparent on the ground extend to about 200 m at the site of the major fumarole activity.

1.8. Thesis Overview

The thesis is structured in six chapters. Chapter one gives general information about the area of study, the purpose and methods followed in the research. Second chapter provide a regional scale overview. Chapter three gives a detail description about the lithology and geological structures of the study area. In Chapter four geochemical data is presented, interpreted and the magmatic evolution of silicic rock of Boko volcano is modeled. In chapter five the soil degassing data is presented and the eruptive history is dealt to some extent. Eventually the main conclusion and recommendation for the future study is dealt in chapter six.

Chapter Two

2. Regional Geological Setting

2.1. East African Rift System (EARS)

East African Rift System (EARS) is one of the rifts found in earth that is important to study evolution of rifting (Gregory, 1896) and a site to study Anthropology and Archeology. Richard Leakey suggested (in Leakey, 1973) that the EARS is the "Cradle of Mankind" because most early hominid fossils have been found in rift sediments. Eduard Suess was probably the first to realize that the EARS is a result of continental extension and thinning of the crust (Ring, 2014). There is a confusion on the age range of rifts to use the term EARS. According to Chorowicz (2005) the term 'East African Rift System' tends to be applied only to rifts of Cenozoic age. In contrary Macgregor (2015) said that still the Cenozoic age contain three overlapping subsets; Oligocene, Mid-Miocene and Late-Miocene to recent. By combining the age subsets, he gives general name EARS 1 (Oligocene to Mid Miocene) and EARS 2 (Mid-Late Miocene to recent).

The general trend for the EARS is N-S, as illustrated in Fig.2.1, but there are other trends like NW-SE due to line of basement weakness (Klerkx et al., 1998). The EARS is a 5,000 km long series of fault-bounded depressions that marks divergent boundary between two major tectonic plates, Somalia and Nubia (Calais et al., 2006). It forms a narrow (50-150 Km wide) elongate system of normal faults that stretches 3500 Km in a sub meridian direction. It is connected to the world wide system of oceanic rifts via the Afar Triangle to the Gulf of Aden and Red Sea rifts (Morley, 1999). Ebinger et al. (1989) suggest that the topography of EARS, at a large scale, is characterized by lithospheric plateau (Afar and East African domes). The average altitude for the Afar dome is 1500 m and for the East Africa dome is 1200 m. They are separated by Turkana depression (600 m average altitude) in northern Kenya. Both domes have diameters of about 1000 Km (Bosworth et al., 1992).

Rifting in EARS on the last 13 My can be grouped into two branches: the eastern and western branches (Macgregor, 2015*;* Morley, 1999*)*. The EARS 2 eastern branch (see on Fig.2.1) rifts extend continuously from the Afar of Ethiopia to northern Tanzania. Ebinger et al. (2000) indicate that evidence for Paleogene to early Miocene rifting in Ethiopia confined to southern part of Ethiopia. In this area rifting started in late Oligocene-Early Miocene from reactivation of EARS 1 rifts (Zanettin et al., 1978; Bonini et al., 2005; Morley, 1999).

The western branch of the EARS 2 rifts extends from close to the Uganda/Sudan border, where it is linked to the eastern branch through the Aswa Fracture Zone (Fig.2.1), to the Indian Ocean at Beira in Mozambique (Ebinger et al., 1989). In comparison the trend of rifts in the western branch is less continuous than eastern branch. This is due to the periodically occurred magmatism in the eastern branch (Ebinger et al., 1993).

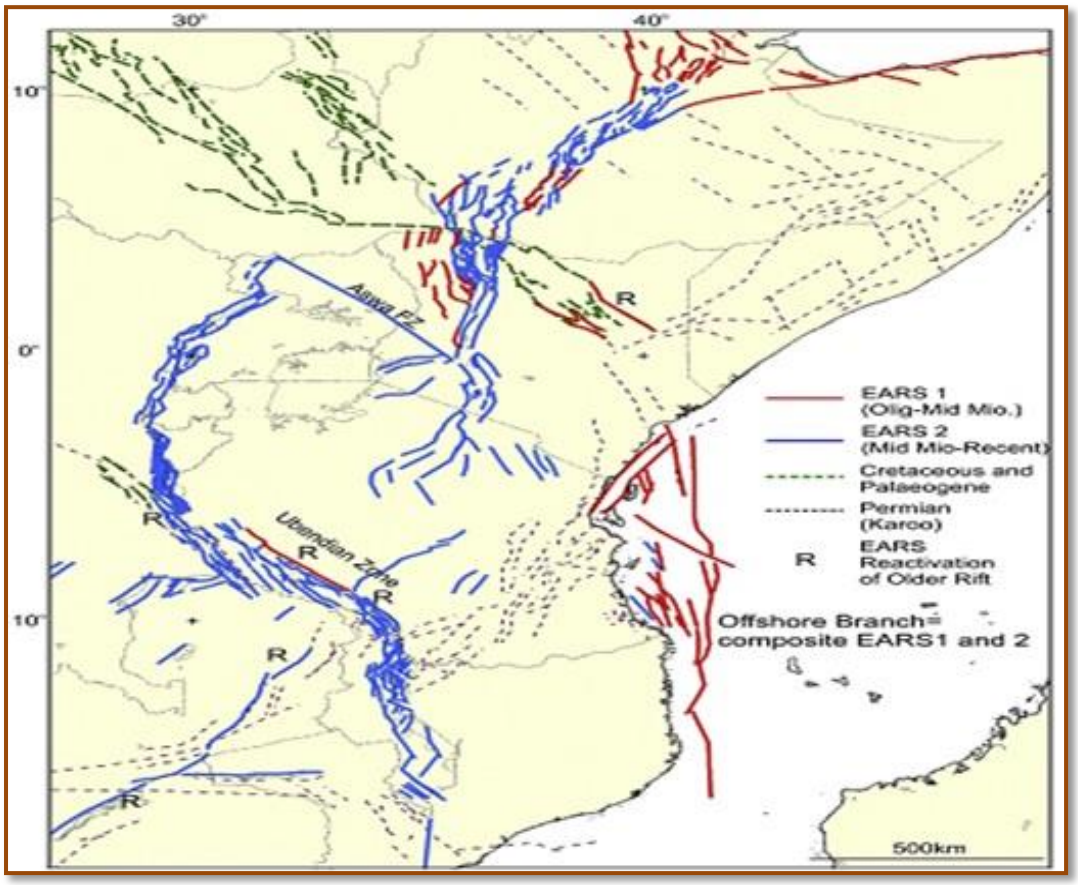

Figure 2.1: *Assignment of rift types in the East Africa based on age. Permo-Triassic ('Karoo'), Cretaceous-Palaeogene, Eo-Oligocene to Mid Miocene (EARS 1) and Mid-Late Miocene to Recent (EARS 2) phases (Macgregor, 2015 pp.234).*

Ring (2014) advocates that the difference between the two branches of EARS is not only by scattering of volcanism on western side than the eastern one. Western branch is not surrounded by a broad regional plateau, low in volume but shows great absolute rift subsidence. In addition to this almost all hominid fossils are from the eastern branch (Bonnefille, 2010). Northern part of the Malawi Rift has been the only locality so far where hominid remains have been discovered in the western branch (Schrenk et al., 1993).

2.2. Main Ethiopian Rift (MER)

2.2.1. Introduction

The Main Ethiopian Rift (MER) is a key area of the EARS that connects the Red Sea-Gulf of Aden junction (Afar depression) with Kenya Rift (Turkana depression) (e.g., Mohr, 1983b; Chorowicz, 2005). The Ethiopian Rift extends for about 1000 km in a NE–SW to N–S direction from the Afar depression southwards to the Turkana depression (Fig.2.2 (A)). The southern boundary traced at latitude ~5° N that characterizes the overlapping area between the Ethiopian and Kenyan Rift (Ebinger et al., 2000). To the north, Wolfenden et al. (2004) suggest, Red Sea–Gulf of Aden–Ethiopian rift triple junction lies in a complex zone at ~11.5° N. Where a left-lateral oblique-slip, Quaternary fault zone (the Tendaho-Goba'ad Discontinuity) separates the roughly E–W extension in the south (Ethiopian Rift) from the NE–SW extension in the north.

According to different authors (e.g., Ebinger et al., 2000), MER extensional deformation start to develop in late Oligocene-early Miocene times. The MER is ~80 km-wide (Mohr, 1983b) rift zone that separates the uplifted western and eastern plateaus (Fig.2.2 (A) and (B)). According to Bonini et al. (2005), the MER is characterised by 6-7 mm/yr relative movement between the two plateaus. The plateaus are formed by volcanism started during the Eocene–Late Oligocene with the eruption of the Ethiopia–Yemen flood-basalt province (Trap series) (Corti, 2009). They are composed of dominantly basalt and intercalated silicic volcanics and built a sub aerial volcanic pile typically 500–1500 m thick and locally attaining 3000 m (Mohr and Zanettin, 1988). The total area covered by these volcanic rocks has been estimated as presently 600,000 km^2 (Mohr, 1983a). According to Kieffer et al. (2004), immediately after the flood basalt volcanic eruption

emplacement a number of large shield volcanoes developed from 30 Ma to about 10 Ma on the surface of the volcanic plateau.

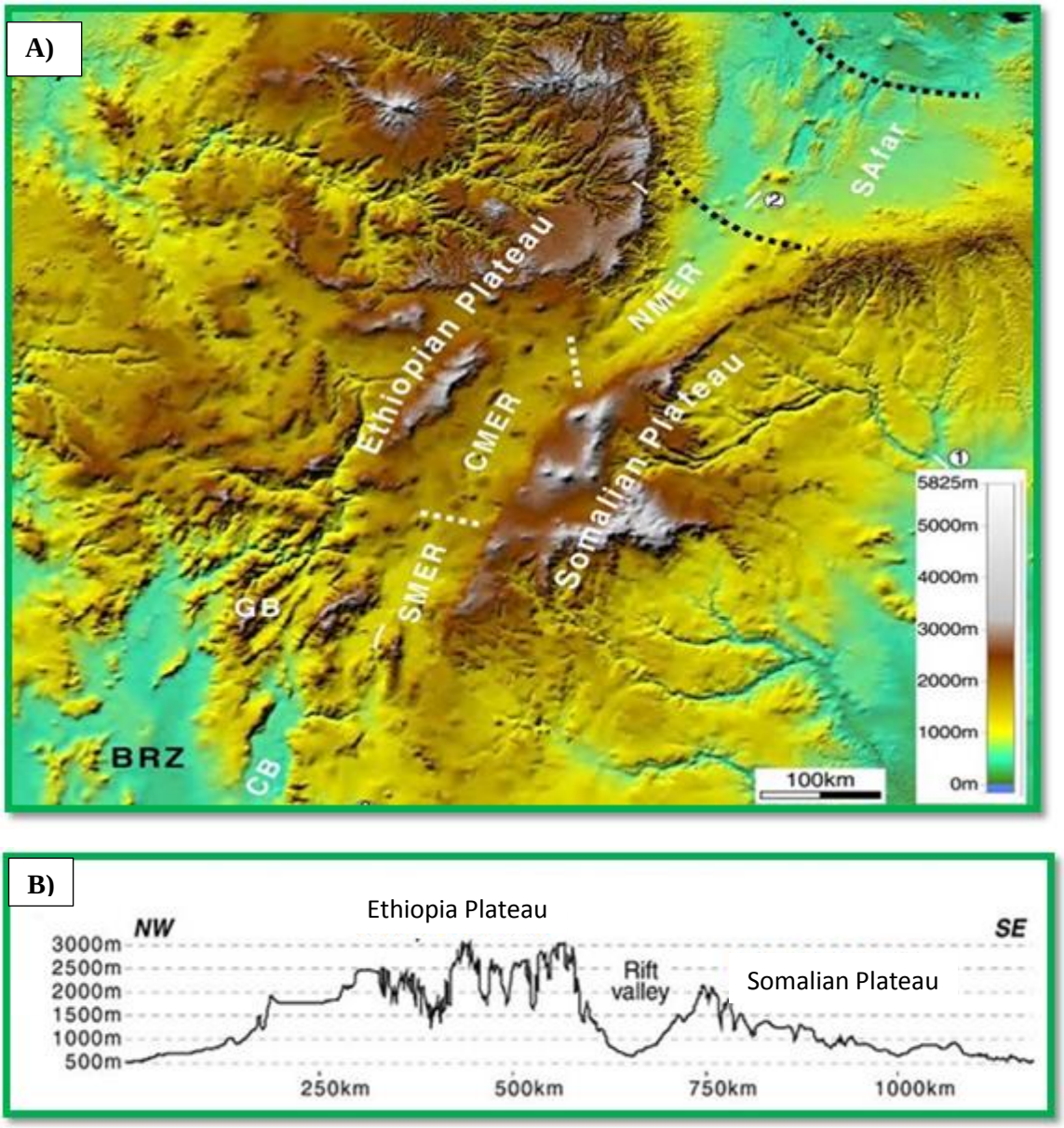

Figure 2.2: ***(A)*** *Digital elevation model of the Ethiopian Rift showing the main rift segments: Southern Afar (Safar), Northern Main Ethiopian Rift (NMER), Central Main Ethiopian Rift (CMER) and Southern Main Ethiopian Rift (SMER). BRZ: Broadly Rifted Zone; CB: Chow Bahir Rift; GB: Gofa Basin and Range.* ***(B)*** *Topographic profile across the rift valley (after Corti, 2009 pp.4).*

The MER is composed of three main different segments; Northern, Central and Southern (e.g., Corti, 2009; Mohr, 1983b; Gidey Woldegabriel et al., 1990; Hayward and Ebinger, 1996). The Northern MER extends from the MER–Afar depression boundary southwards

to the Lake Koka area, where it is separated from the Central MER by the Boru Toru Structural High (Bonini et al., 2005). The Central MER is bounded in the north by Boru Toru structural High. To the south, the boundary between Central and Southern MER can be placed at ~7° N latitude, in the Lake Awassa area, where the rift margins rotate from ~NE–SW to ~N–S, in correspondence to the Goba–Bonga transverse lineament (Bonini et al., 2005). At the boundary of the Central MER and Southern MER, the orientation of the rift valley change from N 20^0-35° to N 5^0-20°, located latitude 7°20′, separated by major E-W trending transverse lineament (Goba-Bonga lineament). South of latitude $6^0$20' N, the Southern MER corresponds to a division of the rift valley by Amaro Horst (block of Precambrian basement) in to near parallel grabens, Chamo (or Ganjuli) basin to the west and Galana Basin to the east (Ebinger et al., 1993; Bonini et al., 2005).

These three segments reflect different stages of the continental extension process that is interpreted from different fault architecture, timing of volcanism-deformation and crustal-lithospheric structure (e.g., Hayward and Ebinger, 1996 see on Fig.2.2 (A)). But commonly they are characterised by typical bimodal magmatic activity and two distinct extensional structures: ~NE-SW to N-S trending border faults and ~NNE-SSW to N-S trending, en-echelon arranged faults obliquely affecting the rift floor (Wonji Fault Belt, WFB; Bonini et al., 2005). The Border faults are major fault-escarpments separating the rift depression from the western and eastern plateaus (Fig.2.2 (A)). These faults are normally long, widely spaced and characterised by large vertical offsets (Boccaletti et al., 1998). But the WFB are arrangement of overlapping, right stepping en-echelon fault segments oblique to the main direction of the rift margins. The faults of the WFB are normally short, closely spaced and display relatively small vertical throws (<100 m; e.g., Boccaletti et al., 1998). Most of the recent (Quaternary) volcanic activity in the MER is closely associated with these fault systems. The WFB developed after 2 Ma (Ebinger and Casey, 2001). According to Keir et al. (2006), in the Southern MER the Wonji faults are relatively less developed than the other sectors of the rift.

Tsegaye Abebe et al. (1998) suggest the MER is characterised by existence of major transverse structures that extend hundreds of kilometers from rift margins. These transverses roughly oriented E-W to ENE-WSW and NW-SE. The E-W structures are represented by Yerer-Tullu Wellel Volcano-tectonic Lineament (YTVL). The YTVL

extends from Tullu Wellel, near Ethiopia-Sudan border, to Ambo fault in northern limit (Tsegaye Abebe et al., 1998). The interpretation of the YTVL is controversial. However, Geophysical data, structural and Oligo-Miocene plateau volcanics indicates the transverse structure represent a pre-existing weakness zones (parallel to the trend of the Gulf of Aden e.g. Bastow et al., 2005). E-W trending transverse lineament is another one relative to the YTVL. That represents by Goba-Bonga lineament; extends across the central part of the MER (Abbate and Sagri, 1980).

2.2.2. Geophysical Background

In the MER the knowledge about crustal and lithospheric structure is significantly increased in a few years back. The major data are collected from Ethiopian Broad band Experiment and the Ethiopia-Afar Geoscientific Lithospheric Experiment (EAGLE). There are also previous geophysical works within the Ethiopian Rift (e.g., Rezene Mahatsente et al., 1999).

The crust beneath the MER generally decreased from the plateaus to the rift axis. On the western and eastern plateaus the crust thickness is in general 38-40 Km (Mackenzie et al., 2005; Mulugeta Dugda et al., 2005; 2007; Keranen et al., 2009). Along the rift axis relative to the plateau, the crustal thickness is thin and become thinner from 33-35 Km at the Northern MER-Central MER boundary to 24-26 Km in southern Afar toward north east (Mulugeta Dugda et al., 2005). Few geophysical data are available for the southern sector of the MER. Receiver function analysis from the Ethiopian Broadband Seismic Experiment (Mulugeta Dugda et al., 2005) suggest a crustal thickness decrease in the Southern MER to values of ~30 km, that is consistent with gravity modeling (Rezene Mahatsente et al., 1999). The majority of the crustal thickness variation is lodged in the upper crust, whereas the lower crust is of relatively constant thickness. The overall lithospheric strength generally is decreasing drastically from Kenyan into Ethiopian rift as a result of increasing temperature in the lithosphere (Keranen et al., 2009).

According to Daly et al. (2008) crustal tomography conveys the existence of anomalously elongate body along the rift axis with a dimension of 20 Km wide and 50 Km long. The anomalous bodies are separated and laterally offset in a right-stepping en-echelon manner. The anomalously fast bodies are also characterised by a high Vp/Vs ratio (Daly

et al., 2008) and relative positive Bouguer anomalies (Rezene Mahatsente et al., 1999). This is interpreted as the presence of cooled mafic intrusion or/and presence of melt in the crust and upper mantle (Daly et al., 2008). The presence of melt is evidenced by Keranen et al. (2009) in which shear wave velocity image is described to indicate high temperatures and the presence of melts.

In the Northern sector of the MER at the depth of immediately beneath the Moho, the lithosphere has a low velocity and low density (Mackenzie et al., 2005). This is interpreted as the presence of hot rocks containing a small percentage of melt. Due to the magmatic modification the mantle lithosphere is greatly thinned beneath the MER and the Afar depression (Mulugeta Dugda et al., 2007). From network of seismic stations data of EAGLE project and Ethiopia Broadband Seismic Experiment (Keir et al., 2006) seismic activity in the Northern and Central MER is localized within Wonji segments.

2.2.3. MER Volcanism

Magmatic activity in the MER seems to have been episodic rather than continuous (Gidey Woldegabriel et al., 1990). That is mainly occurred broadly in two geologic periods; Late Tertiary and Quaternary.

Magmatic activity in Ethiopia generally started with the eruption of Oligocene (~30-35 Ma) voluminous flood basalts (e.g., Mohr and Zanettin, 1988; Ebinger et al., 1993; Gezahegn Yirgu et al., 2006), followed by a complex shield volcano activity (e.g., Kieffer et al., 2004). But in the Southern MER the Tertiary volcanic activity started earlier than other MER sectors at ~45 Ma. This initial volcanic activity in the Southern MER ended around 30 Ma (Zanettin et al., 1978). This volcanic episode was characterised by eruption of tholeitic to alkaline flood basalts and interbedded felsic lavas and pyroclasts (e.g., Mohr and Zanettin, 1988; Kieffer et al., 2004). Flood basalt activity is temporally unrelated to the rifting but there was later magmatism which was strictly related to the tectonic evolution of the MER segments. Close to the rift margin the western and eastern plateau is characterised by Miocene-Pliocene volcanic activity. On western margin, volcanic activity mostly restricted to YTVL (Tsegaye Abebe et al., 1998) that forms aligned central silicic volcanoes. These volcanoes become younger towards the rift from

the 7 Ma Nekemt edifice to the Pliocene-Quaternary volcanoes (such as Wenchi, Wechacha, Furi and Yerer e.g., Tsegaye Abebe et al., 1998).

After this prevalent Mio-Pliocene volcanism, the Quaternary magmatic activity becomes restricted in the rift floor which is associated with WFB. The Quaternary stages of the Ethiopian rift opening have been marked by eruptions of huge amounts of volcanic products. The eruption is with a large prevalence of silicic rocks, minor basalts and scarce or absence of intermediate compositions (e.g., Mohr, 1971; Mohr and Zanettin, 1988; Peccerillo et al., 2003; 2007). Such a bimodal distribution of volcanism is a common feature of many volcanoes, especially in the continental rift, but its genesis is still debated (e.g., Peccerillo et al., 2003).

Chapter Three

3. Local Geology

3.1. Introduction

The rock units are described according to stratigraphic succession (presented on composite stratigraphy; Fig.3.2) from their vertical contact relationship in the field and information from previous absolute dating data. The composite stratigraphy is developed from different exposures which have more than one rock unit in their outcrop. From the oldest to the youngest, the major lithological units identified in the area are; rhyolitic lava flow, pumice flow, ignimbrite, lower pumice fall, rhyolitic lava dome, obsidian, lower basalt, upper ash flow, scoria and upper basalt. Some thin lithological units are not included in the composite stratigraphy namely; lower ash flow, lower ash fall, upper pumice fall and upper ash fall. But these thin lithological units are presented on the lithological description section separately.

The stratigraphic relationship between the section that contain the lower basalt and section contain obsidian is not identified in the field. In this case previous dating made (and or presented) by Alula Damte et al. (1992) and Boccaletti et al. (1999) is used by comparing the petrological and geochemical characteristics of those rocks described by the authors. The dating show a significant time gap between the obsidian (the last product of the volcanic eruption sourced from Boko volcanic centre) and the overlying lower basalt. With the same scenario, there exists a presence of erosional surface and paleosoil in the contact between upper basaltic product, upper ash flow and lower basalt that indicate significant depositional time gap. This pyroclastic flow deposit (upper ash flow) is presented on the Alula Damte et al. (1992) as part of Dera-Sodore unit. By considering this the contact line for those units on the composite stratigraphy is a zigzag line to represent and show a significant time gap. The areal distribution of the rocks and structures are presented on geological map and geological crossection (Fig.3.1).

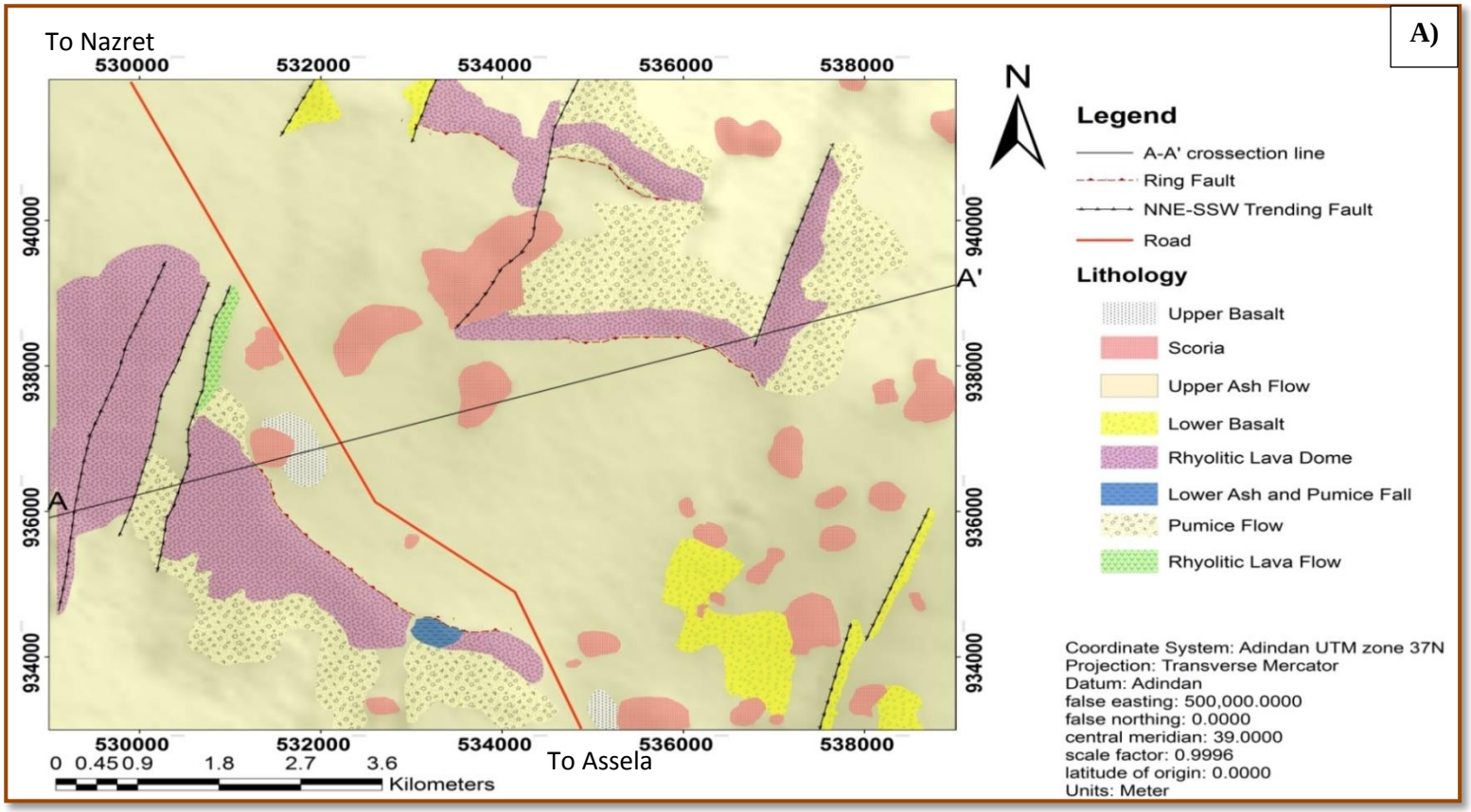

Figure 3.1: *Geological map of the study area (**A**) and geological crossection along A-A' traverse line (**B**).*

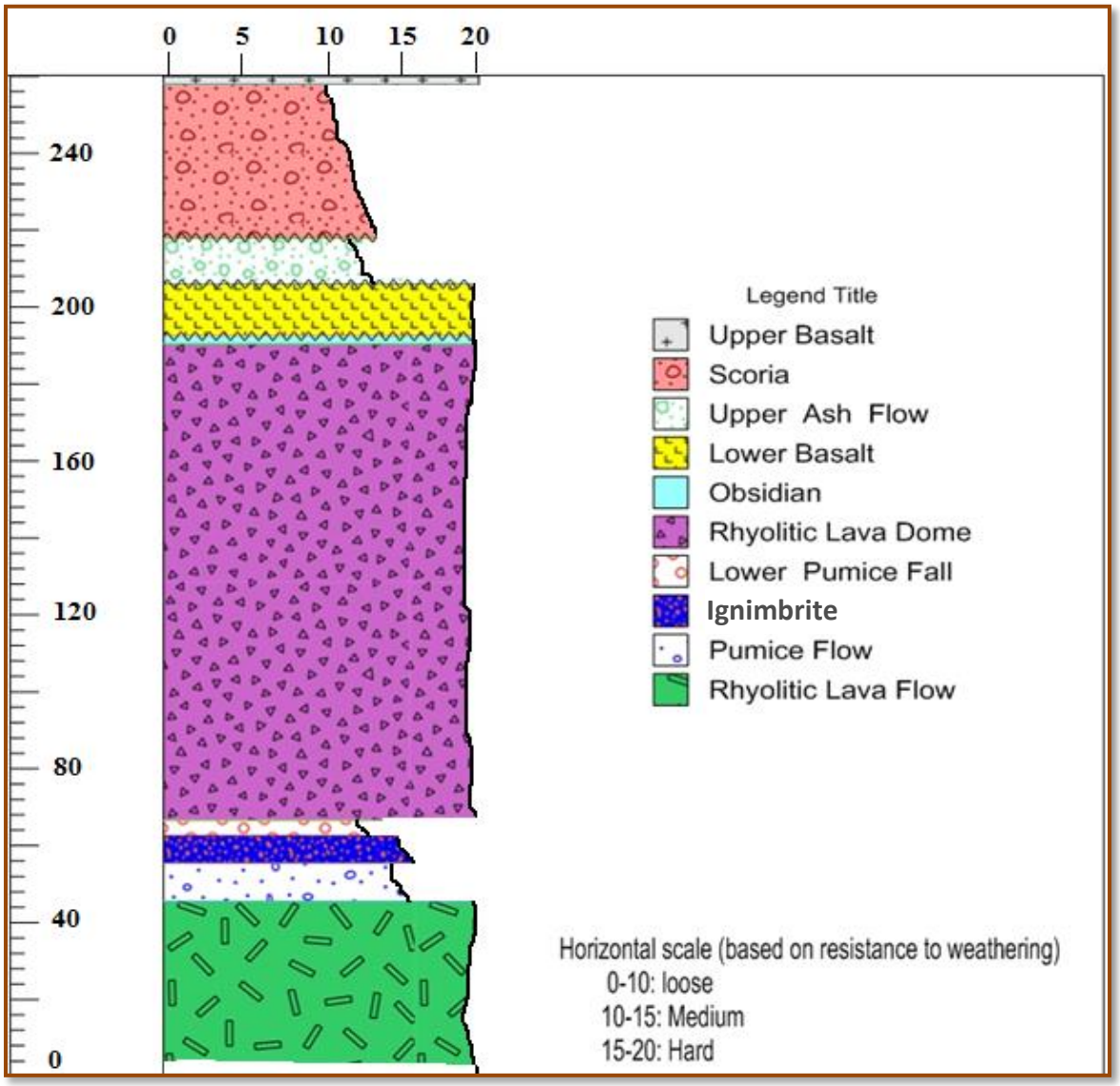

Figure 3.2: *Composite stratigraphy of BMC. The scale labeled vertically shows the thickness (m).*

3.2. Lithology and Petrography Description

3.2.1. Rhyolitic Lava Flow

From the ten major lithological units rhyolite is the main unit that has a major thickness relative to the rest in the rock succession. The rhyolitic rock observed in the study area is two type; lava flow and dome forming. These two types of rhyolites are further reclassified into two by their color; grey rhyolite and pink rhyolite. The dome forming

rhyolite exposed on the top of the Boko and Dabe section, while rhyolite lava flow exposed on the back and front-bottom part of the Boko section and out side of the caldera.

The rhyolitic lava flow on the back of the Boko section is exposed by forming a clear contact with pumice flow on its top (Fig.3.3). The phenocrysts are mainly feldspars. At north western part of the study area rhyolite exposed along fault scarp that run NNE-SSW direction. At this location the rhyolite show a clear lamination parallel to the layering. This lamination formed by alternation of white and dark-redish color. The layering in this location has orientation of $080^0/20^0$ NE. Generally, this unit has a maximum vertical thickness of 45 m, grey color, porphyritic texture and layering with dip amount below 40^0. The layering (or flow banding) measurments are presented in appendix II.

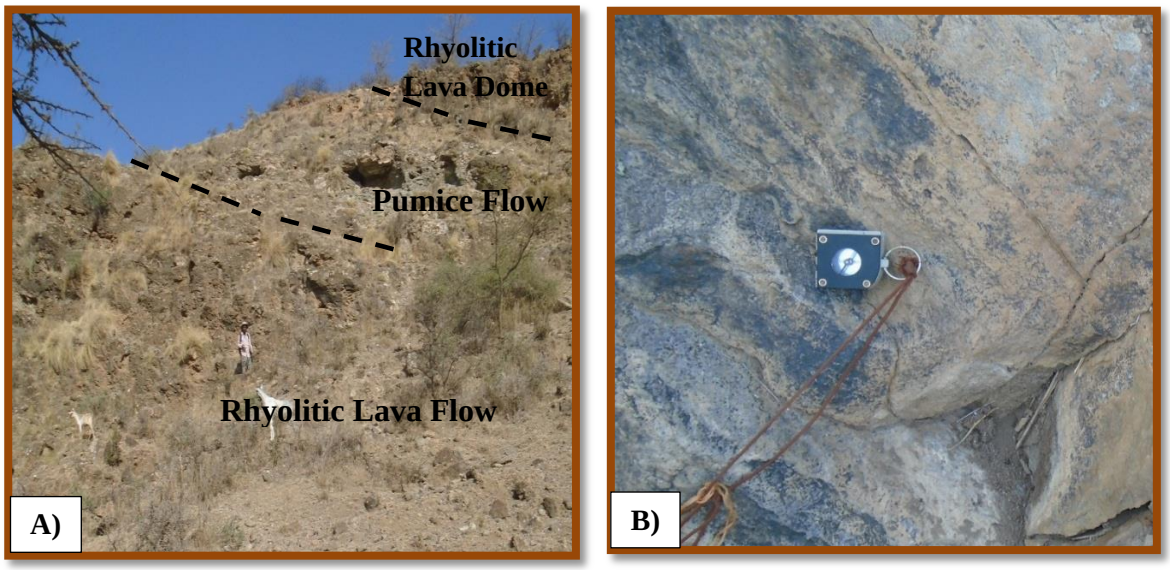

Figure 3.3: *(**A**) Exposure that contain rhyolitic lava flow, pumice flow and rhyolitic lava dome rock types on the back-bottom of Boko section.(**B**) Rhyolite lava flow exposed on a fault scarp that is located north western part of the study area.*

Two samples (RP-9 and RP-2) are prepared for petrographic examination. The rock show glomeroporphyritic texture (Fig.3.4); is a variety of porphyritic texture which has clusters of phenocryts (~20%) specially quartz and alkali feldspar in the groundmass. The phenocrysts are mainly; 3% Fe-Ti oxides, 5-9% quartz and 8-9% alkali feldspar. There are 2% of olivine and clinopyroxene phenocrysts in sample RP-9 which show alteration (~50% of the crystals) in to opaque mineral on the rim of the mineral grains.

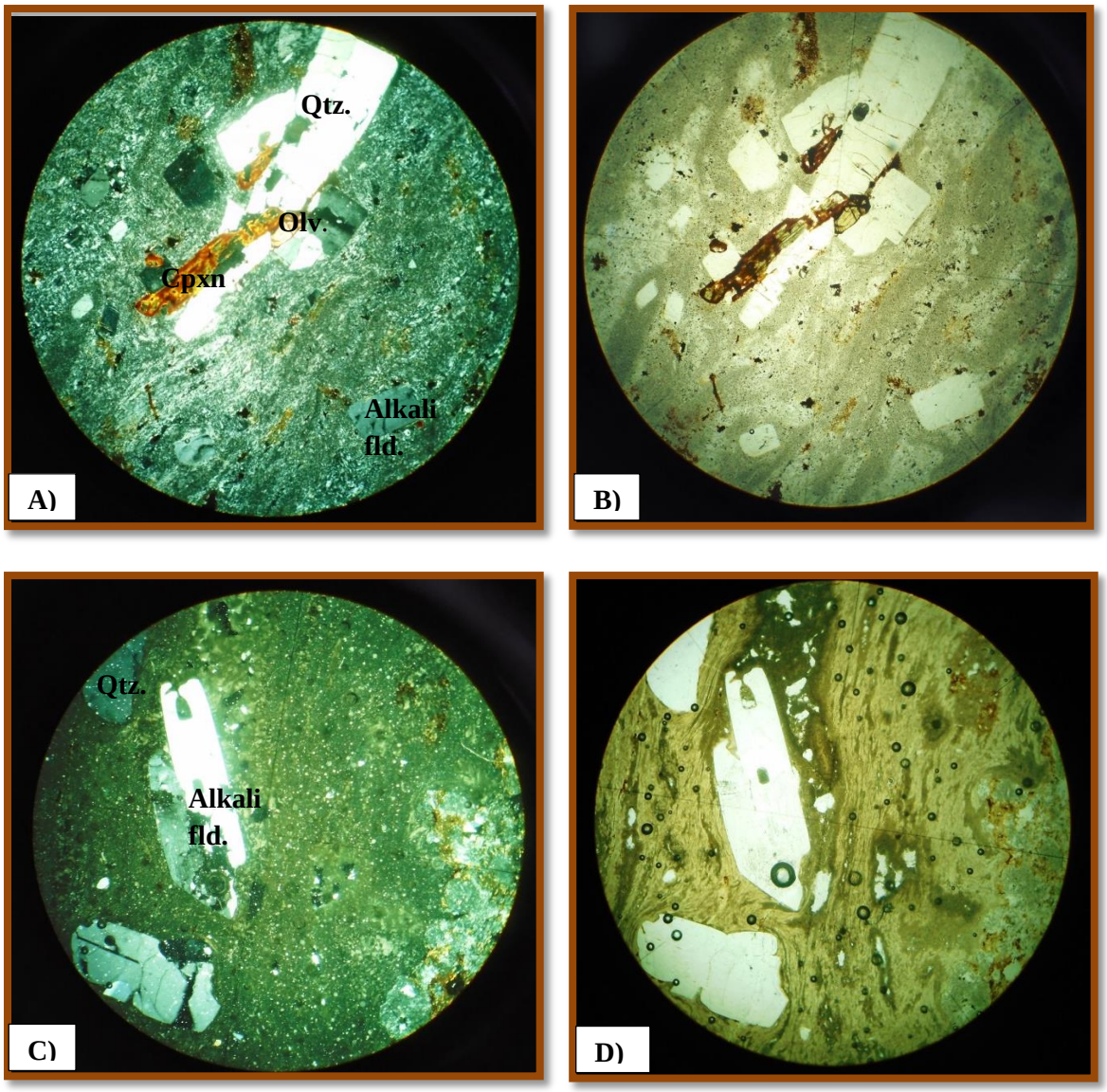

Figure 3.4: *Microphoto picture of samples RP-9 (**A** & **B**) and RP-2 (**C** & **D**) under optical microscope in different view;XPL (**A** & **C**) and PPL (**B** & **D**) at 10X magnification. The labels stands for; Qtz-Quartz, Alkali-fld.-Alkali feldspar, Cpxn-Clinopyroxene, Olv-Olivine and Opq-Fe-Ti oxides.*

Maximum grain size of the phenocryst along there longest dimension are; 0.16 mm Fe-Ti oxides, 0.24 mm olivine, 0.76 mm clinopyroxene, 0.8 mm alkali feldspar and 0.84 mm quartz. The average grain shape of all the phenocrysts is subhedral. In sample RP-2 quartz and alkali feldspar has porespaces in their crystals; called sieve texture. In over all, the rock show layering and the phenocrysts are oriented to the layering. The groundmass is mainly composed of microcrystals of quartz and alkali feldspar. Spherulitic textures are observed on the groundmass due to overgrowth of microsized quartz and alkali feldspars.

3.2.2. Pumice Fall and Pumice Flow

Pyroclastic pumice is another lithologic unit that exposed on the area of study. Depending on the characteristics seen in the field, it is classified in to two; pumice flow and pumice fall.

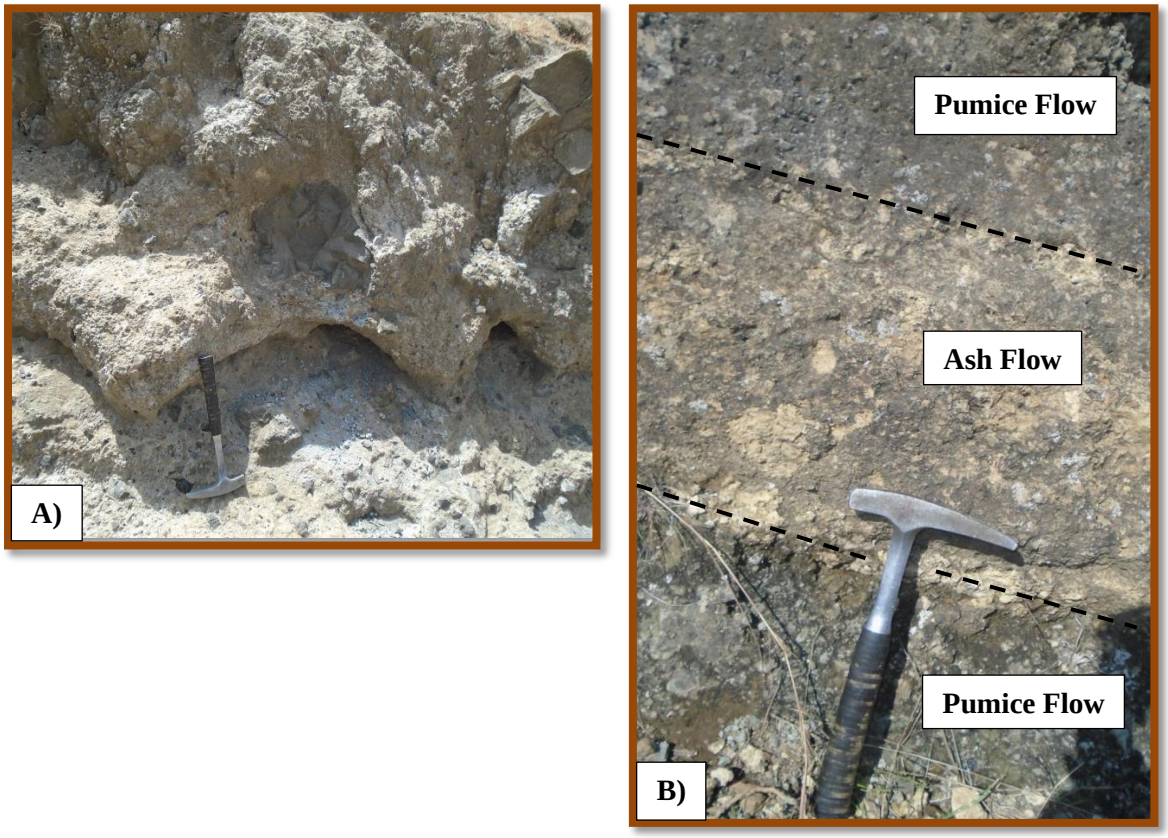

Figure 3.5: *Pumice flow exposure outcroped on the bottom of the Dabe section (**A**) and southern tip of Boko ridge (**B**). Note that on figure "**A**" the lithic fragments are rhyolite and obsidian. On "**B**" the outcrop show intercalation of ash flow with pumice flow layer.*

Pumice flow is a lithological unit that mainly composed of a pumice fragments and formed by a pyroclastic flow process. This type of deposit covers a large area relative to the pumice fall deposit that mainly found on the back of the Boko ridge and on the Dabe section. The deposit is overlain by different rock units namely; pumice fall, rhyolitic lava dome and also by ignimbrite. With these rock units the pumice flow forms abrupt contact. In the southern tip of the Boko ridge the rock unit is intercalated with pyroclastic ash flow (see Fig.3.5 (B)). On the different exposures the deposit show poor sorting, variation in vertical thickness, maximum vertical thickness of 13 m and contain large boulders of

lithic fragment. The lithic fragments are mainly obsidian and rhyolite (see Fig.3.5 (A)). The lithic fragment size varies between 3 cm to 7 cm on the various exposures. The pumice fragments show similar characteristics with the pyroclastic fall deposit but in this case the pumice clasts relatively show roundness to some extent.

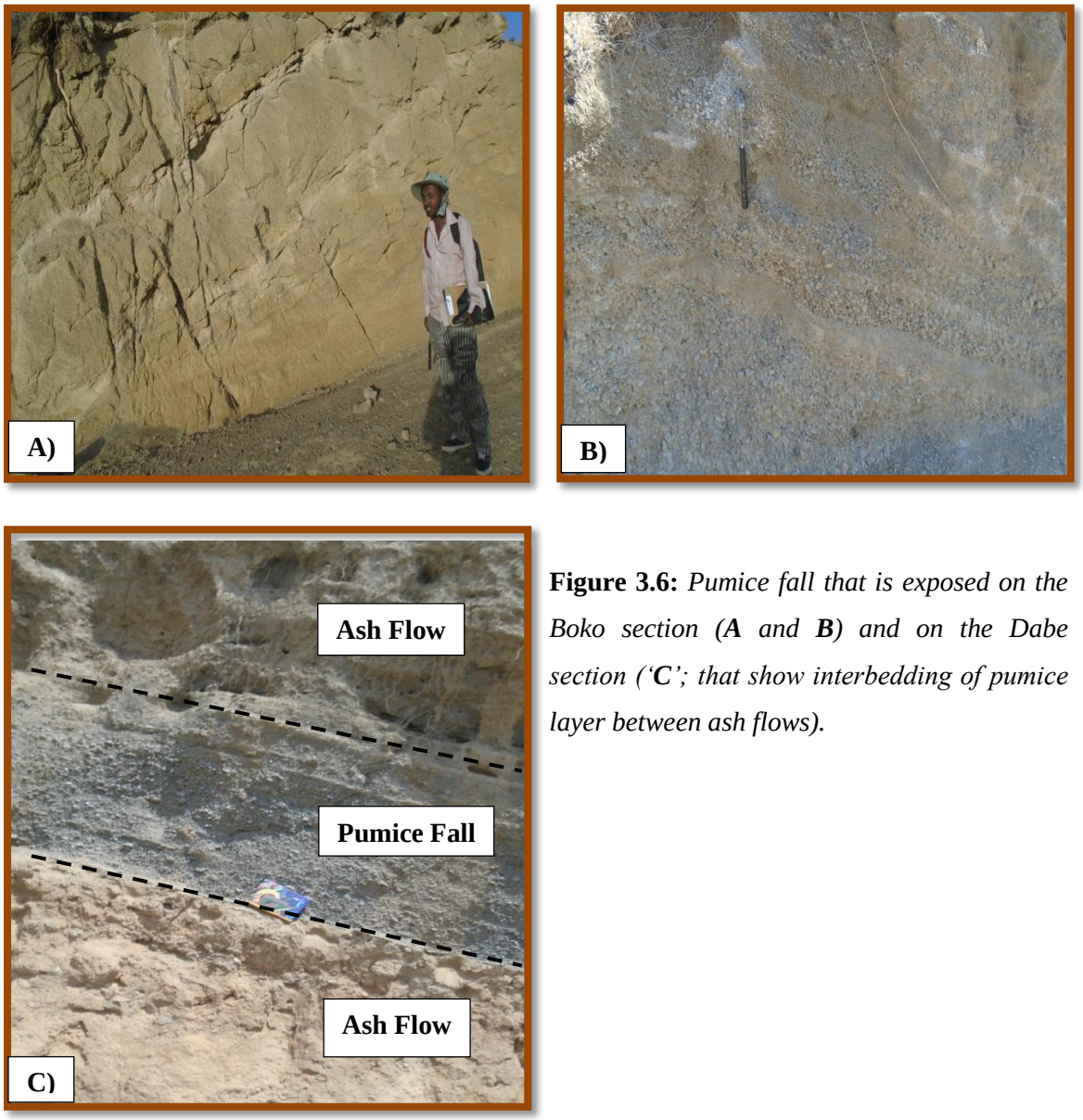

Figure 3.6: *Pumice fall that is exposed on the Boko section (**A** and **B**) and on the Dabe section ('**C**'; that show interbedding of pumice layer between ash flows).*

Pumice fall is the second type of lithological unit that mainly composed of pumice fragment. This unit exposed in different part of the area and specified in one position of the composite stratigraphy. In the composite stratigraphy the pumice fall ovelay the rhyolitic lava flow (lower pumice fall; see Fig.3.6). Lower pumice fall has a maximum thickness of 4 m. Pumice fall (upper pumice fall) is observed on the top of rhyolitic lava dome that is overlain by ash fall and ash flow in field (Fig.3.6 (C)). Upper pumice fall has

a maximum thickness of 1 m. Because of the thickness this unit is not presented on the composite stratigraphy. The two deposits show a similar characteristics except the pumice fragment is smaller on the upper fall deposit relative to the lower one. The thickness in the two stratigraphic unit show a slight variation.

The pumice fall deposits are well sorted, maintain similar local thickness, have light specific gravity and show high porosity with interconnected pores. The fragment size of the pumice in each exposures vary in the range of 2 mm to 7 cm. The exposure types that the deposit exposed are mainly on road cut and rarely on cliff type. The color of the deposit is commonly found as grey but the pyroclastic pumice fall deposit found on the southern tip of the Boko ridge have pale yellow color which might be a result of secondary alteration. Some of the exposures found on the northern tip of the Boko section have crystals, mainly alkali feldspar.

3.2.3. Ignimbrite

Ignimbrite unit is one of the lithological units found in the study area which is not mapable; that means the rock unit area coverage is below the scale of the geological map (1:25,000) and the contour interval (10 m). This unit is exposed on two big sections; Boko ridge and Dabe section.

The ignimbrite unit that is exposed in Boko ridge is along a seasonal stream cut. The exposure is continues along the stream in south east direction. But vertically after 2 m thickness the unit is contacted with pumice flow that is separated by a major NNE-SSW trending fault. Along east-west direction, across the stream, the exposure is 10 m wide. The rock is grey in color and contains fiami and rock fragment. The rock fragment has grey color and show a layering (Fig.3.7 (A)). These characteristics (the color and layering) suggest the rock fragment is dominantly rhyolite. The fiami has black color. The rest of the rock part composed of fine grained and visible crystals. The fine material show grey to white in color and make up the ground mass. Visible crystals are white in color. The rock is highly weathered with a weathering color of light brown.

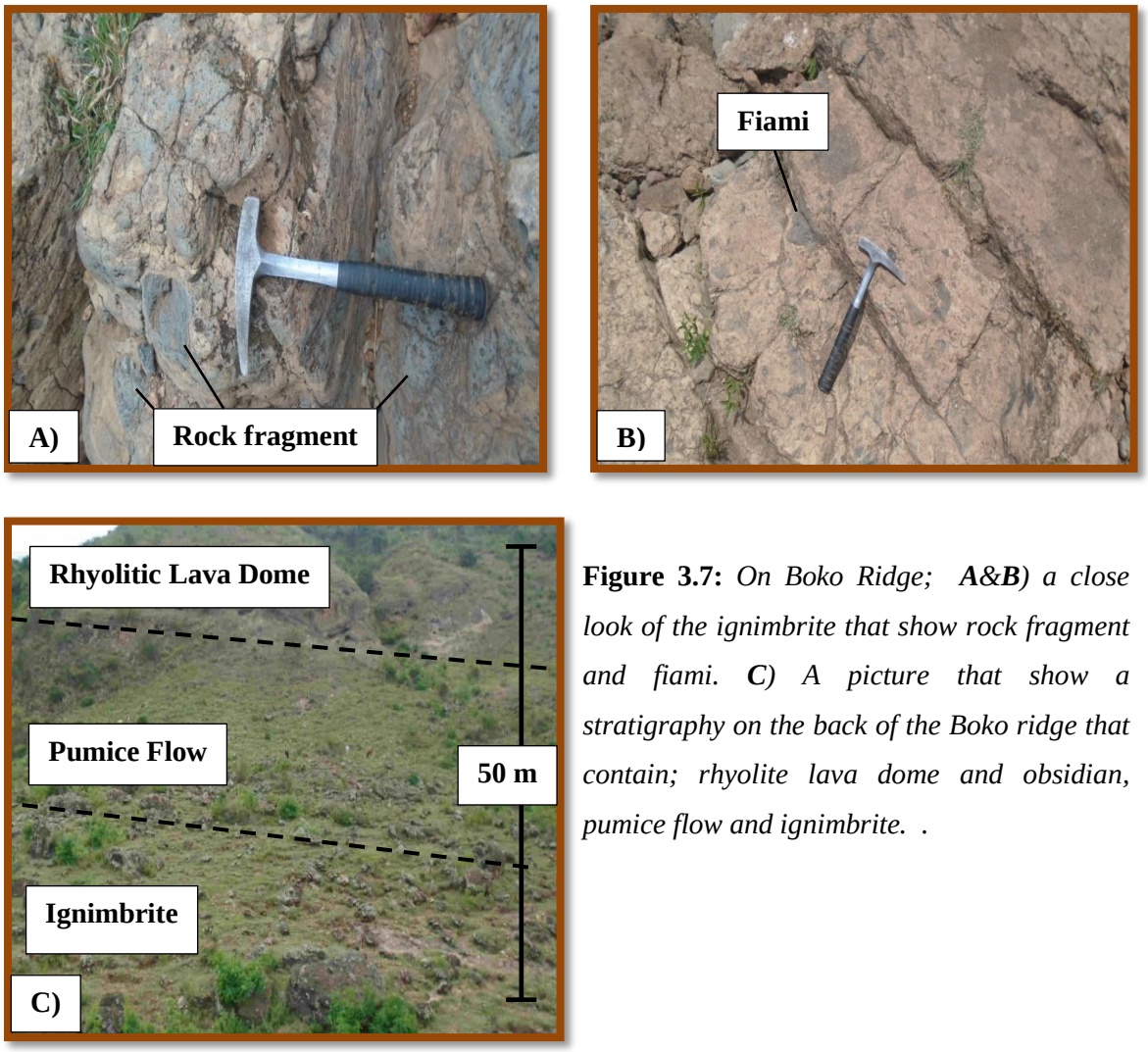

Figure 3.7: *On Boko Ridge;* ***A&B)*** *a close look of the ignimbrite that show rock fragment and fiami.* ***C)*** *A picture that show a stratigraphy on the back of the Boko ridge that contain; rhyolite lava dome and obsidian, pumice flow and ignimbrite.* .

Ignimbrite rock unit with a bit different characteristics is exposed in the bottom part of the Dabe section; between the Dabe section and Dera scoria cone (that located on north east side of the study area). The type of exposure is a cliff that is mainly composed by this rock unit underlain by pumice flow deposit (Fig.3.8). This rock exposure is fresh and rich in lithic fragment relative to the ignimbrite exposed on the back of the Boko ridge. It shows grey color with a little disimilarity to the previous exposure. It is fiami poor. The rock fragment is grey and pinkish in color. The rest rock part (juvenile material) made of fine groundmass (grey in color) and visible crystals (white in color). The maximum vertical thickness of this unit is 7 m.

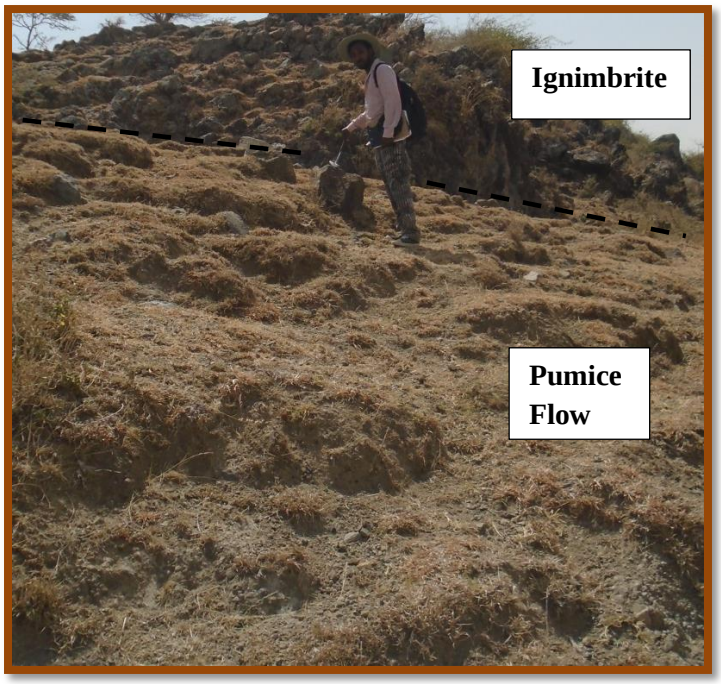

Figure 3.8: *A picture showing rock succession exposed on the bottom section of Dabe. The ignimbrite is underlain by pumice flow.*

One sample that is collected from the Dabe section is prepared for petrographic analysis. The rock show glomeroporphyritic texture (see on Fig.3.9). The phenocryst assemblage is dominantly composed of quartz and alkali feldspar. The modal proportion of the phenocryts is ~28% and constituet; 1% pyroxenes, 2% Fe-Ti oxides, 8% alkali feldspar and 17% quartz. The crystal shape of quartz grains show dominantly anhedral and alkali feldspar show subhedral. The maximum length for the largest grains measurment result for each phenocryst are; 0.68 mm alkali feldspar and 1.84 mm quartz. Quartz grains relative to the other phenocrysts show a sieve texture (open spaces in the crystal grains) and circular cracks called perlitic cracks. The groundmass is microcrystalline which mainly composed of quartz and alkali feldspar. Rock fragments are present in the thin section which are composed of rhyolitic and basaltic rock. The rhyolite rock fragment show microcrystals of quartz and alkali feldpar. The basaltic rock fragment show altered plagioclase feldspar and opaque minerals. The maximum size of the longest dimension of rock fragment is 1.2 mm rhyolite and 1.9 mm basalt. From the modal proportion destribution of the phenocrysts we can conclude that the rock is Rhyolitic ignimbrite.

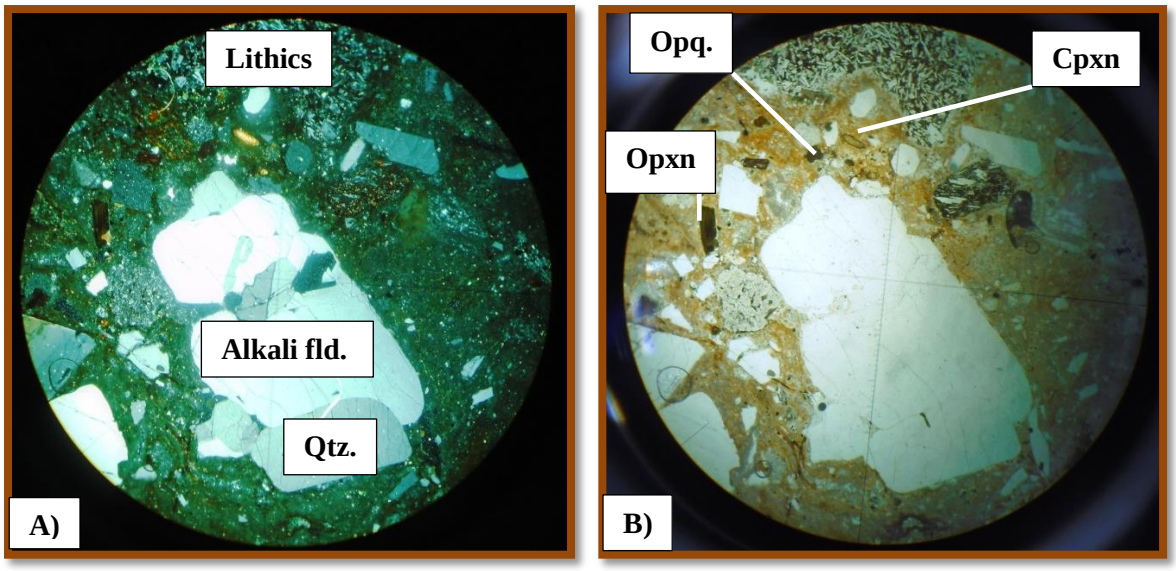

Figure 3.9: *Microphoto picture of ignimbriter(RP-8) in 10X magnification under XPL (**A**) and PPL(**B**) view. The labeles are phenocrysts (Qtz-Quartz, Alkali fld.-Alkali feldspar, Opaq-Fe-Ti oxides, Opxn-Orthopyroxene and Cpxn-Clinopyroxene), Lithics–Lithic fragment and Microcrystalline groundmass.*

3.2.4. Rhyolitic Lava Dome

As mentioned on subheading 3.2.1 from the ten lithological units rhyolite is the main unit that has a major thickness relative to the rest in the rock succession. The rhyolitic lava dome takes the most proportion of vertical thickness with comparing to rhyolitic lava flow. This variety of rhyolite has two types; grey and pink rhyolite. On different exposure the rhyolite shows a bit different characteristics but in general it forms flat plain like physiography on top.

The Boko section contains rhyolite lava dome that intercalates with poorley welded ash flow and fragmented obsidian on the upper part of the section. The largest vertical thickness of rhyolite lava dome is observed in this exposure approximetly 90 m. Above the intercalation of rhyolite and ash flow, aphanitic rhyolite is exposed. The color of the rhyolite is dark-grey and its weathered color is white spots on the dark background. The rock is dome forming that means it has large height relative to its width and show sub vertical layering (flow banding). The layering dip amount is above 50^0 (see appendix II for the detail). On bottom of the Dabe section a rhyolitic rock with similar characteristics exposed. This unit is the main block that cover maximum thickness of the Dabe section.

To the east direction from the exposure at elevation of 1656 m a.s.l., the rhyolite which has the same characterstics intercalate with the obsidian unit which has fragmental nature.

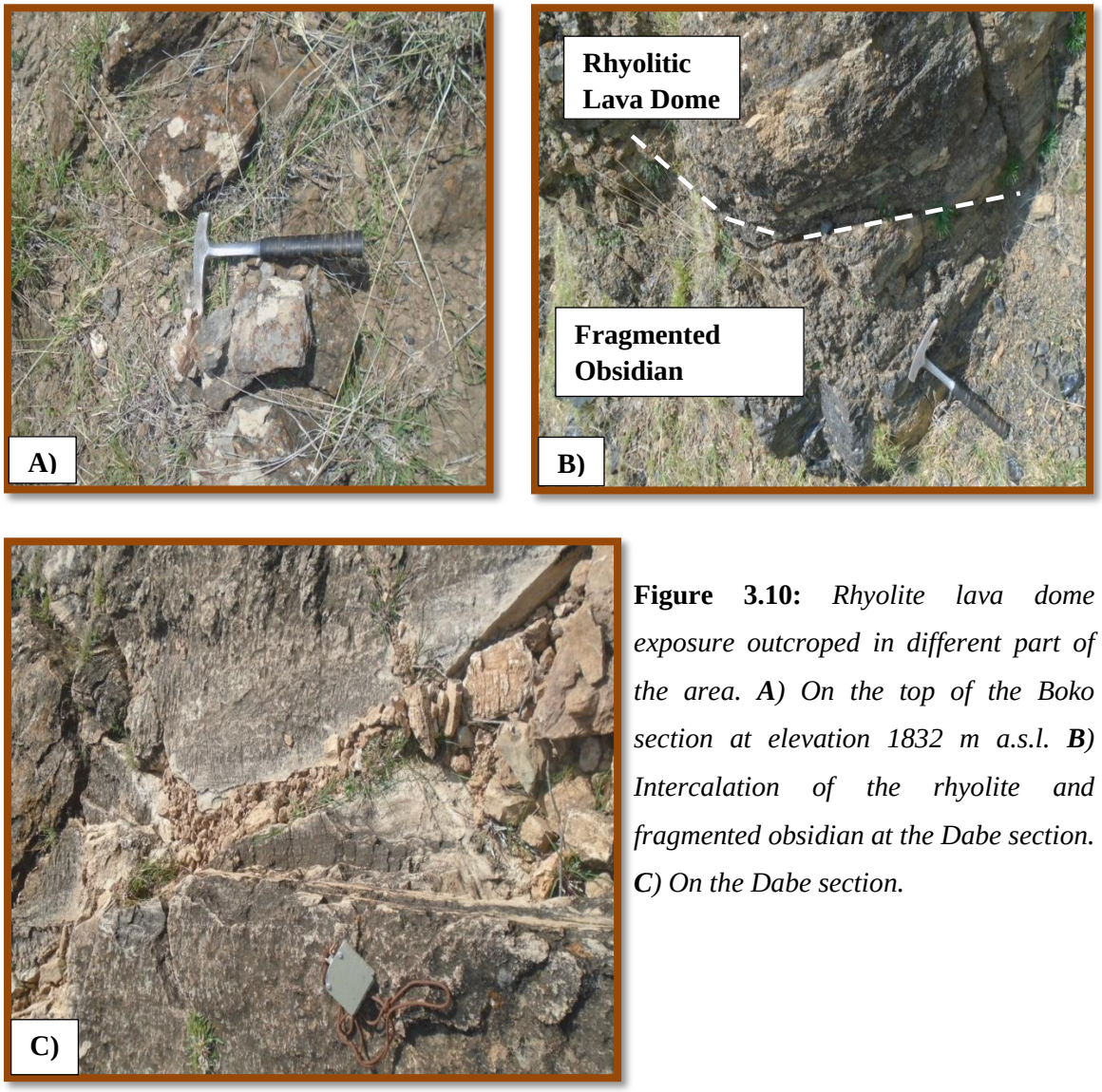

Figure 3.10: *Rhyolite lava dome exposure outcroped in different part of the area.* ***A****) On the top of the Boko section at elevation 1832 m a.s.l.* ***B****) Intercalation of the rhyolite and fragmented obsidian at the Dabe section.* ***C****) On the Dabe section.*

Hand specimen collected at the bottom of the Dabe section is prepared for petrographic analysis. The rock show hyalopilitic texture (see Fig.3.11); is special type of trachytoid texture that has a characteristics of alkali feldspar microlites oriented and follow the outline if they encounter relatively bigger mineral grain. The phenocrysts have a sieve texture (inclusions of elongated alkali feldspar), that make them difficult to differentiate optically. The visible phenocrysts which is inclusion free is composed of 2% Fe-Ti oxides, 3% quartz and 4% alkali feldspar.

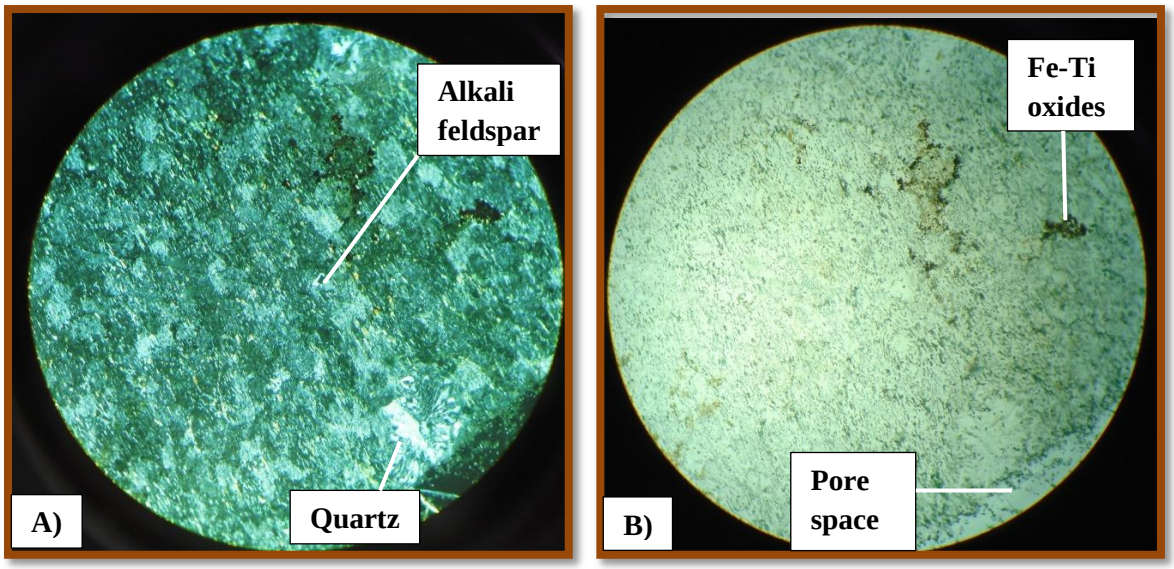

Figure 3.11: *Microphoto picture of dome forming rhyolite (RP-1); XPL (**A**) and PPL (**B**) view at 10X magnification.*

The maximum grain size of each mineral observed in the thin section is measured on its longest dimension as; 0.8 mm Fe-Ti oxides, 0.8 mm quartz and 2.4 mm alkali feldspar. The grain shape of the phenocryst is anhedral (quartz and Fe-Ti oxides) and subhedral (alkali feldspar). The groundmass is the leading one regarding to the modal proportion, that counts 90% composition. In composition the groundmass is microcrystalline quartz and alkali feldspar.

Pink rhyolite is the other variety of rhyolite lava dome that is observed in the study area. This type of lithologic unit exposed on the caldera floor by stream cut and domes outside the caldera. The rock has pink to redish color, aphanitic texture, a weathered color of dark-brownish, layered and has vesicles with longest dimension oriented parallel to the layering. But the rhyolite that is exposed on the stream cut has a color of light pinkish. In this exposure the vertical thickness of the exposed rhyolitic unit is 2 m. The pink rhyolite, that exposed on the dome at location E 0529755, N 0938191 and elevation 1735 m a.s.l, is porphyritic in texture. The phenocryts are white color while the groundmass is pink.

Two samples (RP-3 and RP-5) that are collected from the caldera floor and from the dome outside the caldera are prepared for thin section study. The rock thin sections show porphyritic (see Fig.3.13) texture with small volumetric proportion (18% to 23%) of phenocrysts. The phenocrysts are 4-5% quartz, 4-7% Fe-Ti oxides and 7 & 13% alkali

feldspar. The maximum grain length of each phenocrysts are 0.3 mm Fe-Ti oxides, 0.42 mm alkali feldspar and 0.64 mm quartz. The grain shape of each phenocryst show anhedral (quartz and Fe-Ti oxides) and subhedral (alkali feldspar). The groundmass take the maximum modal proportion (68-77%); it's composed of microcrystalline quartz, alkali feldspar and redish stains (that might be clay minerals from hydrothermal alteration).

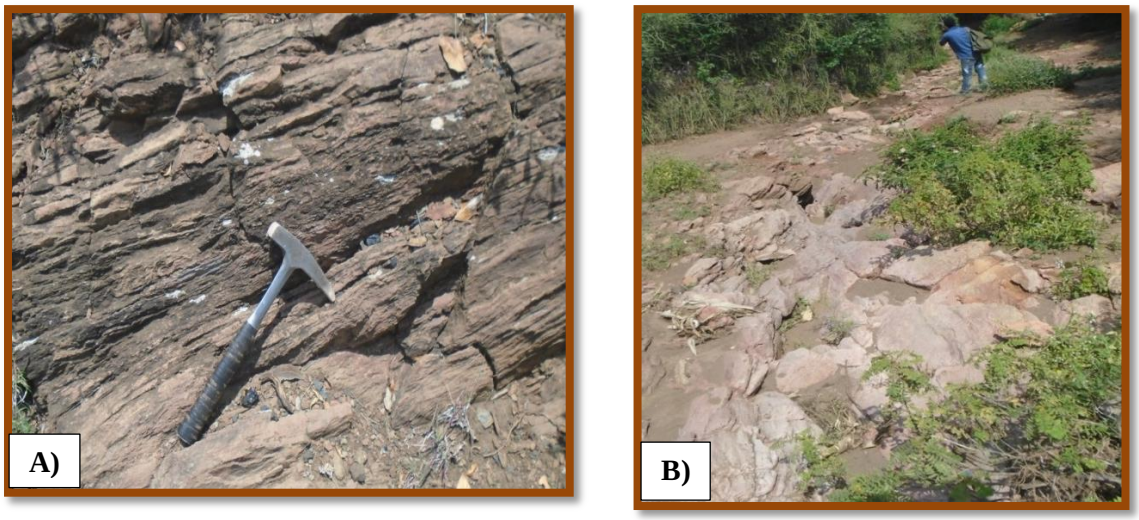

Figure 3.12: *Pink rhyolite outcrops in different location.* ***A****) Exposed at dome outside the caldera.* ***B****) Exposed on the caldera floor along stream cut.*

On sample number RP-5, the rock show radiate texture. This radiate texture is formed by overgrowth of alkali feldspar on existing phenocryst. The phenocryst in the radiate microstucture is dominantly alkali feldspars and quartz. The other type of texture observed in this sample is intersertal texture (Fig.3.13 (A) and (B)); that is formed by Fe-Ti oxides embeded in alkali feldspar and quartz. Some of the alkali feldspar grains show half sector zone (is a variety of zoning that takes idealy the form of four triangular segment with a common apex). The microlites show alignment in a single direction. Sample number RP-3 show hyalopilitic texture (see in Fig.3.13 (C) and (D)); special type of porphyritic texture which is the alkali feldspar and quartz microlite orientation follows the outline of phenocrysts. In thise sample the alkali feldspar show oscillatory zoning (a rythimic repitation of width formed by compositional difference).

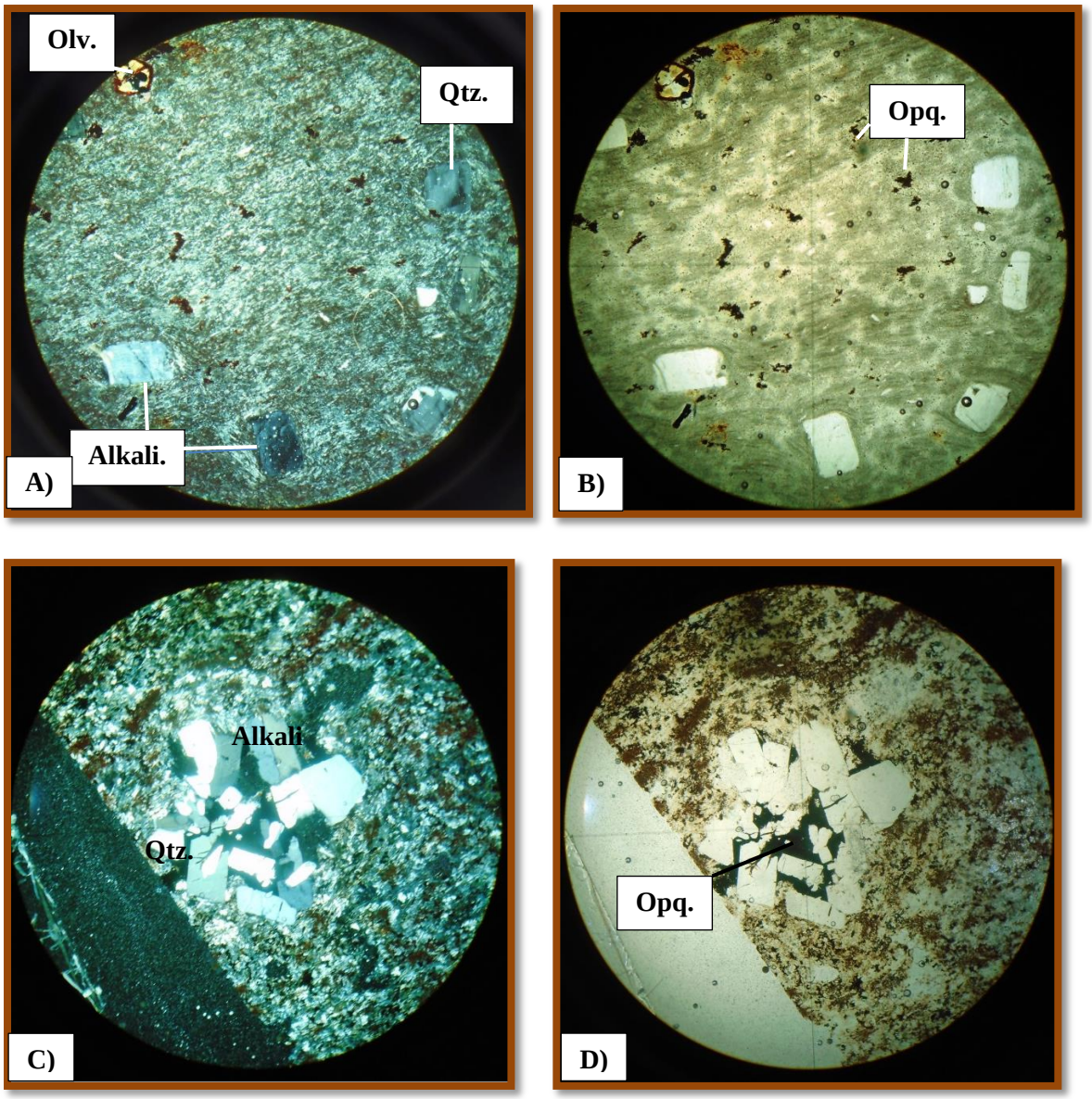

Figure 3.13: *Microphoto picture of pink rhyolite lava dome samples; RP-3 (**A**&**B**) and RP-5 (**C**&**D**) under optical microscope in different view XPL (**A**&**C**) and PPL (**B**&**D**). The labels stands for; Qrtz-Quartz, Alkali-Alkali feldspar and Opq-Fe-Ti oxides. The photo is taken at 10X magnification.*

3.2.5. Obsidian

Obsidian unit is the other unit that is exposed on the study area. This unit show more or less uniform character relative to the other units found in the area. Two categories are identified based on physical difference. The first one is massive obsidian that is exposed on top of the Boko and Dabe section. The second variety is fragmented obsidian; exposed on the middle portion of the Boko section and on the top of domes outside the caldera .

Massive obsidian exposed on top part of the Boko section and Dabe section is well indurated, has no layering structure, show black fresh color, brownish weathered color, has a glassy texture, show concoidal fracture and has shiny appearance. On both sections this type of unit outcroped by intercalating with dark grey aphanitic rhyolite (see Fig.3.14). Sample is collected for geochemical analysis on different locations.

Figure 3.14: *Massive Obsidian exposed on top part of the Boko section.*

The second variety of obsidian unit is fragmented obsidian. This rock unit is very fragile and weak. With the same characteristics to the massive obsidian; it's black in color, glassy in texture and has brown weathered color. This unit is exposed in the middle portion of the Boko (see Fig.3.15) and Dabe section and on the top of the domes located outside the caldera. It's intercalated with rhyolite lava dome and ash fall.

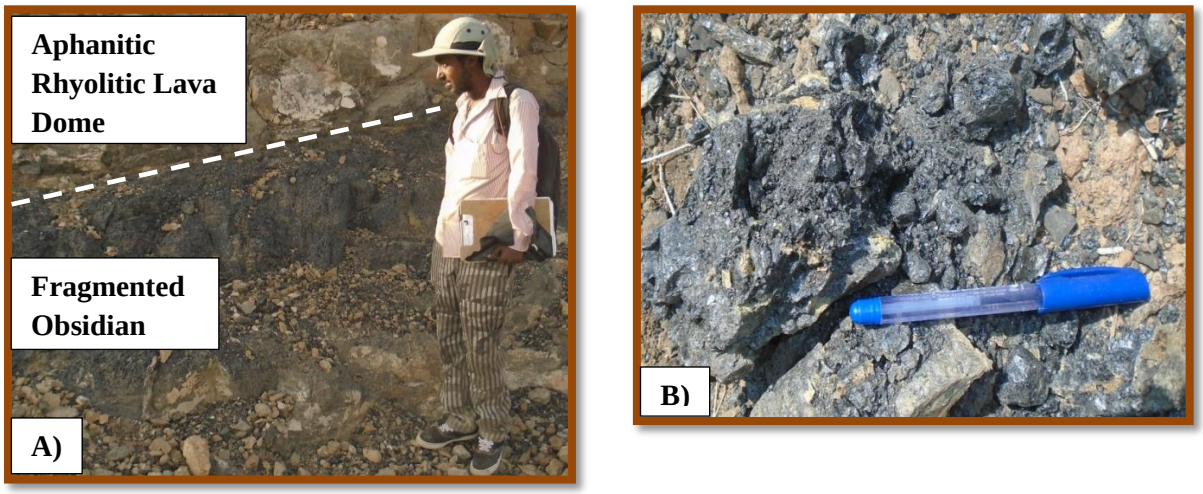

Figure 3.15: *Fagmented obsidian exposed on the middle portion of the Boko section on outcrop scale (**A**) and hand specimen scale (**B**).*

3.2.6. Lower Basalt

Basaltic lava flow is found in the area of study by forming a gentle slope and steep cliffs along fault exposures. Based on stratigraphy and petrological characteristics, the basaltic lava flow is classified into two units; lower basalt and upper basalt. Stratigraphically the lower basalt is found below the upper basalt. In this section of the lithological description the lower basalt is presented.

Lower basalt is constituted by a basaltic lava flow underlain by thin scoria (Fig.3.16 (A)). The scoria is highly fragmented with a range of fragment size from boulder to lapilli and has black color. The lava flow is found in the stratigraphy by underlying ash flow (Fig.3.16 (B)). From different exposure the maximum thickness measured is 13.5 m that exposed along NNE-SSW trending major fault. The rock is aphanitic and in some area shows porphyritic texture, dark grey color and has polygonal joints on its surface (see Fig.3.16 (C)). The porphyritic basalt shows phenocrysts of dominantly olivine and plagioclase feldspar and pyroxene in small proportion. This rock unit is exposed only in the southeastern and northwestern part of the study area.

Two samples (RP-7 and RP-10) are prepared for petrographic analysis. The samples show a seriate texture (see on Fig.3.17) which is the grain size has a large variation. The visible grains are mineralogically composed of 1% orthopyroxene (only seen in sample RP-10), 1% alkali feldspar (only in RP-10), 2% clinopyroxene (only found in RP-7), 5 & 14% olivine, 4 & 15% Fe-Ti oxides and 18 & 24% plagioclase feldspar. The maximum dimension of each largest visible mineral grains are measured and the result shows; 0.08 mm Fe-Ti oxides, 0.36 mm clinopyroxene, 0.44 mm alkali feldspar, 0.64 mm plagioclase feldspar and 0.98 mm olivine. The average grain shape is subhedral (olivine, clinopyroxene, plagioclase feldspar and alkali feldspar) and anhedral (Fe-Ti oxides). The mineralogical composition of the plagioclase feldspar is Labradorite (An_{50-70}) with sporadic Bytownite (An_{70-90}). At some plagioclase feldspar grains, on sample number RP-10, there are inclusions of olivine and pyroxenes and show oscillatory zoning. Sample number RP-7 show olivine grains which are highly fractured and show skeletal structure; the crystal occupying the bulk has acomplex interior form. There are some olivine grains in thise sample that show oscillatory zoning. The groundmass is microcrystalline that mainly composed of olivine, plagioclase feldspar and Fe-Ti oxides.

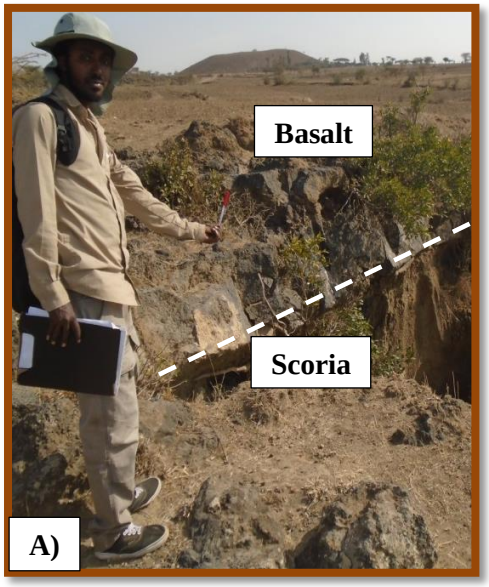

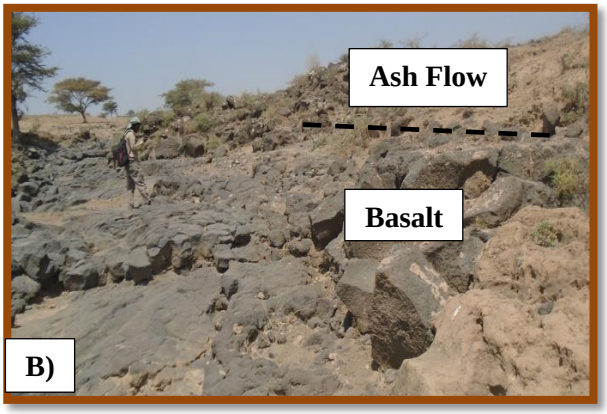

Figure 3.16: *The lower basalt that underlain by scoria (**A**), overlain by Upper ash flow (**B**) and show polygonal joints (**C**).*

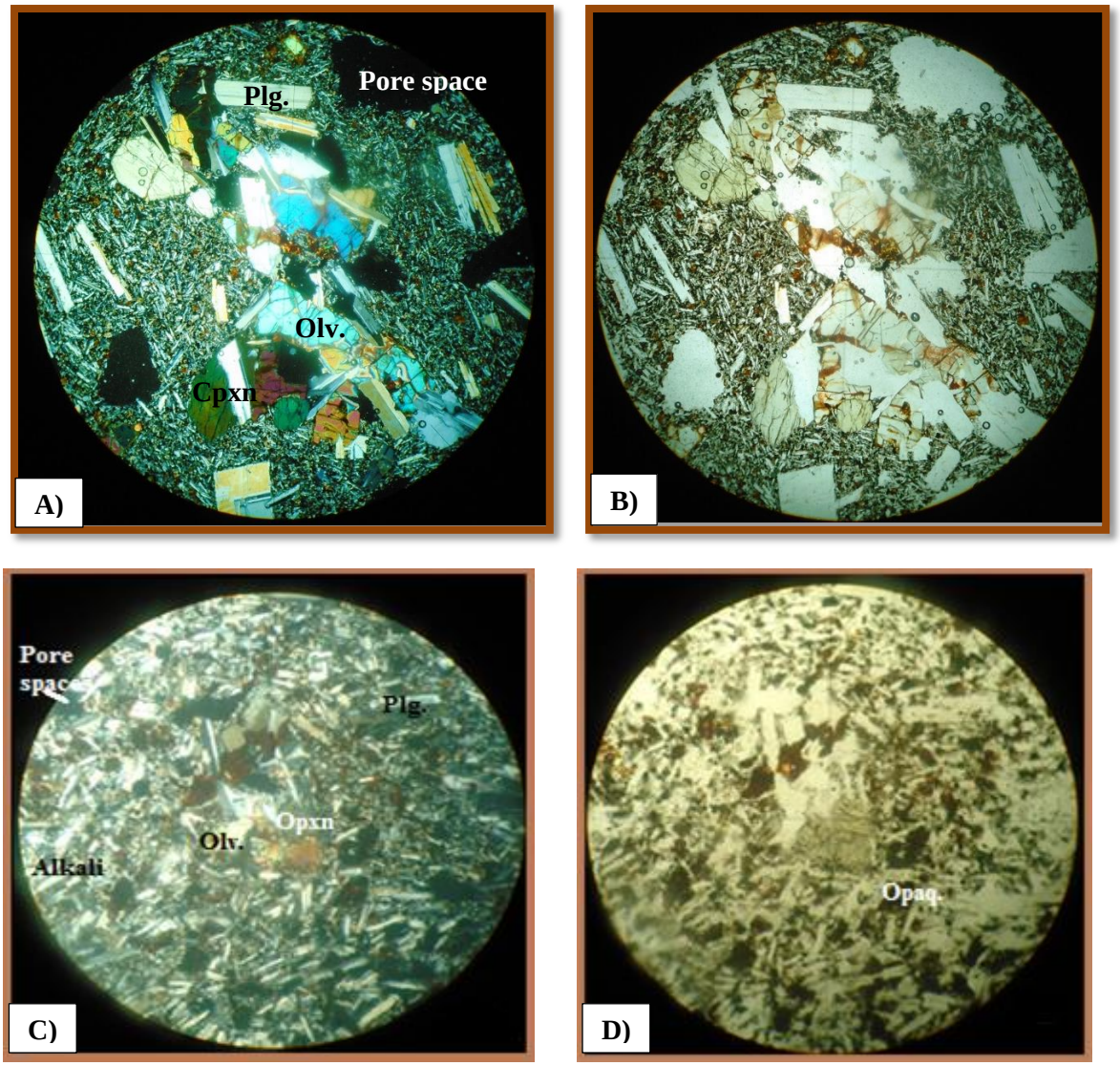

Figure 3.17: *Microphoto picture of lower basalt sample; RP-7 (**A** & **B**) and RP-10 (**C** & **D**) under optical microscope in XPL view (**A** & **C**) and PPL view (**B** & **D**). The labels stands for; Olv-Olivine, Plg.-Plagioclase feldspar, Alkali-Alkali feldspar, OPxn-Orthopyroxene, Cpxn-Clinopyroxene and Opaq.-Fe-Ti Oxides. The photo picture is taken at 10X magnification.*

3.2.7. Ash Flow and Ash Fall

Pyroclastic ash is the main lithological unit that enormously cover the study area in plan view. Relative to the other geological units, ash has a large proportion in area coverage and form a gentle slope to flat plane. In addition to that, this unit is very thin and intercalated with different units. The pyroclastic ash exposed in the area are on the big sections of the Boko ridge, Dabe section and on the caldera floor outcroped by deep

gullies. By their physical characteristics, they are classified into two; ash flow and ash fall. Their field description is described in the following paragraphs.

Ash flow deposit is one type of lithology which mainly composed of ash size (< 2 mm) tephras. Thise unit is exposed on one position of the composite stratigraphy. But in field there is another unit of ash flow that intercalate with the pumice flow (see Fig.3.18 (C) and (D)) which named as lower ash flow. Lower ash flow has a maximum thickness of 0.7 m, that is exposed on Boko section. The upper ash flow; that presented on the composite stratigraphy is exposed by overlaying the lower basaltic lava flow (see Fig.3.18 (B)) and thin alluvial sediments on western part of the study area (with maximum thickness of 0.5 m). The upper ash flow have 12 m maximum vertical thickness. Generally the two have a common characteristics of pale yellow color, show moderate welding, poorly sorted, have lithic fragment and show variation in vertical thickness. The lithic fragment is mainly composed of basalt, obsidian and rhyolite. The size of the lithics is vary between 2 to 3 mm. In one river cut exposure located on the northwestern part of the area the upper ash flow deposit show an accretionary lapilli (see in Fig.3.18 (A)).

Ash fall deposit is the second type of pyroclastic deposit which is composed of ash sized tephras. The deposit is not presented in the composite stratigraphy because of having small thickness. But the ash fall exposed on two stratigraphic position; lower ash fall and upper ash fall. The lower ash fall is exposed by intercalating with pumice fall unit (see Fig.3.6 (B)) and the upper ash fall is exposed by intercalating with ash flow deposit. All ash fall deposit show a similar characteristics of pale yellow to grey color, well sorted, loosely welded and have consistent local thickness. On both upper and lower ash fall; the unit has a maximum thickness of 1 m.

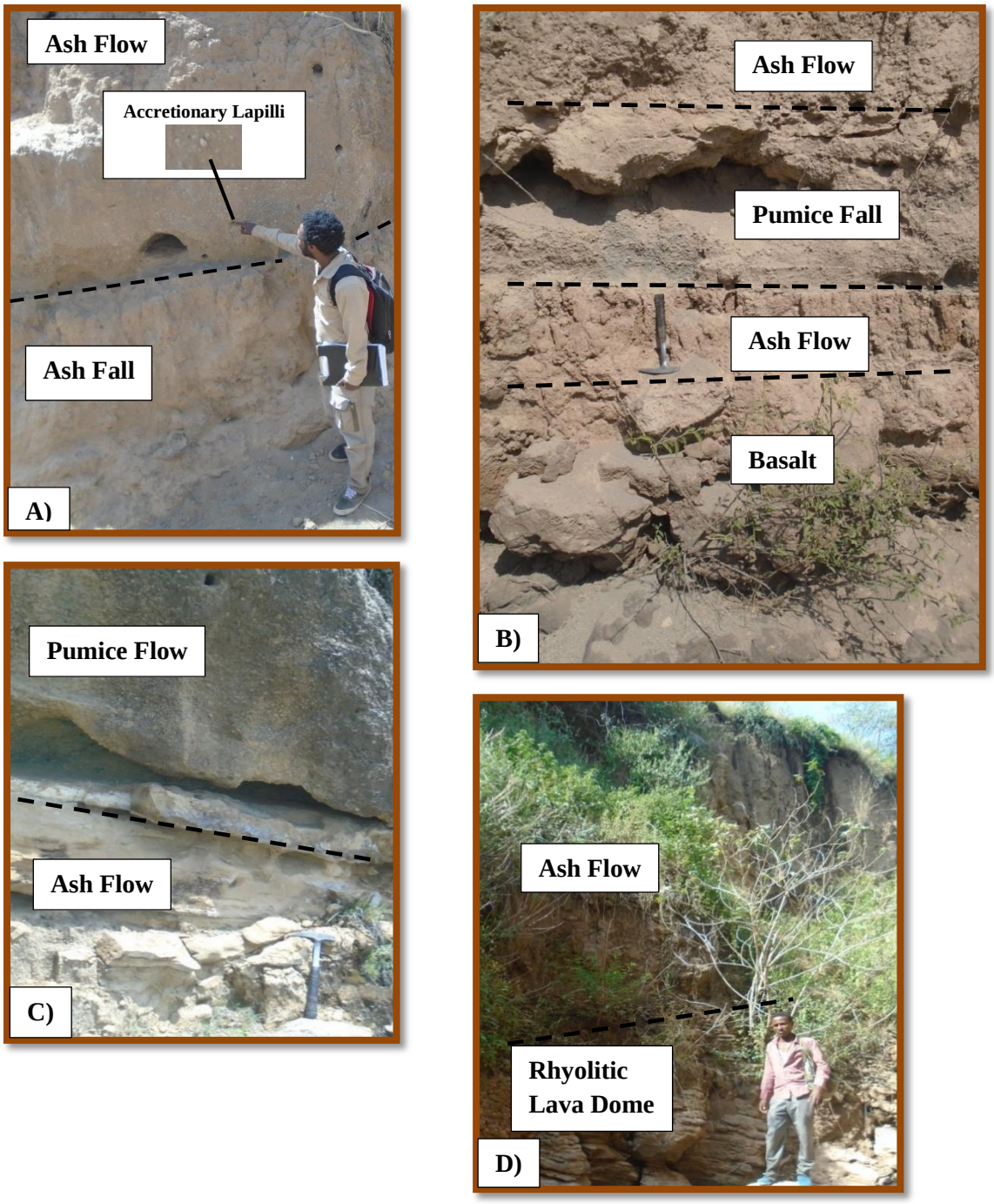

Figure 3.18: *Ash flow deposit showing interbedding with different types of rock units. In exposure "**B**" the ash flow, that overlay the lower basalt, show increament in vertical thickness from 0.7 m to 1.2 m toward the right side of the exposure (down the stream toward south west direction).*

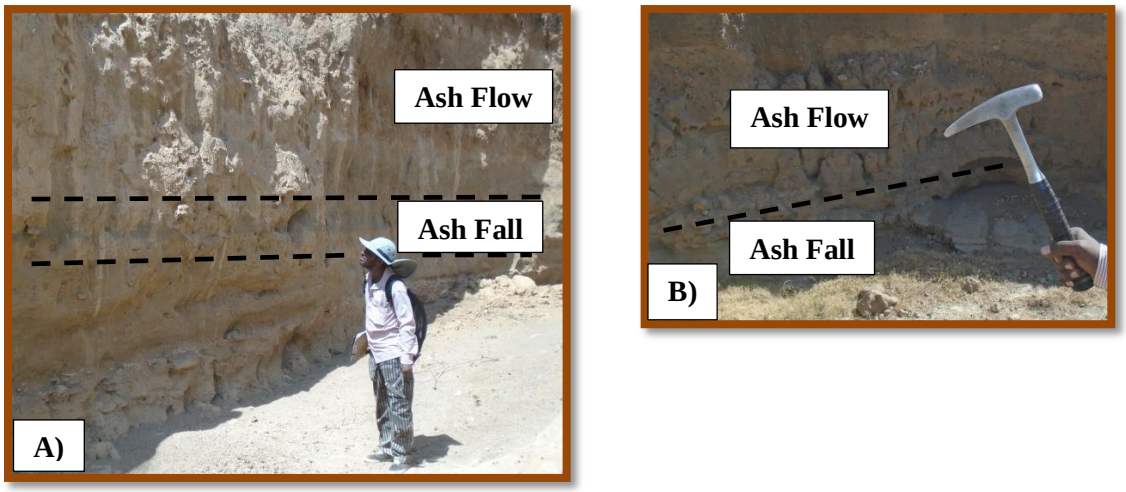

Figure 3.19: *Ash fall deposit that intercalated with ash flow which have been exposed by a stream.*

3.2.8. Upper Basalt and Scoria

Upper basalt is the youngest product among the volcanic rocks found in the Boko magmatic complex. The upper basalt is found in the composite stratigraphy by overlaying scoria. These two varieties are easly identifiable on a topographic map; form a cone like structure with a gentler slope on one side of the cone. The cone is made of scoria while gentle slope is formed by the associated basaltic lava flow. Generally, most cones show elliptical geometry with there longest dimension on NE-SW direction in agreement with the regional tectonic direction indicating that their eruption is controlled by preexisting structures. Except scoria cones that exposed on the south eastern part of the study area show a major axis along east-west direction. The nature of the contact between the two varieties is gradational that means the fragmentation of the scoria become less (well indurated) near to the contact while the basalt become fragmented near to the contact. The detail rock description of the two varieties is described in the following paragraphs.

Scoria is one variety of lithological unit exposed in the study area. The rock is mainly outcroped on cliff type exposure. Quarry type of exposures are also observed due to excavation activities for the purpose of cement factory production as a raw material and aggregates for gravel roads on near by localities. A typical example for quarry type exposure is on the Dera scoria cone (Fig.3.20 (A)) that exposed 40 m vertically thick

scoria deposit. In this exposure the rock is highly fragmented with maximum fragment size of 12 cm, redish in color and show grain size stratification.

Figure 3.20: ***A****) Exposure in a quarry at the Dera scoria cone.* ***B****) Black scoria and 15 m by 20 m dimension crater near the village Enyur.*

Rocks with similar characteristics is observed on others scoria cones. The only exception is the scoria exposed on south eastern side of the study area on the village Enyure and its surrounding. The rock exposed in this area is black colored (Fig.3.20 (B)). There is a crater stracture that looks like the vent for the magmas flow out to form the rock unit. The crater (see Fig.3.20 (B)) has elliptical structure with a dimension of 15 m by 20 m. The rock is very fresh and young (by examining its physical characteristics) relative to the other rock exposed on the rest of the study area.

Upper basalt is another variety of lithological unit that associated to scoria. This unit form a clear sharp contact with the underlying scoria and ash flow deposit that cover the flat land of the area (Fig.3.21 (D)). The basaltic rock unit that is found adjacent to Boko ridge shows the following characteristics; porphyritic texture, dark-grey color, vesicular apearance (with iregular structured vesicles), some vesicles are filled by whitish secondary minerals and black with white spots weathered color. The phenocryts are mainly composed of plagioclase feldspar, olivine and pyroxene. Similar rock unit is exposed on the Dera scoria cone (Fig.3.21 (A)) and other scoria cones found in the study area except the scoria cone located eastern margine of Dabe section. The scoria cone

located east of Dabe section has a unique characteristics of plagioclase feldspar and pyroxene phenocryst rich with no or scarce olivine phenocryst. The maximum thickness of this unit is 2 m.

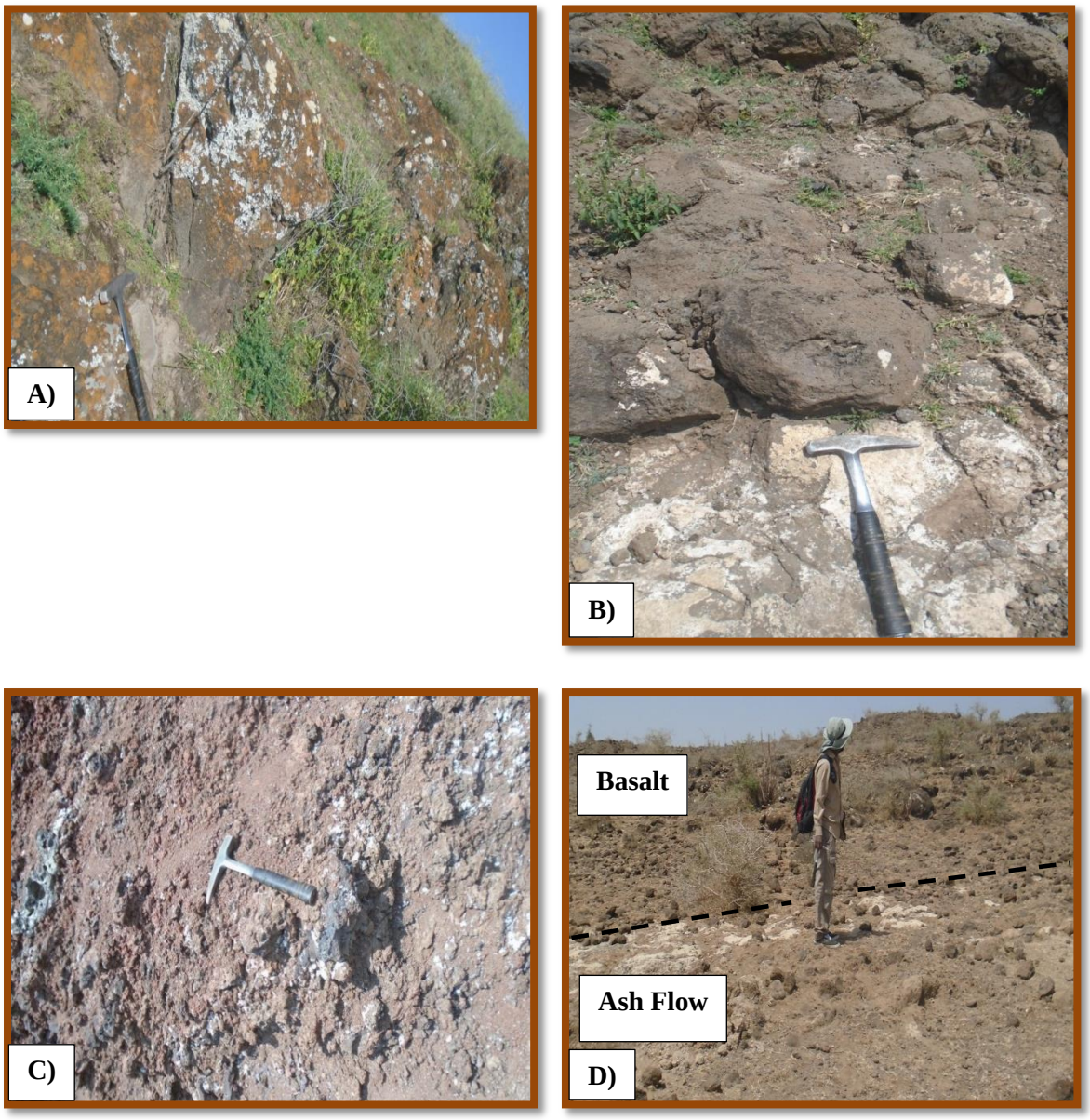

Figure 3.21: ***A)*** *Upper basalt on the Dera scoria cone.* ***B)*** *Vesicular basalt with plagioclase feldspar, pyroxene and scarce olivine phenocryst that are found on the south eastern part of the area.* ***C)*** *Close look of scoria that is found together with the vesicular basalt on "****B****". **D)** Upper basalt on top of ash flow that is found on south eastern part of the study area.*

Two samples collected from upper basalt are prepared for petrographic analysis by considering their variation in mineralogy. The sample codes are RP-4 and RP-6. The

samples show a serieate texture (see Fig.3.22). This type of texture is a porphyritic texture in which the phenocrysts show a wide range of grain size. The phenocryst is dominantly plagioclase feldspar with modal proportion of 31% and there are also 1% alkali feldspar, 1% orthopyroxene (only observed on RP-4), 1-2% clinopyroxene, 4 & 12% Fe-Ti oxides and 9 & 12% olivine. The maximum grain size along the longest length of the phenocrysts are 0.1 mm Fe-Ti oxides, 0.14 mm orthopyroxene, 0.16 mm alkali feldspar, 0.2 mm clinopyroxene, 0.9 mm olivine and 1.5 mm plagioclase feldspar.

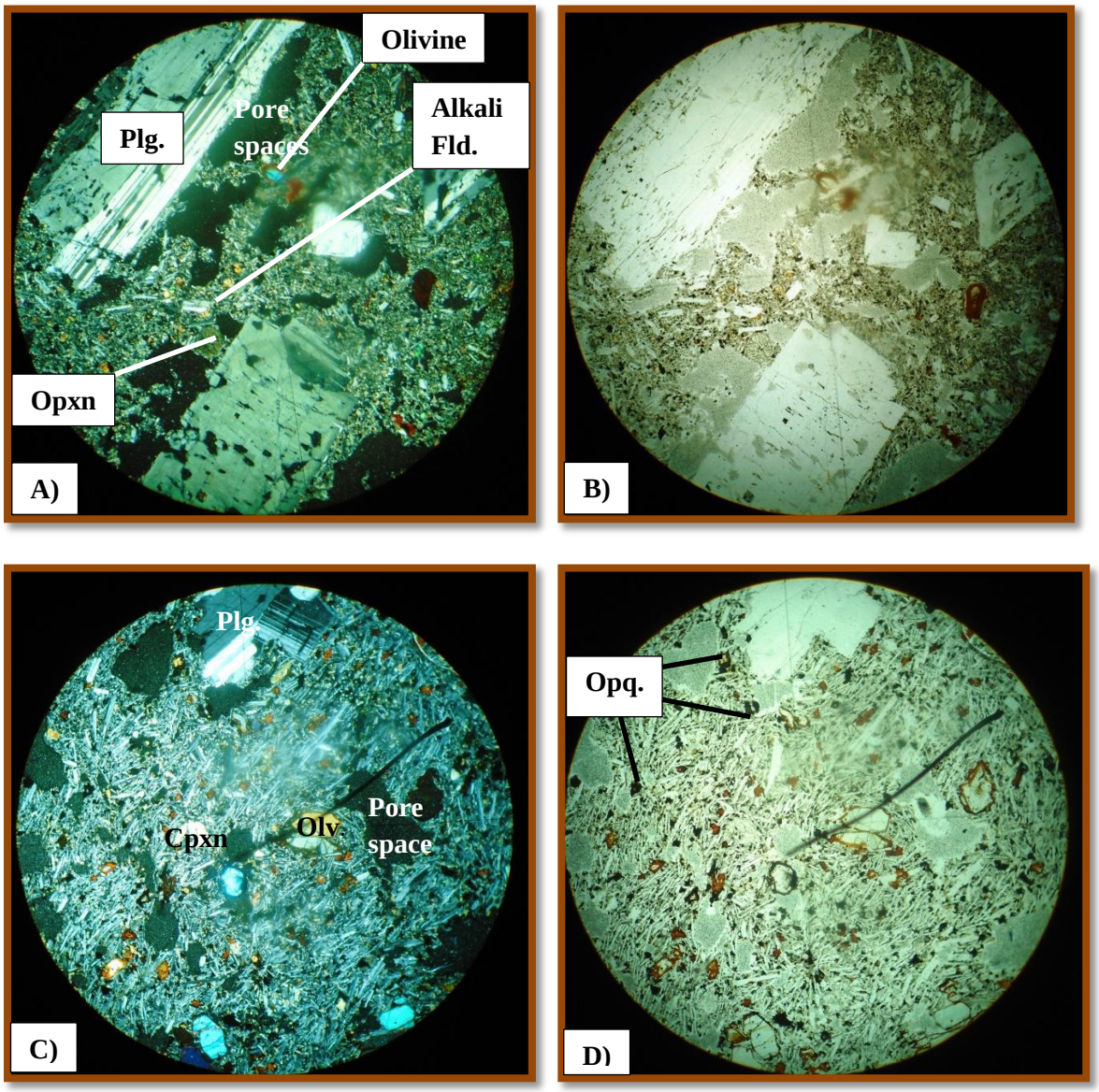

Figure 3.22: *Microphoto picture of upper basalt sample; RP-4 (**A** & **B**) and RP-6 (**C** & **D**) under optical microscope in XPL (**A** & **C**) and PPL (**B** & **D**) view. The labels stands for; Plg.-Plagioclase feldspar, Alkali Fld.-Alkali feldspar, OPxn-Orthopyroxene and Opq.-Fe-Ti Oxides. The photo taken at 10X magnification.*

Grain shape of the phenocrysts show anhedral (olivine, clinopyroxene, orthopyroxene and Fe-Ti oxides) and subhedral (alkali and plagioclase feldspar). The plagioclase feldspar is dominantly composed of andesine (An_{30-50}) and oligoclase (An_{10-30}). The Plagioclase feldspar shows a clear oscillatory zoning by compositional changing from andesine to oligoclase. On sample number RP-4 some grains of plagioclase feldspar has poor alignment, bleb-like inclusions of alkali feldspar called anthiperthitic texture (see on Fig.3.22 (A) and (B)). On sample number RP-6 some of the plagioclase feldspar show sieve texture because of inclusion of olivine and Fe-Ti oxides in the mineral grain. Generally on the two samples olivine and pyroxene grains are altered into opaque minerals dominantly visible on the rim of the mineral grains. The groundmass modal proportion ranges between 33-48%; it is composed of microcrystals of the phenocryst (dominantly Fe-Ti oxides, plagioclase feldspar, olivine and pyroxenes).

3.3. Geological structures

3.3.1. Introduction

Since the Boko magmatic complex (BMC) is located in the axis of the Main Ethiopian Rift (MER) the area predominantly shows tectonic structures. The tectonic structures encountered in the area are formed by the extensional force that is oriented regionally along a general east-west direction (Bonini et al., 2005). In general, the geological structures observed in the area are classified mainly into two; primary and secondary.

The primary geological structures are structures that are formed during the rock formation process. An example of a primary structure is flow banding and layering on pyroclastic deposits. The secondary structures are structures formed by a process that transpired on the rock after the rock formation process. The structures under secondary structures are joints and faults. The primary structures are discussed with the lithological unit description section while in this section the secondary structures are described.

3.3.2. Joint

Joint is fracture which has no or insignificant relative displacement between the blocks found on the two side of the fracture. This structure is predominantly observed on rhyolitic lava flow, pumice fall and lower basalt units.

The joint that observed on the lower basalt is polygonal joint. The polygonal joint has a y-intersection (see on Fig.3.16 (C)).

The joint that is observed on the rhyolitic lava flow has a general orientation of NE-SW strike (some SE-NW present) and vertical to sub vertical dip amount, the dip direction fall on the SE direction (and some NE, see Fig.3.23 (A)). On the pumice fall, the general orientation of the strike is NE-SW (some NW-SE) and vertical to sub vertical dip amount (see on Fig.3.23 (B)). The orientation measurements of all joints are presented on Appendix II. Generally the orientation is NE-SW and NW-SE (see the stereo net analysis in Fig.3.23 (C)). Maximum aperture measured in the field is 60 cm.

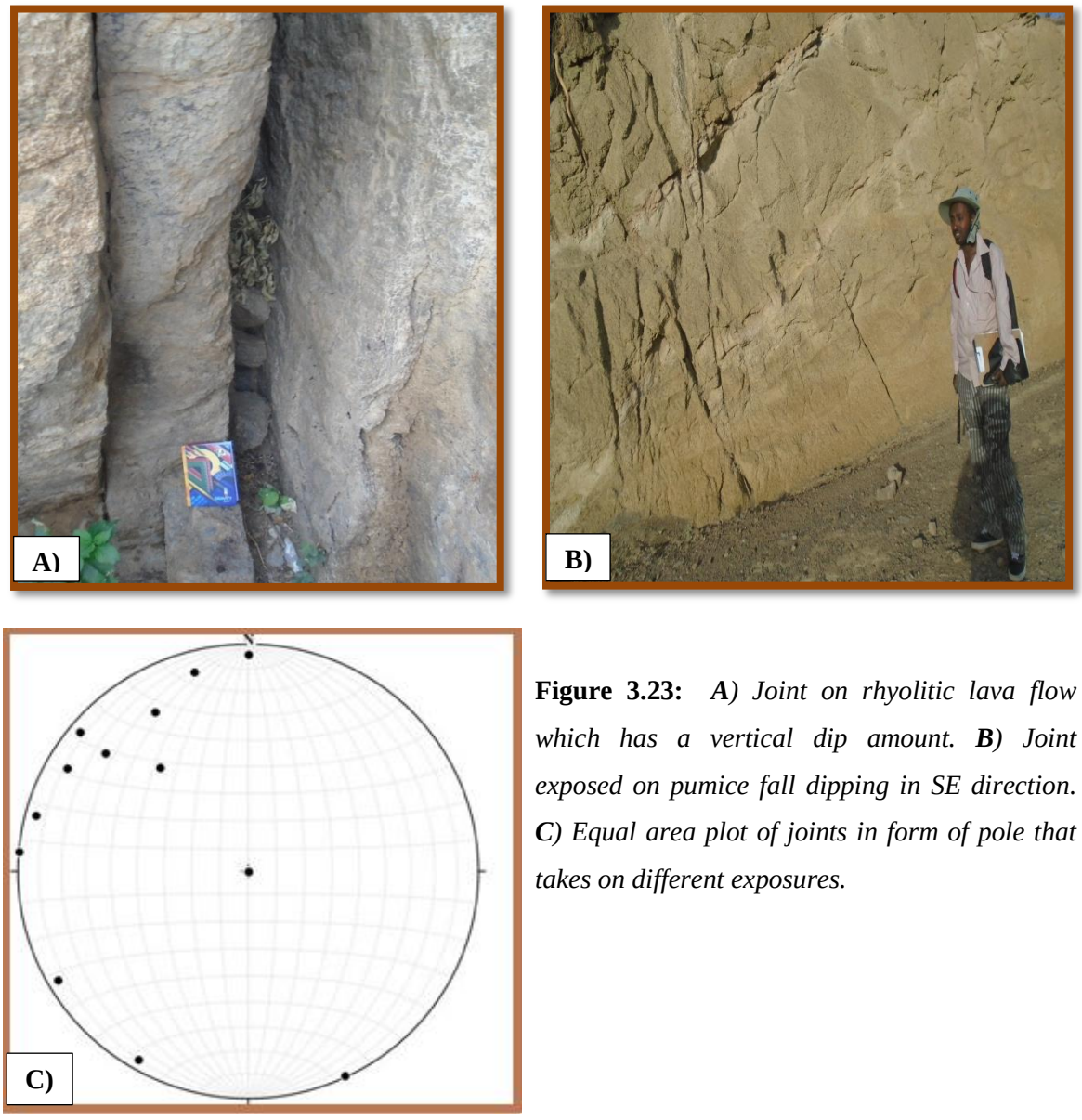

Figure 3.23: ***A)*** *Joint on rhyolitic lava flow which has a vertical dip amount.* ***B)*** *Joint exposed on pumice fall dipping in SE direction.* ***C)*** *Equal area plot of joints in form of pole that takes on different exposures.*

3.3.3. Fault

Normal Fault is the other predominant structure in the area. It is the main path way for the flow of gas and the hot fluids in addition to the joints and the flow bands. It encountered on varieties of rock types; on rhyolitic lava flow, rhyolitic lava dome, lower basalt and upper basalt.

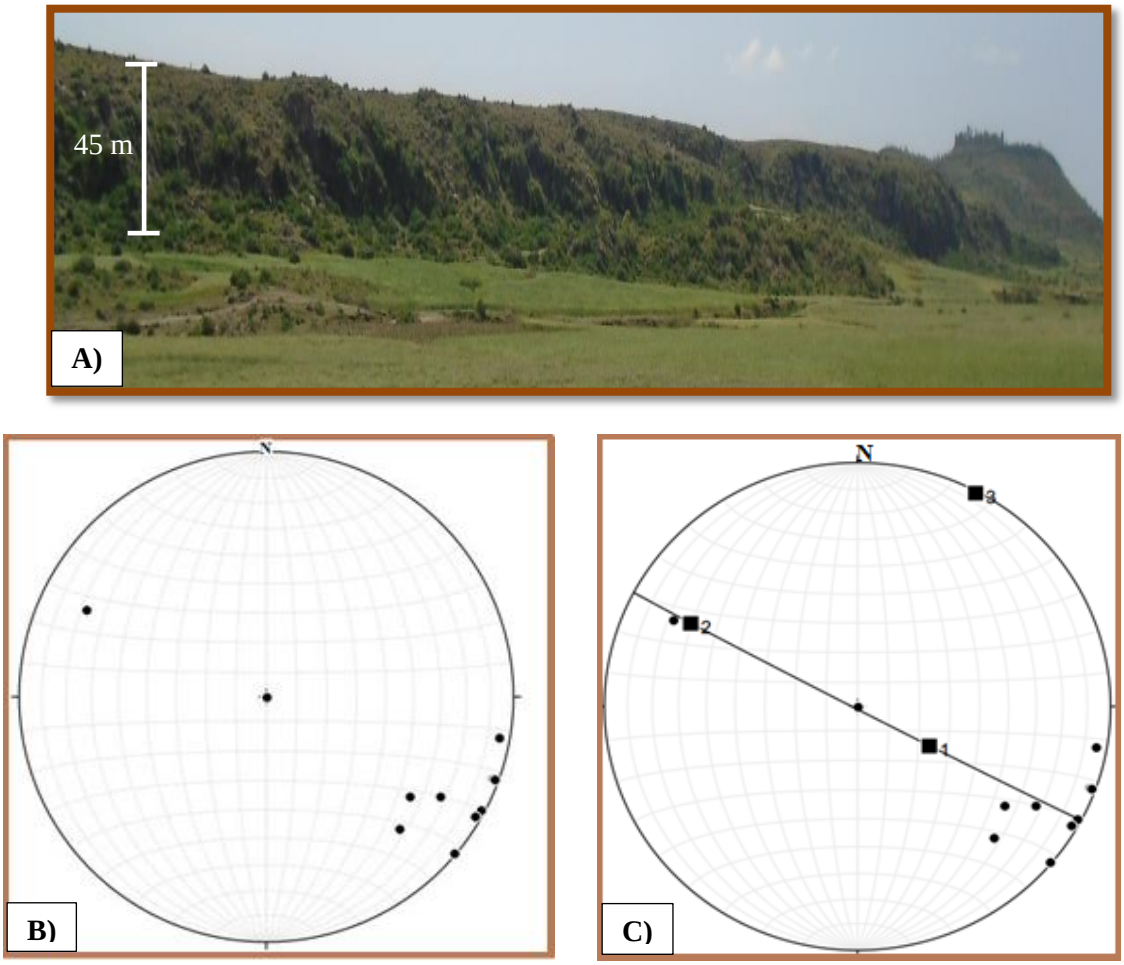

Figure 3.24: ***A****) Photo picture of major normal fault cutting rhyolitic lava flow, the fault dip direction is SE.* ***B****) Equal area plots of faults in form of pole that takes on different locations. C) Best fit line plot of the fault measurement in form of pole which show orientation of* 028^0 *strikes and* 90^0 *dip.*

The faults encountered in the axis of the MER are formed during the caldera collapse and by the younger extension that concentrated on the Wonji fault belts (Bonini et al., 2005). The fault formed by the collapse activity forms a ring or circular geometry. But the fault

formed recently after the collapse displaces the ring faults. The orientations of the recent fault are NE-SW trending strike and dip direction of NW or SE (see on Fig.3.24). Fig.3.24 (C) shows the best fit great circle, from the stereographic projection analysis, 028^0 regional orientation of the faults. In most of the area the faults form a half graben. But in one area a 250 m wide full graben is observed that is bounded by two NW and SE dipping major faults. The graben is filled by pyroclastic material especially ash flow. The full data are presented on appendix II and structural map on Fig.3.25.

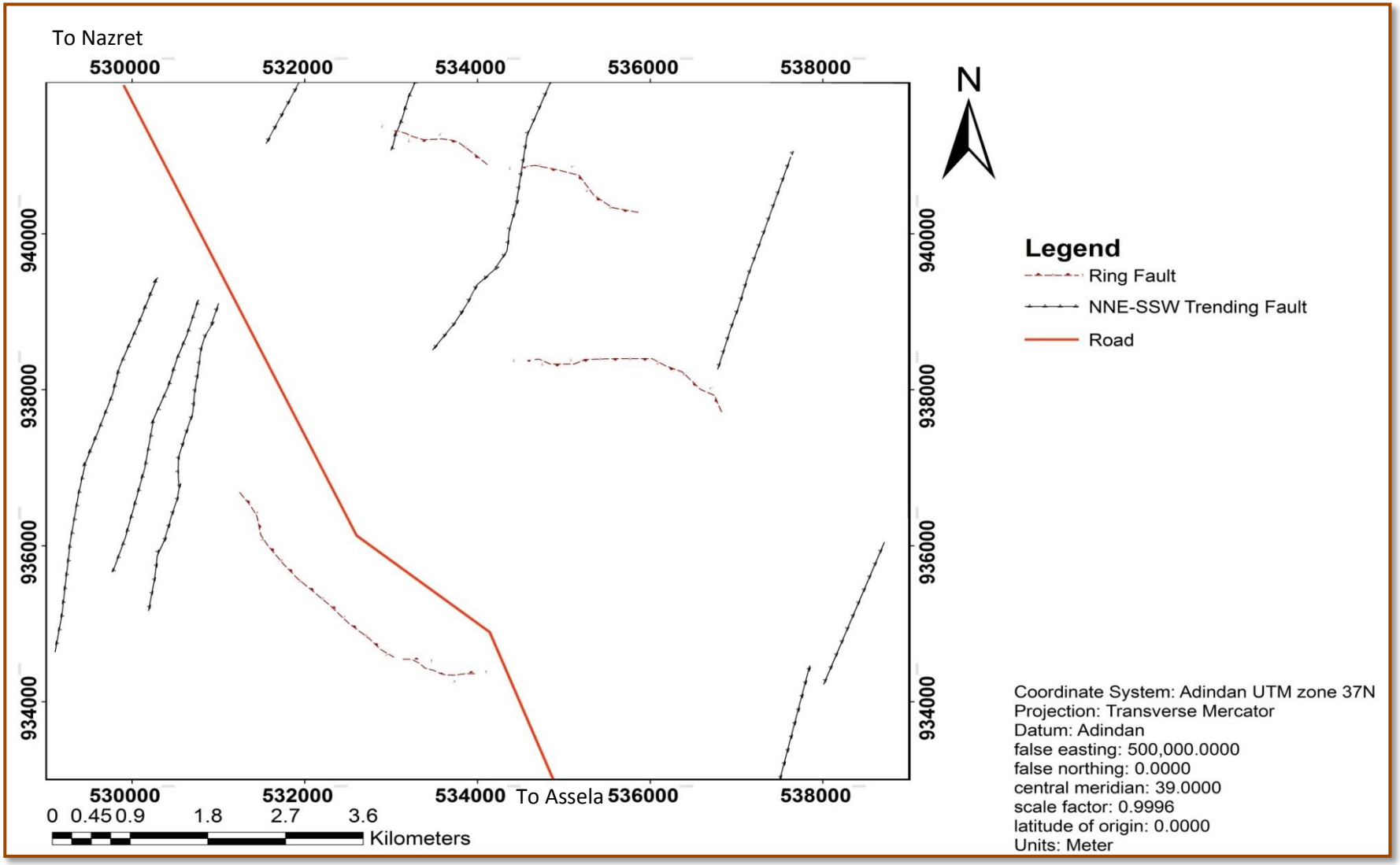

Figure 3.25: *Fault map of the study area.*

Chapter Four

4. Geochemistry

4.1. Introduction

Geochemistry is common method used to study the magmatic evolution of any volcanic product. This method mainly depends on the relative signature of the elemental composition that enables to understand the geologic process. Nowadays the geochemical data is processed by different software.

Four major types of geochemical data are identified according to Rollinson (1993); major, trace, volatile and isotope. From the four types only three of them (major, trace and volatile) are used in this study. Mainly major and trace element geochemical data types are used to understand the evolution. But the volatile, which is presented by Loss of Ignition (LOI) used only to know the behavior and alteration effect on mobile elements concentration that is well explained below. LOI represents the total volatile content of the rock that is determined by igniting the rock with temperature of 1000 ^{o}C (Rollinson, 1993).

The total numbers of collected samples for the geochemical analysis purpose are thirty (10-rhyolite, 2-ignimbrite, 4-obsidian, 6-pumice, 8-basalt & scoria). The sample location and geochemical result is presented on Fig.4.1 and Table.4.1 respectively. The samples are carefully prepared in powder form in Addis Ababa University School of Earth Sciences Milling room. The powdered sample is analyzed by analytical method of Inductively Coupled Plasma Optical Emission Spectroscopy (ICP-OES) for major element-LOI analysis result and Inductively Coupled Plasma Mass Spectroscopy (ICP-MS) for trace element. Major element is analyzed by ICP-OES. Because the sample introduced into the ICP is in liquid form solid samples has converted to liquid by dissolving it into proper solvent. The solvent is ultra-pure HNO_3 and dried at 160 ^{o}C. The first process called nebulization where sample is converted to a mist of finely divided droplet called aerosol, where the sample is sucked into capillary tube by a high pressure stream of Argon gas flowing around the tip of the tube. This pressure breaks the liquid

into fine droplets in various sizes in the spray chamber. In the spray chamber, separation of aerosol occurred where the large droplets go to drain the fine droplet carried to the plasma. The sample mist reaching the plasma is curiously dried, vaporized, and energized through coalitional excitation at high temperature (up to 8000 K). In this case, the atomic emission emanating from the plasma is viewed in either a radial or axial configuration, collected with a lens or mirror, and imaged onto the entrance slit of a wavelength selection device. The instrument runs will include an initial calibration verification solution and a blank solution at the beginning and end of every run. A calibration verification solution will be analyzed after every 10 samples throughout the run. The verification measurements (Standard Reference Material 2780) must be within 10 percent of the expected value. If they are not, the problem should be corrected before continuing with next analyses.

Trace element is analyzed by ICP-MS. ICP-MS is the most accepted tool for trace element and isotopic analysis (Rollinson, 1993). The acceptability in the science is due to its detection limit is low, high accuracy and high precision. In similar to ICP OES the sample is introduced after changing in liquid form by using HNO_3. Ions are extracted from the plasma through a pin-hole sized loop into a pumped vacuum system and focused with an ion lens into a mass spectrometer. Once the ions enter the mass spectrometer, they are separated by their mass-to-charge ratio. The result is that an electrostatic filter is established that only allows ions of a single mass-to-charge ratio (m/e) pass through the rods to the detector at a given instant in time. The relative standard deviation (RSD) of the instrument is 1-2% with comparing to calibration solution of a multi-element doped solution. Matrix extraction prior to the analysis of trace elements in geochemical materials was used to remove possible isobaric interference and, eliminate signal suppression in the plasma.

From the geochemical analysis the result are mainly volatile, major and trace elements concentration data. To use for the research purpose the data must be integrated or synthesized. The data integration is done by a software packages; Microsoft excel 2010 and Petrograph version 2beta. The outputs from the software are in the form of graphs that help to understand mainly the magmatic evolution of the magmatic complex by depending on those representative geochemical samples. In addition to primary

geochemical data there are some secondary data adopted from previous works (Boccaletti et al., 1999; Tadiwos Chernet, 1995) that were done on the surrounding of Boko magmatic complex (BMC) for comparison.

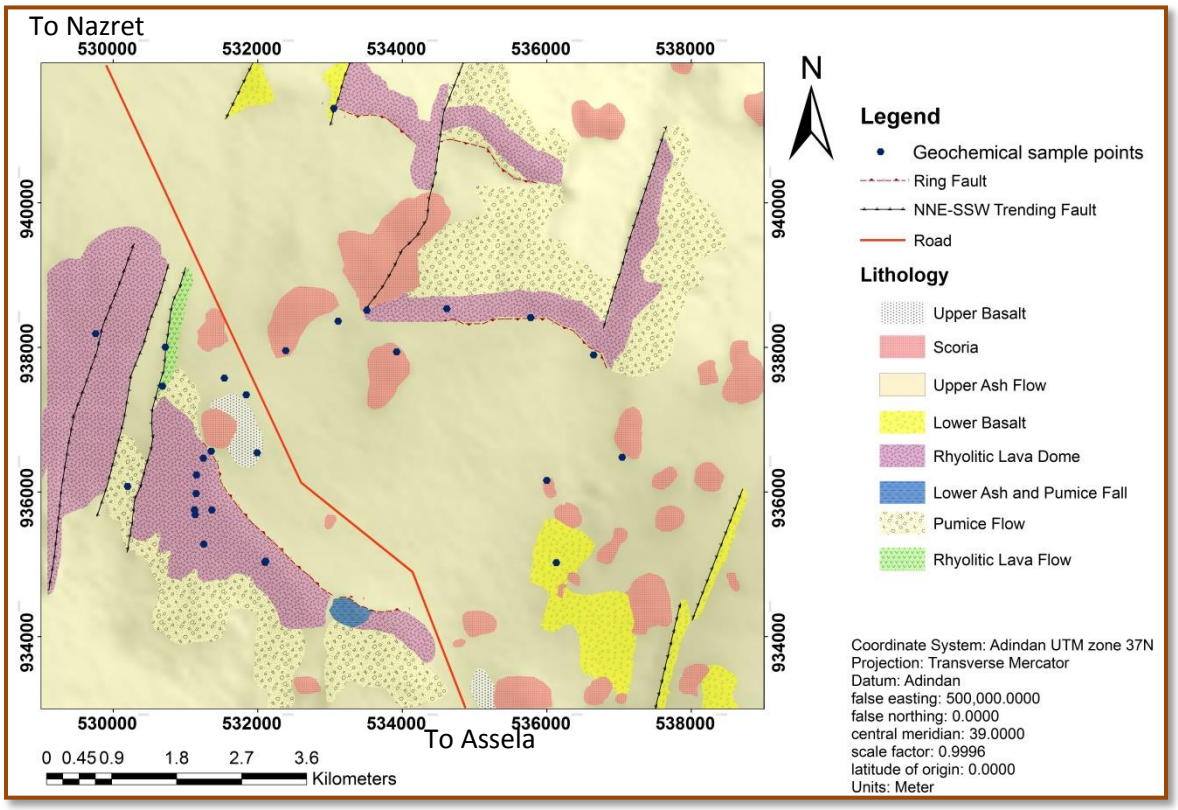

Figure 4.1: *Distribution and location of samples that are collected for geochemical analysis from different rock units.*

From the total of thirty samples the six samples show a high value of LOI. The samples that show LOI>5wt. % are collected from pumice flow and fall unit. In those samples the value of Na_2O is minimum (<2wt. %) relative to other felsic rock samples that are presented on the total alkali silica (TAS) classification plot. The LOI enrichment is usually occurred by post deposition alteration process (Peccerillo et al., 2003; Fontijn et al., 2013 in Hutchison, 2015). The effect of the volatile enrichment is checked by comparing selected mobile and immobile elements trend by plotting them with LOI in binary diagram. The trend of mobile major element for example Na_2O against LOI has a very slight negative correlation (Fig.4.2). In contrast to this the immobile elements, for example Al_2O_3, plot with LOI show no variation in the samples (Fig.4.2). This trend indicates to use volatile rich samples for interpretation with caution.

Table 4.1: *Geochemical analysis result of BMC samples. On the table the notation stands for LD- Detection Limit. The major element (including LOI) and trace element value of concentration is expressed by wt. % and ppm respectively. The geochemical data is normalized in volatile free base.*

	NBS2.2-R4 Rhyolite	**NBS2.2-R2 Rhyolite**	**NBS2.2-R3 Rhyolite**	**NBS1.1-TR1 Rhyolite**	**NBS2.2-R1 Rhyolite**	**NBS4.1-R1 Rhyolite**	**NBS3.1-R3 Rhyolite**	**NBS1.2-RT2 Rhyolite**	**NBS3.1-R1 Rhyolite**	**NBS3.1-R2 Rhyolite**
E (m)	0531840	0531149	0531124	0532099	0531246	0533509	0529755	0531364	0531537	0530721
N (m)	0937344	0936234	0935753	0935027	0936467	0938512	0938191	0935749	0937575	0938005
SiO_2	75.45	71.12	70.23	70.9	71.65	74.7	73.3	73.16	75.4	73.13
TiO_2	0.19	0.44	0.5	0.44	0.42	0.26	0.19	0.39	0.20	0.19
Al_2O_3	10.88	11.61	11.53	11.02	10.59	9.47	13.68	9.97	10.96	13.66
FeO_t	4.09	6.46	5.62	5.76	5.86	5.17	2.29	6.34	4.08	2.32
MnO	0.10	0.25	0.31	0.33	0.38	0.17	0.02	0.3	0.04	0.07
MgO	0.05	0.10	0.25	0.13	0.19	0.07	0.07	0.07	0.06	0.10
CaO	0.12	0.15	0.34	0.34	0.44	0.29	0.18	0.33	0.22	0.21
Na_2O	3.8	4.22	5.83	5.85	5.19	4.88	4.91	4.22	3.53	4.94
K_2O	4.87	4.92	4.75	4.59	4.64	4.43	5.1	4.52	5.04	5.11
P_2O_5	< L.D.	< L.D.	< L.D.	< L.D.	< L.D.	< L.D.	< L.D.	< L.D.	< L.D.	< L.D.
Total	99.55	99.27	99.36	99.36	99.36	99.44	99.74	99.30	99.57	99.73
LOI	0.85	1.53	0.65	0.43	0.81	0.73	0.88	1.52	1.74	0.44
Be	6.035	5.052	4.873	5.02	4.647	8.043	3.843	5.07	5.267	4.175
Sc	< L.D.	5.47	8.19	6.08	5.13	< L.D.	3.61	< L.D.	< L.D.	3.8
V	4.532	1.863	2.861	1.434	1.608	2.037	3.992	0.955	6.634	5.152
Cr	24.92	19.83	26.87	17.13	63.05	54.76	31.35	15.31	24.96	50.92
Co	0.386	0.274	0.332	0.209	0.365	0.365	0.269	0.152	0.119	0.405
Ni	< L.D.	< L.D.	< L.D.	< L.D.	< L.D.	< L.D.	< L.D.	< L.D.	< L.D.	< L.D.
Cu	< L.D.	< L.D.	< L.D.	< L.D.	< L.D.	13.4	< L.D.	< L.D.	< L.D.	< L.D.
Zn	176.4	192.9	197.9	211.2	215.7	261	87.97	245.8	189.7	83.54
Ga	32.69	35.12	32.7	32.21	31.51	31.52	26.19	31.68	31.73	25.92
Ge	2.092	2.205	2.569	2.598	2.656	2.695	1.869	2.469	2.069	1.926
As	1.874	< L.D.	1.701	< L.D.	< L.D.	2.121	1.531	< L.D.	1.66	1.708

Rb	197.5	118	109.4	107.9	118.1	199.1	129	131.1	195.3	127.3
Sr	8.33	8.924	7.062	5.131	13.84	7.829	12.16	5.727	13.53	11.73
Y	97.57	97.45	55.61	86.34	64.75	89.1	45.96	60.53	96.69	52.12
Zr	980	729.7	662.3	660.4	684.7	958.5	557.4	791.4	946.2	544.5
Nb	108.4	94.61	86.59	86.68	87.79	145.6	57.02	108.4	106	55.74
Mo	1.137	0.793	1.5	1.179	0.781	0.924	2.769	1.393	1.072	2.888
Cd	0.712	0.517	0.477	0.559	0.46	0.938	0.304	0.618	0.586	0.293
In	0.132	0.227	0.208	0.208	0.203	0.181	< L.D.	0.205	0.163	< L.D.
Sn	10.42	6.956	5.925	6.109	6.209	10.23	5.968	7.852	8.543	5.018
Sb	0.232	0.156	0.142	0.156	0.217	0.322	0.168	0.124	< L.D.	0.165
Cs	0.402	0.175	0.659	0.88	0.439	1.442	0.615	0.319	0.269	0.751
Ba	46.5	228.6	374.1	267.9	348	26.74	345.5	280.5	19.41	346.4
La	75.94	117.6	75.43	90.7	76.06	90.46	66.12	68.48	106	64.1
Hf	27.19	17.39	15.97	15.8	16.56	26.69	14.12	21.41	26.18	13.59
Ta	8.431	6.952	6.481	6.426	6.663	10.49	4.473	8.067	8.117	4.361
W	< L.D.	0.937	1.213	1.006	< L.D.	0.959	< L.D.	0.979	< L.D.	1
Pb	28.9164	17.598	15.2845	13.3516	15.947	27.5783	13.2812	21.7491	14.5133	13.4227
Bi	< L.D.	< L.D.	< L.D.	< L.D.	< L.D.	< L.D.	< L.D.	< L.D.	< L.D.	< L.D.
Ce	234.1	202.1	160.6	158.4	199.8	219	95.39	215.1	210.5	133.1
Pr	20.8	29.32	20.12	21.03	19.73	19.15	16.22	18.98	25.72	15.08
Nd	76.43	109.1	74.51	78.73	74.05	68.38	57.06	69.12	93.18	53.64
Sm	18.23	20.96	14.82	15.88	14.83	13.78	10.55	14.01	20.01	10.24
Eu	1.438	4.475	3.383	3.626	3.262	1.494	0.899	2.943	1.322	0.853
Gd	16.94	17.03	11.83	14.47	12.59	12.96	8.066	11.4	17.42	8.541
Tb	2.983	2.832	1.925	2.363	2.057	2.244	1.342	2.012	2.815	1.4
Dy	19.34	17.98	11.82	14.9	12.89	15.11	8.343	13.18	17.37	8.83
Ho	4.064	3.76	2.338	3.13	2.682	3.292	1.75	2.786	3.681	1.877
Er	10.88	10.03	6.19	8.348	7.218	9.104	4.901	7.881	9.896	5.181
Tm	1.634	1.461	0.937	1.233	1.058	1.369	0.746	1.217	1.451	0.773
Yb	11.22	9.846	6.539	8.49	7.132	9.585	5.249	8.716	9.737	5.39
Lu	1.684	1.519	1.047	1.338	1.124	1.522	0.83	1.347	1.471	0.841

Th	21.85	13.92	12.92	12.62	13.82	24.33	14.09	16.98	21.18	13.67
U	1.691	0.971	1.618	1.563	2.525	1.126	2.576	0.868	2.443	2.367

	NBS2.2-O2 Obsidian	**NBS4.1-O1 Obsidian**	**NBS1.2-O1 Obsidian**	**NBS2.2-O1 Obsidian**	**NBS4.1-i1 Ignimbrite**	**NBS2.2-i1 Ignimbrite**	**NBS1.1-P2 Pumice**	**NBS1.1-P1 Pumice**	**NBS2.2-P1 Pumice**	**NBS2.2-P2 Pumice**
E (m)	0531124	0535776	0531133	0531146	0533111	0530198	0532106	0532106	0530679	0530679
N (m)	0935753	0938413	0935686	0935979	0938363	0936077	0935043	0935043	0937464	0937464
SiO_2	70.86	70.51	70.65	71.9	68.43	70.27	72.7	71.59	70.33	73.09
TiO_2	0.48	0.50	0.48	0.42	0.79	0.5	0.46	0.47	0.45	0.38
Al_2O_3	11.19	10.87	11.15	10.45	12.87	10.7	11.46	11.7	16.07	10.43
FeO_t	5.48	5.73	5.45	5.86	5.18	5.91	6.41	6.52	3.28	6.04
MnO	0.30	0.31	0.30	0.32	0.23	0.34	0.34	0.33	0.07	0.28
MgO	0.20	0.20	0.20	0.09	0.79	0.42	0.21	0.43	0.88	0.1
CaO	0.30	0.30	0.30	0.31	1.08	0.84	0.67	1.14	1.04	0.5
Na_2O	6.38	6.40	6.37	5.25	5.71	5.78	2	1.63	1.74	1.75
K_2O	4.53	4.53	4.53	4.76	4.36	4.59	5.04	5.46	5.78	6.77
P_2O_5	< L.D.	< L.D.	< L.D.	< L.D.	< L.D.	< L.D.	< L.D.	< L.D.	< L.D.	< L.D.
Total	99.72	99.35	99.43	99.36	99.44	99.35	99.29	99.27	99.64	99.34
LOI	0.00	-0.05	0.08	2.51	0.79	1.60	9.04	9.08	9.50	7.03
Be	4.499	4.429	4.54	5.091	4.042	4.636	4.798	5.187	4.068	5.373
Sc	8.06	7.94	7.93	4.91	13.25	7.35	5.12	5.55	5.22	3.01
V	1.67	1.709	1.616	0.66	36.27	2.962	0.707	1.755	14.69	1.311
Cr	39.83	22.78	30.66	19.61	59.66	31.66	< L.D.	< L.D.	13.83	26.04
Co	0.225	0.225	0.127	0.073	4.624	0.313	0.04	0.317	2.303	0.166
Ni	< L.D.	< L.D.	< L.D.	< L.D.	< L.D.	< L.D.	< L.D.	< L.D.	< L.D.	< L.D.
Cu	< L.D.	< L.D.	9.905	< L.D.	6.245	< L.D.	< L.D.	< L.D.	< L.D.	< L.D.
Zn	193.2	208.9	199.4	222.3	180.3	212.5	221.4	222.9	79.04	235
Ga	31.17	32.37	32.24	32.03	30.54	32.06	32.21	32.23	25.26	29.75
Ge	2.523	2.614	2.652	2.671	2.414	2.556	2.518	2.649	1.55	2.538

As	2.295	2.017	2.011	2.23	1.306	1.8	1.971	2.457	2.013	2.299
Rb	103.7	106.5	108.2	122	90.87	106.1	256	198.6	123.9	178.5
Sr	2.306	2.189	2.411	3.723	56.11	13.05	52.83	30.25	117.9	22.04
Y	73.96	76.57	76.7	84.69	71.28	77.81	82.59	81.64	30.72	98.87
Zr	618.2	646.8	644.6	706.1	565	652.2	718.5	722.1	427.4	713.4
Nb	83.17	87.26	86.32	91.63	75.24	88.16	93.29	93.56	41.86	98.76
Mo	4.15	4.22	4.328	4.48	1.778	1.744	3.928	3.701	2.622	4.509
Cd	0.585	0.626	0.619	0.672	0.489	0.525	0.668	0.683	0.282	0.774
In	0.196	0.184	0.188	0.205	0.146	0.181	0.195	0.176	< L.D.	0.149
Sn	5.722	6.011	5.991	6.465	5.007	5.992	6.577	6.643	5.412	7.416
Sb	0.199	0.211	0.209	0.203	0.227	0.194	0.209	0.219	0.175	0.231
Cs	1.476	1.573	1.559	1.874	0.95	0.931	2.027	2.2	1.01	1.735
Ba	390.7	333.2	405.9	293.8	574.6	370.3	282.9	308.2	447	372
La	75.38	78.91	81.09	87.64	76.53	101.7	87.62	90.03	50.43	120.5
Hf	14.98	15.63	15.66	17.26	13.66	15.96	17.46	17.42	11.3	20.21
Ta	6.076	6.398	6.354	6.787	5.464	6.487	6.874	6.937	3.726	7.435
W	1.678	1.76	1.727	1.962	1.148	1.252	1.691	1.694	1.304	1.875
Pb	14.7386	15.3291	15.5061	17.1482	12.9708	14.2818	17.2367	17.6564	13.7325	19.8169
Bi	< L.D.	< L.D.	< L.D.	< L.D.	< L.D.	< L.D.	< L.D.	< L.D.	< L.D.	< L.D.
Ce	167.9	172.5	175.1	189.5	144.8	166.5	188.8	194.6	89.1	222.5
Pr	19.4	19.92	20.26	21.88	18.56	22.66	21.57	21.91	10.57	26.53
Nd	72.77	73.85	76	83.06	69.72	84.3	81.69	83.9	36.8	102
Sm	14.81	15.36	15.34	17.09	14.32	16.74	16.85	17.41	6.689	20.87
Eu	3.438	3.569	3.562	3.777	3.116	3.797	3.738	3.855	0.859	4.373
Gd	12.78	13.16	13.33	14.91	12.35	14.03	14.65	15.12	5.48	18.41
Tb	2.13	2.21	2.214	2.461	2.068	2.326	2.427	2.482	0.867	2.957
Dy	13.38	13.91	13.92	15.37	12.86	14.32	15.17	15.49	5.409	18.36
Ho	2.818	2.957	2.932	3.267	2.737	2.979	3.194	3.228	1.139	3.825
Er	7.621	7.93	7.869	8.667	7.359	8.081	8.509	8.617	3.145	10.06
Tm	1.101	1.17	1.163	1.275	1.081	1.188	1.244	1.275	0.499	1.459
Yb	7.441	7.913	7.857	8.612	7.314	8.12	8.521	8.781	3.502	9.861

Lu	1.144	1.215	1.192	1.317	1.111	1.232	1.284	1.326	0.54	1.465
Th	12.23	12.78	12.68	14.21	10.07	13.02	14.52	14.68	14.02	16.14
U	2.859	2.982	2.936	3.218	2.234	2.235	3.07	2.933	2.298	3.314

	NBS4.1-P1 Pumice	**NBS1.2-P1 Pumice**	**NBS4.1-B1 Basalt**	**NBS5.1-B2 Basalt**	**NBS2.1-S1 Scoria**	**NBS4.1-B2 Basalt**	**NBS2.1-B1 Basalt**	**NBS4.1-B3 Basalt**	**NBS5.1-B1 Basalt**	**NBS5.1-S1 Scoria**
E (m)	0536648	0531250	0532385	0537042	0531354	0534616	0531990	0533922	0536774	0535998
N (m)	0937896	0935278	0937956	0936480	0936564	0938536	0936542	0937938	0936069	0936159
SiO_2	68.93	73.01	45.43	47.3	47.58	49.37	48.13	49.29	46.62	47.93
TiO_2	0.28	0.44	2.19	2.29	2.01	1.90	1.97	1.93	2.20	1.69
Al_2O_3	7.75	10.86	16.81	15.84	15.44	15.79	15.84	17.26	14.89	14.68
FeO_t	8.04	6.06	11.46	10.98	10.61	10.53	10.63	11.26	11.04	9.93
MnO	0.35	0.33	0.19	0.19	0.18	0.18	0.18	0.18	0.18	0.17
MgO	0.22	0.12	8.81	7.81	8.81	7.08	7.9	5.79	9.02	9.77
CaO	3.98	0.4	10.52	10.73	10.52	9.65	10.22	9.84	11.17	11.48
Na_2O	5.04	1.87	2.52	2.66	2.67	3.00	2.75	3.11	2.65	2.3
K_2O	4.52	6.25	0.46	0.67	0.67	1.00	0.86	0.92	0.59	0.58
P_2O_5	< L.D.	< L.D.	0.33	0.35	0.36	0.34	0.35	0.29	0.42	0.38
Total	99.11	99.34	98.72	98.82	98.85	98.84	98.83	98.87	98.78	98.91
LOI	7.94	7.40	1.76	1.79	0.44	0.26	0.64	1.37	0.16	1.52
Be	7.068	4.866	1.121	1.051	0.985	1.126	0.963	1.082	0.779	0.886
Sc	< L.D.	4.77	34.86	32.87	32.89	29.51	32.95	30.33	34.48	33.57
V	2.439	1.356	216	283.9	263.2	238.6	263.1	266.8	284.1	233.6
Cr	16.75	35.46	368.6	391.8	392.2	263.2	392.6	157.7	581.3	573.8
Co	0.409	0.248	49.62	46.66	48.33	43.08	47.28	37.91	49.35	48.12
Ni	< L.D.	< L.D.	87.92	114.6	75.11	53.49	72.93	30.69	143.4	153.7
Cu	< L.D.	< L.D.	51.92	76.48	37.62	37.22	36.28	25.52	72.91	89.72
Zn	334.6	217.7	109.8	116.2	113	107.1	101.9	97.41	97.09	85.96

Ga	30.04	31.34	21	19.09	19.12	19.4	19.13	20.42	18.14	16.49
Ge	2.432	2.778	1.594	1.563	1.541	1.559	1.473	1.493	1.578	1.479
As	2.959	2.545	< L.D.	< L.D.	< L.D.	1.326	< L.D.	< L.D.	< L.D.	< L.D.
Rb	124.6	158.3	3.073	7.675	10.75	15.82	12.21	13.88	6.691	10.62
Sr	92.67	7.489	433.8	441.7	455.9	476.3	441.5	454.7	447	346.5
Y	136.3	87.5	23.21	19.59	20.86	23.15	21.29	21.78	21.76	16.98
Zr	882.5	702.3	133.6	115.3	124.1	137.7	124.7	127.1	107.6	93.79
Nb	160.5	89.42	23.72	17.79	21.97	20.11	21.95	20.64	18.45	14.41
Mo	6.446	4.352	< L.D.	0.635	1.209	1.31	1.176	1.109	0.799	0.944
Cd	1.029	0.733	0.1	0.167	0.188	0.193	0.209	0.183	0.142	0.122
In	0.154	0.172	0.097	< L.D.	0.088	0.086	0.093	0.087	0.085	0.092
Sn	9.441	6.449	1.667	1.732	1.394	1.815	1.407	1.516	1.351	1.254
Sb	0.272	0.237	< L.D.	< L.D.	< L.D.	< L.D.	< L.D.	< L.D.	< L.D.	< L.D.
Cs	1.189	1.778	< L.D.	0.023	0.097	0.129	< L.D.	< L.D.	< L.D.	0.018
Ba	510.8	284.9	254.1	257.8	250.6	458.6	323.4	268.9	267.1	189.2
La	131.2	90.11	21.27	15.69	19.11	21.17	19.78	18.35	17.52	12.2
Hf	24.23	16.92	3.506	3.02	3.315	3.642	3.312	3.436	2.822	2.5
Ta	11.09	6.669	1.809	1.351	1.666	1.539	1.667	1.601	1.42	1.104
W	2.182	1.79	< L.D.	< L.D.	< L.D.	< L.D.	< L.D.	< L.D.	< L.D.	< L.D.
Pb	17.337	17.0445	2.53	3.3679	2.5829	4.2856	2.7221	2.5731	2.1306	2.2527
Bi	< L.D.	< L.D.	< L.D.	< L.D.	< L.D.	< L.D.	< L.D.	< L.D.	< L.D.	< L.D.
Ce	245.4	185.3	43.67	34.42	41.31	42.95	41.63	38.98	36.59	27.42
Pr	28.2	21.6	5.746	4.536	5.278	5.668	5.475	5.142	5.008	3.665
Nd	108.2	82.06	23.92	19.36	22.18	23.36	22.66	21.24	21.35	15.88
Sm	22.87	16.63	5.329	4.443	4.877	5.177	4.972	4.703	4.866	3.708
Eu	5.663	3.729	1.855	1.559	1.703	1.84	1.716	1.653	1.767	1.314
Gd	21.26	14.69	4.901	4.229	4.5	4.808	4.575	4.382	4.678	3.537
Tb	3.553	2.402	0.746	0.635	0.678	0.717	0.684	0.677	0.693	0.537
Dy	22.84	15.09	4.49	3.802	4.071	4.331	4.113	4.087	4.142	3.285
Ho	4.926	3.212	0.908	0.771	0.822	0.876	0.827	0.832	0.833	0.664
Er	13.16	8.583	2.327	1.951	2.065	2.238	2.111	2.149	2.084	1.67

Tm	1.948	1.275	0.31	0.265	0.285	0.308	0.286	0.303	0.281	0.232
Yb	13.15	8.548	2.072	1.735	1.872	2.011	1.89	1.991	1.799	1.507
Lu	1.959	1.281	0.319	0.259	0.285	0.306	0.284	0.302	0.271	0.233
Th	16.69	13.96	2.231	1.651	2.134	2.576	2.187	2.391	1.572	1.355
U	4.163	3.194	0.211	0.328	0.514	0.674	0.377	0.4	0.291	0.383

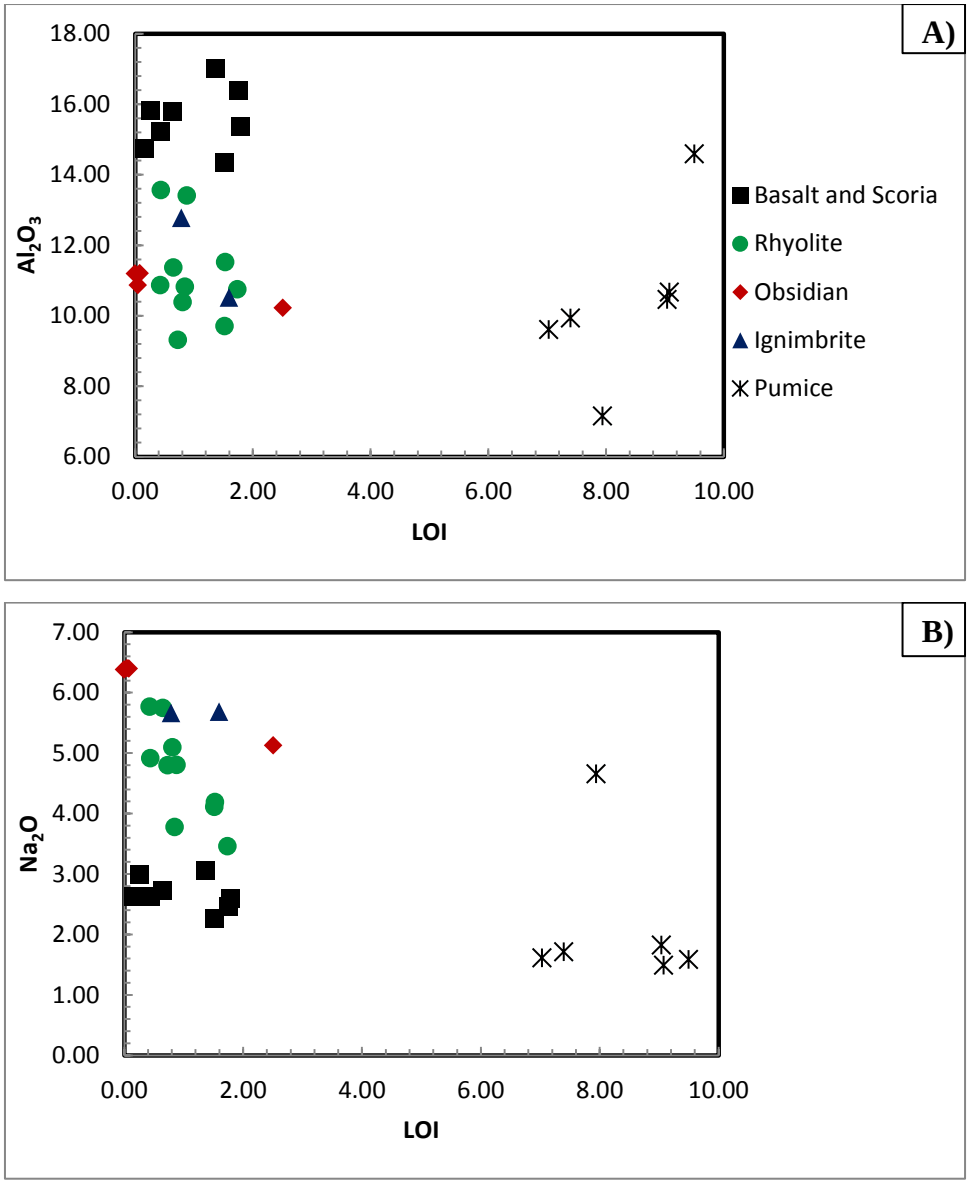

Figure 4.2: *Graphs of Al_2O_3 and Na_2O with LOI that show the variation of mobile and immobile major element.*

On the following section of this chapter the presentation and interpretation of the geochemical data are thoroughly discussed. At first major element then trace element and finally the petrogenesis of the silicic volcanic product is discussed.

4.2. Major Element Geochemistry

Major elements are elements which predominate in any rock analysis. They are Si, Ti, Al, Fe, Mn, Mg, Ca, Na, K and P. Their concentration is expressed in wt. % in oxide form. The main goal of using the major element geochemistry is to understand the magmatic

process. The concept behind this is the chemical composition plus mineralogical composition of the source regions and the rock forming process exerts a fundamental control over the magmatic rock. So the source and process of rock formation will be analyzed by examining the concentration of major elements at preliminary level. The analysis and interpretation is also checked by trace element data for further assurance.

The major element analytical data of the thirty samples collected from the study area is used in oxide, elemental and CIPW norm form. The raw analytical data readjusted to volatile free bases to use for the interpretation and to draw the graphs. The volatile free base is calculated by normalizing the major element concentration value to 100% by subtracting the volatile concentration (that is presented as LOI). ICP-OES give Fe concentration in form of Fe_2O_3. From the volatile free base FeO is calculated by multiplying Fe_2O_3 by 0.8998. Then FeO_t calculated by the mathematical formula; $FeO_t=FeO+Fe_2O_3$ (Rollinson, 1993).

The CIPW norm calculation is a method of working out the mineralogy of a rock from a chemical analysis. Because the mineralogy of the norm is entirely dependent on chemistry, fine or coarse grained, finally it gives a different mineralogical percentage distribution compare to the modal proportion result from the petrographic analysis. The element fractions from the oxides are also calculated to analyze mainly the evolution of the mafic volcanic products. The volatile free base geochemical data, element concentration or fraction and the CIPW norm calculation result is fully presented in Appendix III.

The analyzed samples show a typical bimodal composition on the Total Alkali Silica (TAS after Le Bas et al., 1986, see Fig.4.3) classification diagram. The distribution of the samples is mainly fall on felsic boundary with silica (SiO_2) above 68 wt. % and mafic with silica range of 45 to 50 wt. %. From the felsic samples only one sample fall on trachyte-trachydacite range and another one straddle on the boundary line between trachyte-trachydacite and rhyolite but the rest of the samples are rhyolitic in composition. All the mafic samples are basaltic in composition. From the diagram we can see the absence of rocks with silica range between 50 to 68.37 wt. %.

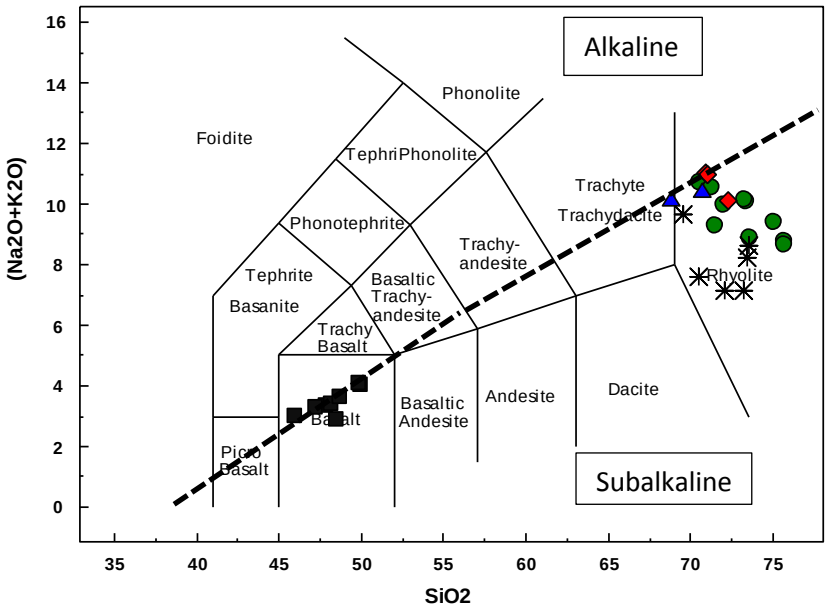

Figure 4.3: *TAS diagram after Le Bas et al. (1986) and overlay of alkaline-subalkaline basalt classification diagram after Irvine and Baragar (1971) of samples collected from BMC. The major element geochemistry data is volatile free base in wt. %.*

On the TAS diagram the broken line classify the basaltic rocks in to two; subalkaline and alkaline. The boundary line between the two types of basalt is after Irvine and Baragar (1971). The Boko samples fall on the transitional to weakly subalkaline basalt region.

Associating the petrographic description that is discussed on chapter three with CIPW norm of each mineral for the basalt give some additional information about the type of basalt. According to the minerals norm proportion the basalt that is classified under transitional to weakly subalkaline basalt on the above paragraph have proportions of olivine norm (14.05-24.05 wt. %) and some samples of slightly undersaturated with nepheline norm less than 2 wt. %. Based on the norm calculation the Boko basalts are olivine normative transitional to weakly subalkaline basalt.

The elemental ratio of major elements after Pearce (1970) gives a clear discrimination in the composition of the olivine normative transitional to subalkaline basalts. The basalts fall on different lineage on P/K against Ti/K diagram (Fig.4.4). The sample which has a high Ti/K against P/K and above 1 wt. % (1.73 and 1.98) nepheline norm is fully found on the southeastern and northwestern margin of the study area that exposed by major faults. These basalts are found in the same region to Bofa basalts on the diagram. The

other group of basalt that found in the same region to Boset basalt has low Ti/K and P/K. These basalts are located mainly on the caldera floor by associating with the scoria cones.

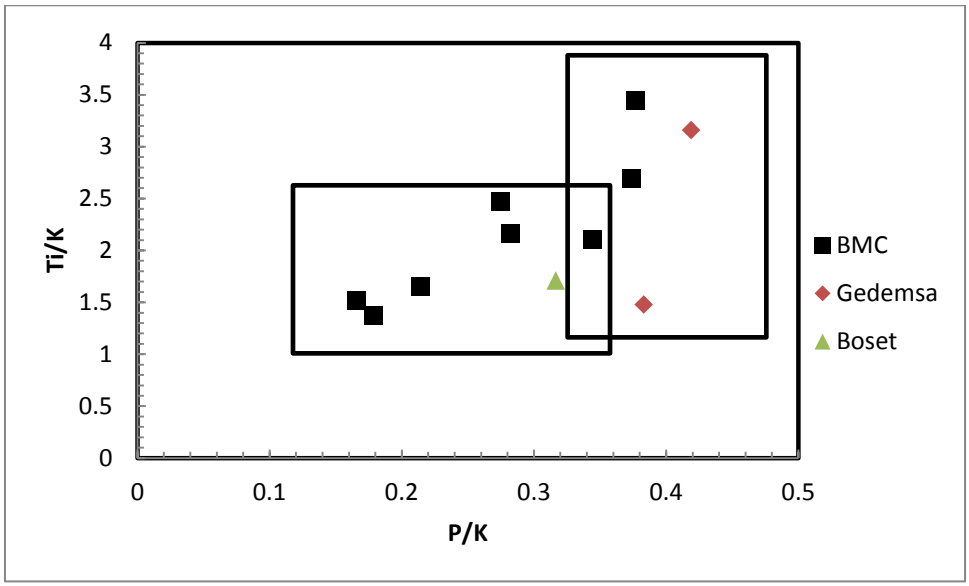

Figure 4.4: *Diagrams of Ti/K against P/K. The box indicates the classification of different basalt clusters comes from different chemistry according to Pearce (1970). The data of Boset and Bofa basalt is adopted from Tadiwos Chernet (1995) and Boccaletti et al. (1999) respectively.*

From LeBas et al. (1986) plot of agpaitic index against SiO_2 show the silicic volcanic products classified under peralkaline except one sample of pumice that fall under subalkaline felsic rock (see on Fig.4.5 (A)). Agpaitic index is calculated as:

$$\text{Agpaitic index} = \frac{Al_2O_3}{Na_2O+K_2O}$$

The calculation result show only one sample has agpaitic index value of 0.81 (subalkaline) but the rest have more than one and they classified as peralkaline. The silicic rocks are further classified by the diagram Al_2O_3 against FeO_t after Macdonald (1974). The diagram (Fig.4.5 (B)) shows; one sample of comenditic trachyte that is classified as subalkaline on the diagram of agpaitic index against SiO_2. The peralkaline reclassified in to three samples of comendite and the rest samples fall on the pantellerite region. The comenditic trachyte from BMC has low FeO_t relative to comenditic trachyte sample of Gedemsa volcano but their Al_2O_3 concentrations are more or less similar. Comendite and pantellerite that collected from Boko, Gedemsa and Boset has irregular variation in concentration of Al_2O_3 and FeO_t; that means they doesn't show any systematic variation trend.

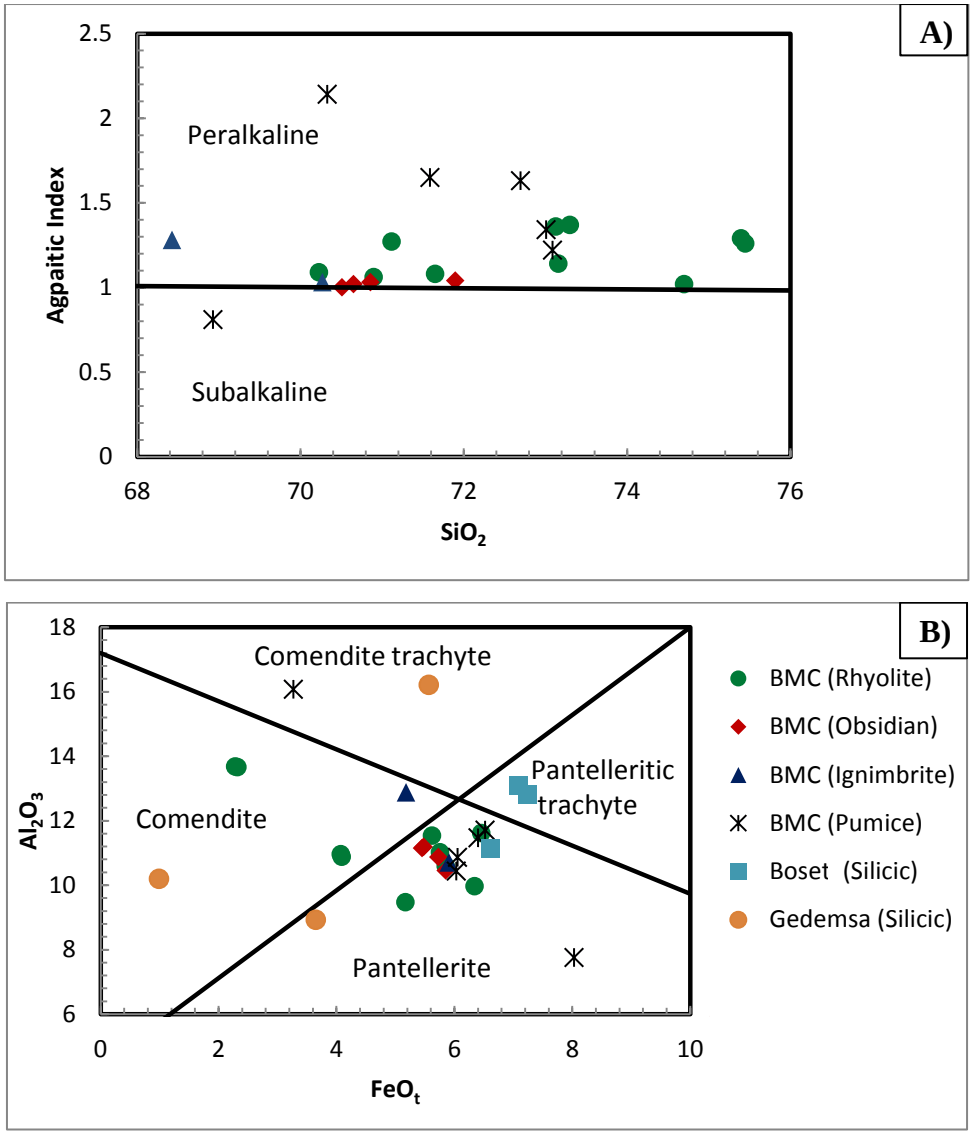

Figure 4.5: ***A)*** *Classification of silicic volcanic product from BMC, Gedemsa and Boset after Le Bas et al. (1986).* ***B)*** *The detail classification diagram for classifying peralkaline silicic rock into comenditic trachyte, comendite and pantellerite (after Macdonald, 1974). The geochemical data of Gedemsa volcano is adopted from Boccaletti et al. (1999) and Boset volcano from Tadiwos Chernet (1995). The concentration value of the major element is in volatile free base.*

From major element variation diagram different trends can be observed. The plot is prepared for some selected major elements on each mafic and silicic sample to refine the variation that is shown on the general major element variation diagram of both types of rocks. Different symbols are used to represent different rock types. On the general Harker variation plot (Fig.4.6) for the analysis of two rock types show a clear negative correlation observed on TiO_2, Al_2O_3, FeO_t, MgO, CaO, and P_2O_5 against SiO_2. But in case of Na_2O and K_2O against SiO_2 plots show positive correlation.

In addition to the general major element variation diagram a refining comparison diagram within the mafic and silicic rocks is plotted and presented (Fig.4.7). The comparisons between plots of mafic and silicic rocks for some major elements show variation on slope and trend. The major elements on the Harker diagram, presented on Fig.4.7, are selected based on the extremity difference on their manner of correlation distribution on each specific plot. On the different plots there is variation on slope and a random change in correlation trend. For instance, CaO against SiO_2 show difference in slope from steep in mafic rocks and become gentler in silicic rocks. The concentration of CaO on the mafic rocks show increment on the initial stage up to 46.5 wt. % of SiO_2 then start to show negative correlation. This kind of bimodal trend is also observed in P_2O_5 variation diagrams. The other plot which show slope change between the two rock types is FeO_t that is steep negative correlation on mafic and gentler on silicic. In the silicic rocks the sample distribution in all selected major element plot against SiO_2 is highly dispersed. The full trend change is observed in Na_2O plot which shows positive in mafic rock and negative in silicic rocks. In silicic rocks the slope is gentler. In case of K_2O the two plots show positive in mafic and become constant variation in silicic rocks.

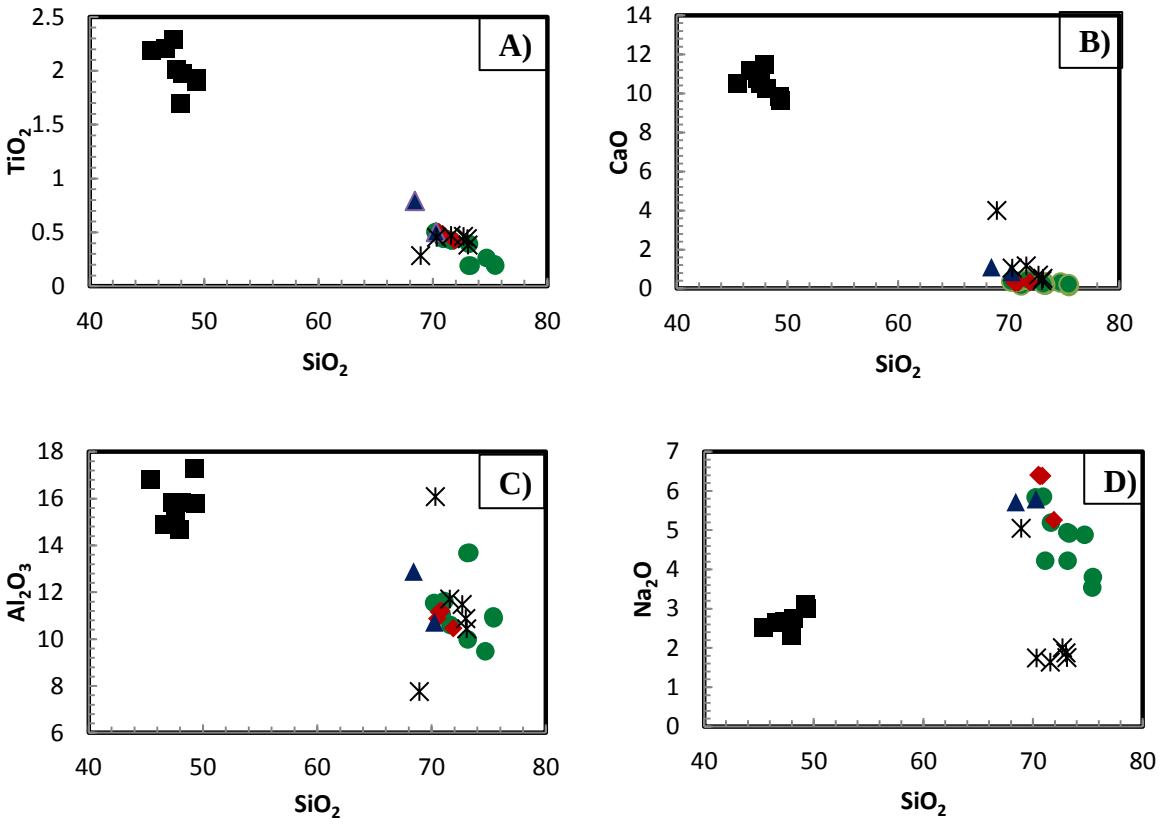

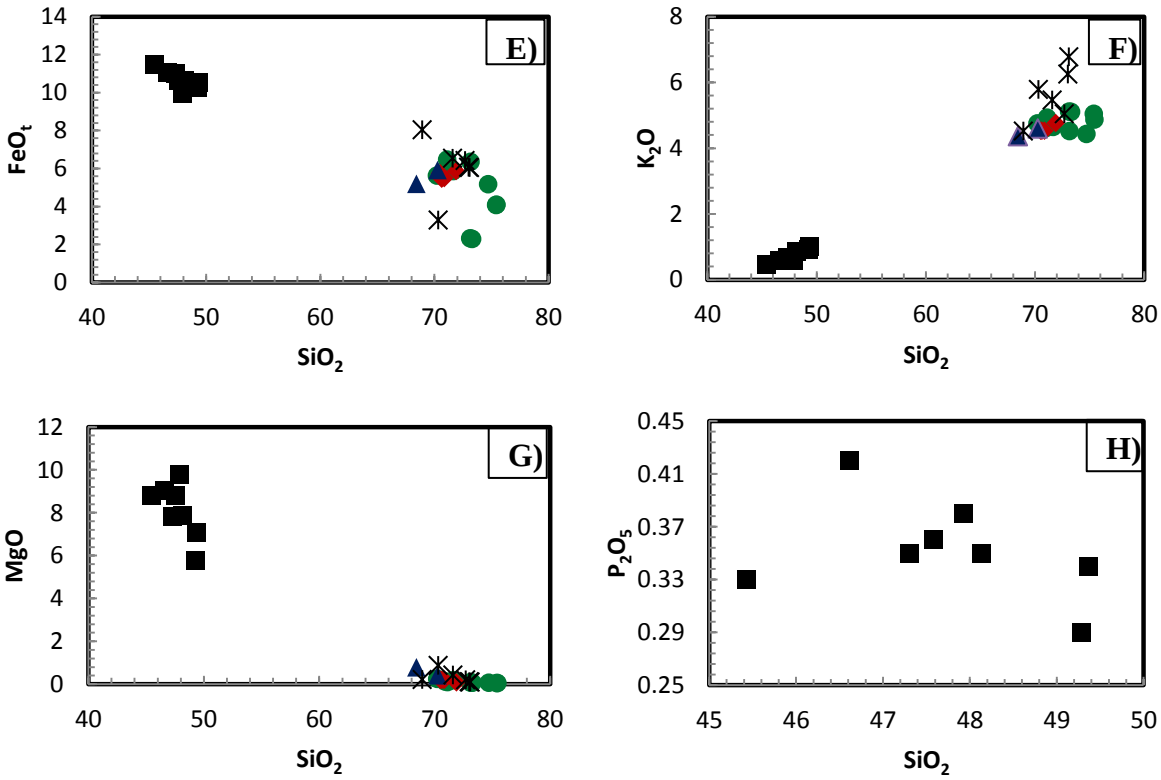

Figure 4.6: *Harker diagram of whole rock composition for all representative rock samples collected in BMC. The major element concentration is volatile free base and expressed by wt. %.*

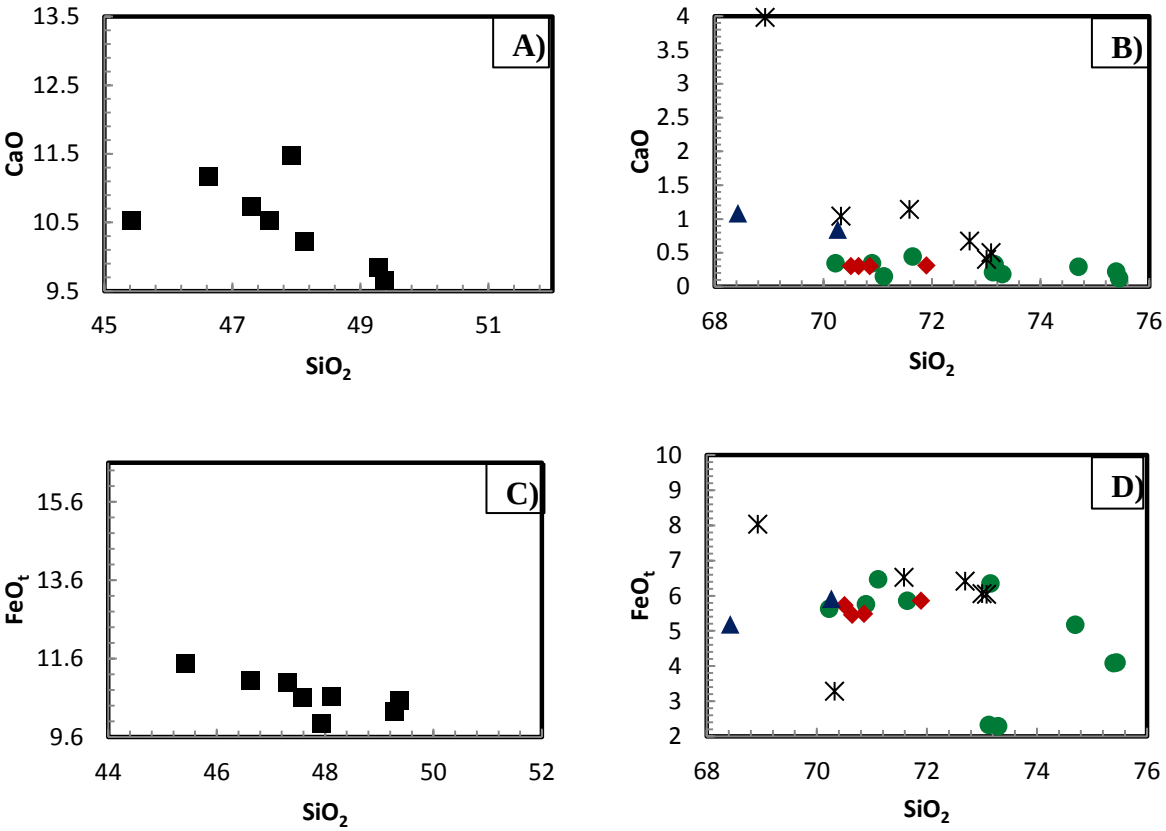

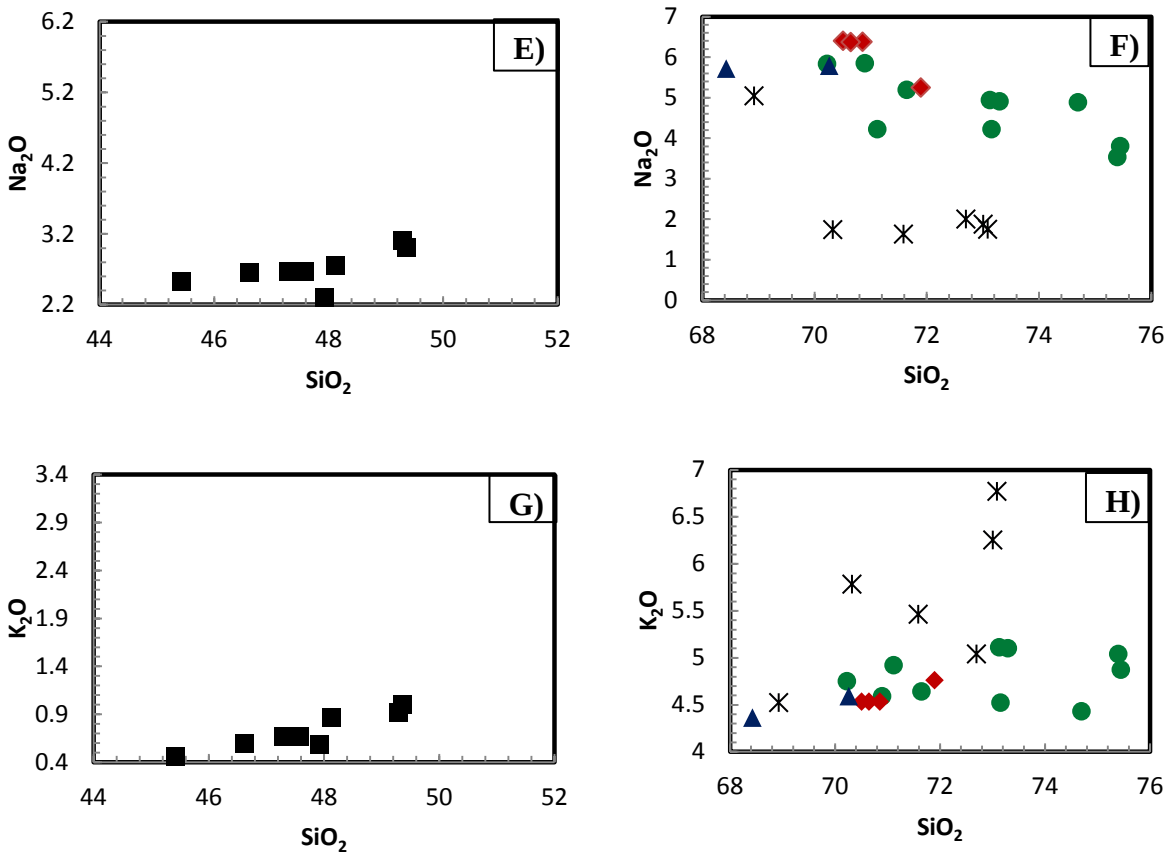

Figure 4.7: *Major element variation diagram for a purpose to compare the correlation trend for mafic and silicic volcanic products of BMC. The concentration value of the major elements is volatile free base and expressed in wt. %. In CaO against SiO_2 diagram for silicic rock, the sample which show anomalously high CaO is hydrous (LOI>5 wt. %).*

The overall trend of major element variation diagrams has characteristics to show the evolving process for the rocks is fractional crystallization. The distribution of the samples and the slopes of the trend in the diagrams suggest early crystallization controlled by olivine followed by pyroxene, plagioclase, Fe-Ti oxides and apatite. A steep slope break in the variation diagram of SiO_2 against MgO clearly indicates the control of olivine fractionation from the system in the initial level and then dominated by pyroxene, plagioclase, Fe-Ti oxides and apatite (after 46 to 47 wt. % of SiO_2). Variation of TiO_2 and P_2O_5 with SiO_2 show the crystal-liquid equilibration with Fe-Ti oxides and apatite was reached after considerable fractionation at high SiO_2.The variation of the major elements for the silicic analyzed rocks against SiO_2; different fractionation histories may be responsible for the trend. The variation of SiO_2 (specifically above a value of 65 wt. %) against K_2O and Na_2O shows a vertical variation from the trachydacite-trachyte to

pantelleritic rhyolite samples. In this group of rock it appears to be the major element variation is controlled by the fractionation of alkaline feldspar in the final stage of the magma evolution. In the comparison plots of selected major elements we can roughly suspect the relative dominancy of different mineral phases on different stage of the magma evolution. For instance CaO and FeO_t against SiO_2 clearly show a trend change from steep negative to gentler slope. The trend change is an indication of CaO and FeO_t bearing mineral removal is less dominant in silicic magma relative to mafic. The overall elemental variation in the silicic suit shows two important fractionation trends. A first one dominated by fractionation of mafic phases (olivine, pyroxene, plagioclase feldspar, apatite and Fe-Ti oxides) and a second dominated by a fractionation of alkali feldspar.

4.3. Trace Element Geochemistry

Trace elements, by definition, constitute only a small fraction of a system of interest; they provide geochemical and geological information out of proportion to their abundance. According to Rollinson (1993) trace elements are elements which present at less than 0.1 wt. % level and their concentrations are expressed in parts per million (ppm) or more rarely by parts per billion (ppb). It can also be defined as elements that are not stoichiometric constituents of phases in the system of interest (White, 2013). In the current study the system of interest is magmatic system. The presentation, interpretation of trace element data is given in this section of the chapter with the same grouping and symbols of main volcanic products, mafic and silicic rocks, used on the major element data presentation.

The plot in Fig.4.8 shows the variation between trace element and SiO_2. The compatible trace elements form a negative correlation. Especially Cu and Ni show a general negative trending best fit line with a concentration below the detection limit for silicic rocks. The others, V and Cr, still show a negative correlation but the silicic rocks have a concentration of above the detection limit of the analyzing instrument. The incompatible trace elements (Nb, Zn, Rb, Y and Zr) against SiO_2 are plotted. The plots show a clear positive trend line; the rhyolite exhibit high value. The trends of Ba, Sr and Sc show a bit difference relative to the above incompatible trace elements. Ba against SiO_2 variation plot shows more a gentler slope but Sr and Sc show negative correlation that reach very low values only on the rhyolitic rock. The Ba versus SiO_2 plot shows a steep variation

trend within the mafic and silicic rocks. The negative and positive trends of the compatible and incompatible elements show the differentiation and fractionation of Mg and Fe bearing minerals; like olivine and pyroxenes. The Mg and Fe are the accommodating elements for the compatible trace elements specially Ni and Cu. The trend of Sr and Ba indicates the differentiation process and removal of feldspar.

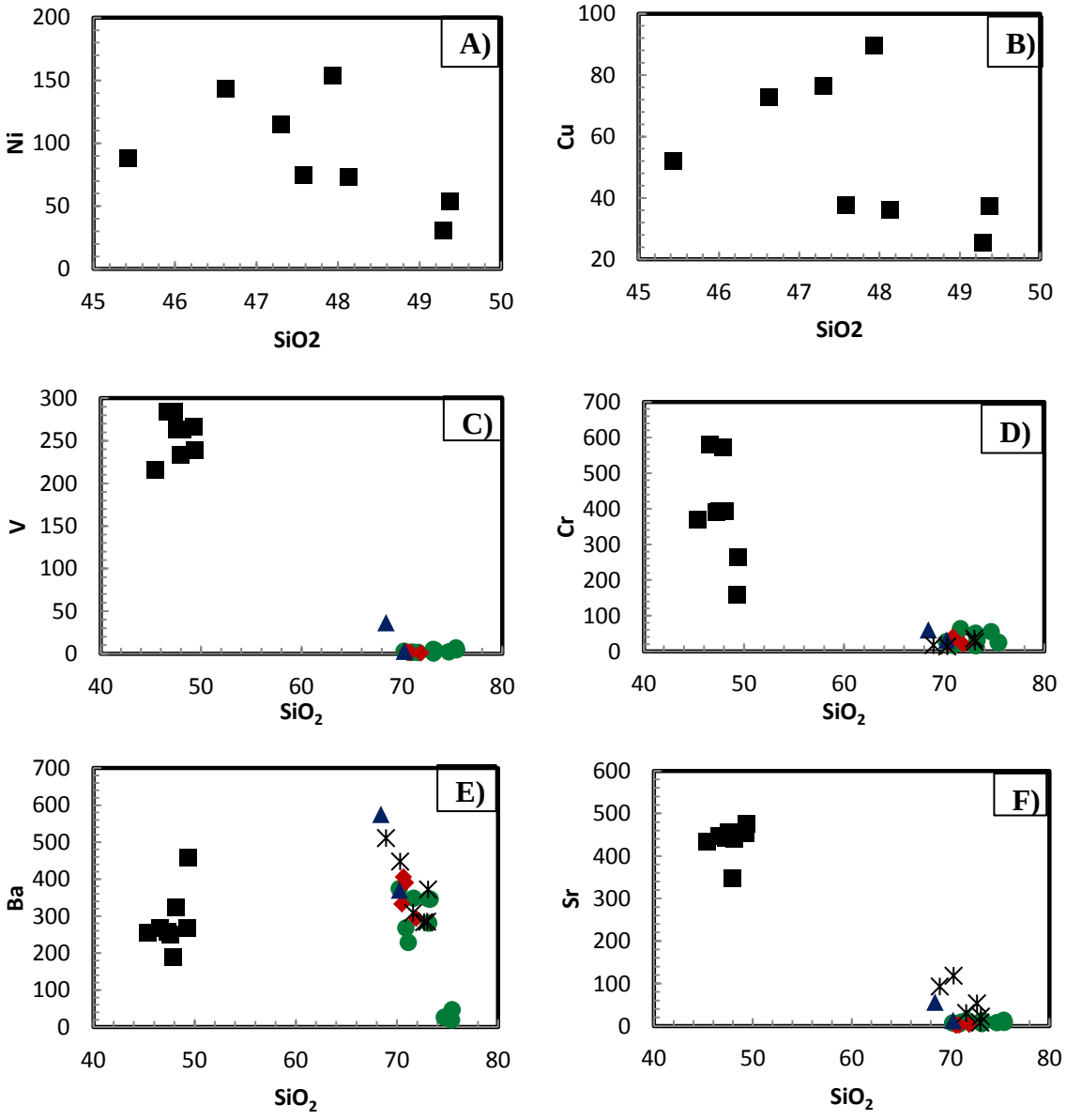

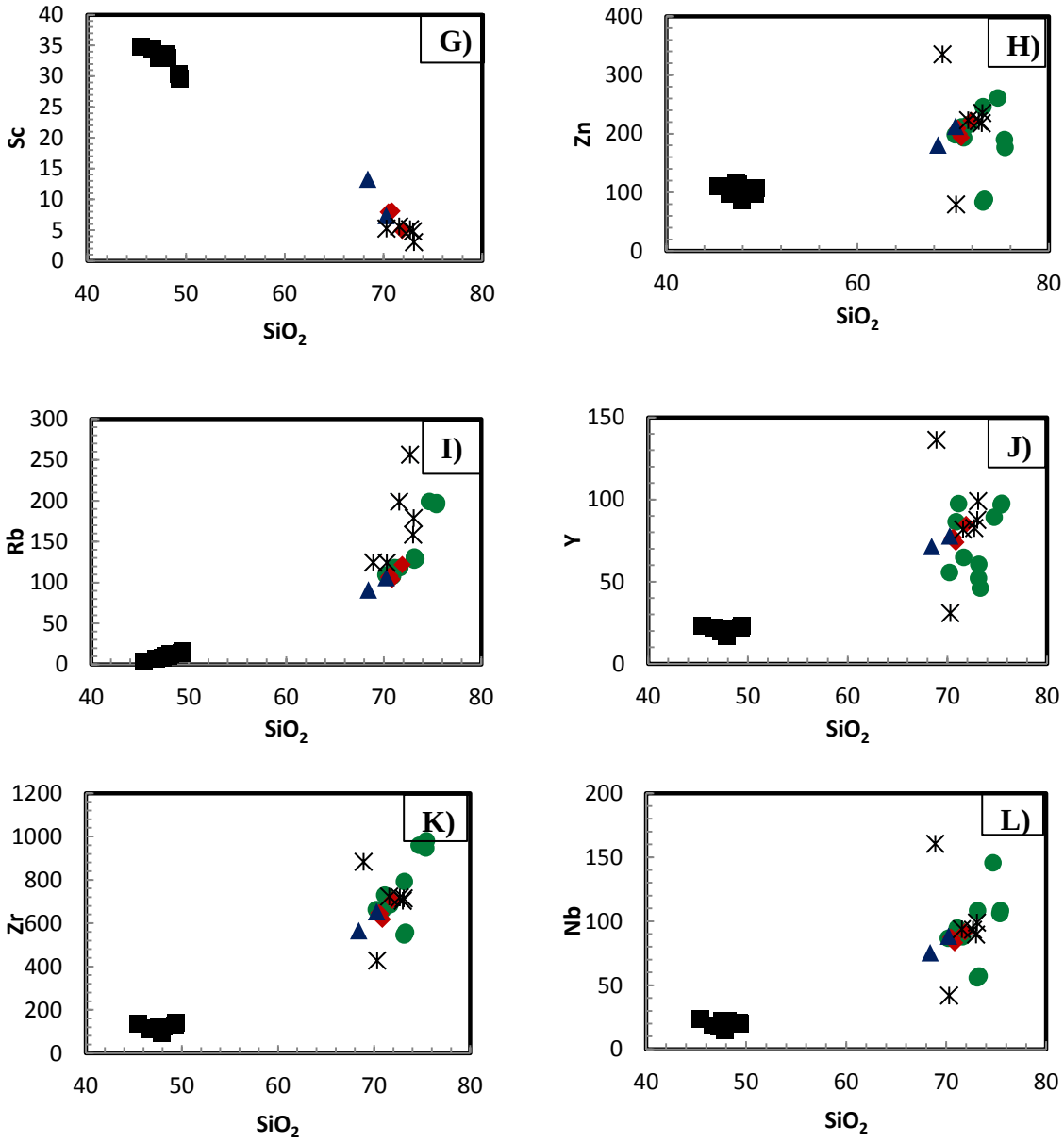

Figure 4.8: *Variation diagram of trace element against SiO_2.*

On account of the ionic size of Zr, Zr does not enter into the major crystalline phase. Because of this, Zr prefers the liquid phase so it's very important to study behavior of elements in magmatic evolution by taking Zr as an index. The incompatible trace element (Zn, Y, Nb and Rb) against Zr show a positive correlation (see Fig.4.9). This show the silicic rocks have a similar evolution history. The noticeable dispersion is the sign of more than a single process is accountable for the evolution. There is a very small compositional gap between mafic and silicic volcanic product in the incompatible element against Zr plot relative to major element against SiO_2 plot.

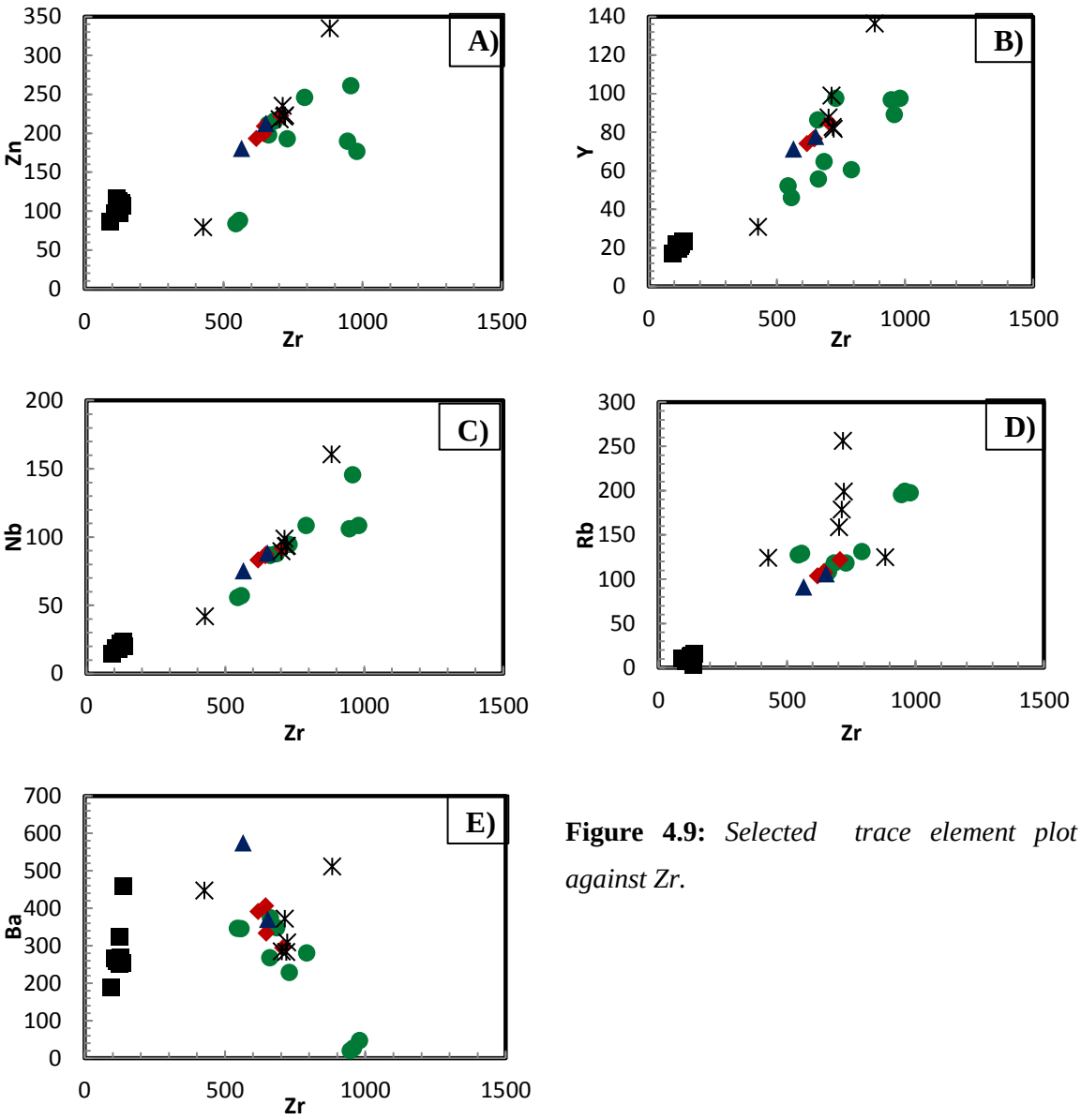

Figure 4.9: *Selected trace element plot against Zr.*

Plots for selected trace element-trace element ratio (Fig.4.10) give information about the evolution of the mafic and silicic magma that is discussed and elaborated further on section 4.4. For samples of silicic volcanic product; Rb/Sr against SiO_2 is plotted and show a positive trend. This indicates the fractionation of plagioclase (Sr can substitute Ca in the crystal lattice) is high relative to alkali feldspar (accommodate K). Ba/Y against Zr negative trend further evaluated the crystallization of alkali feldspar. The sharp drop in Ti/Zr in the less differentiated lava indicates significant removal of Fe-Ti oxides and/or pyroxenes in the initial stage of differentiation of silicic lava.

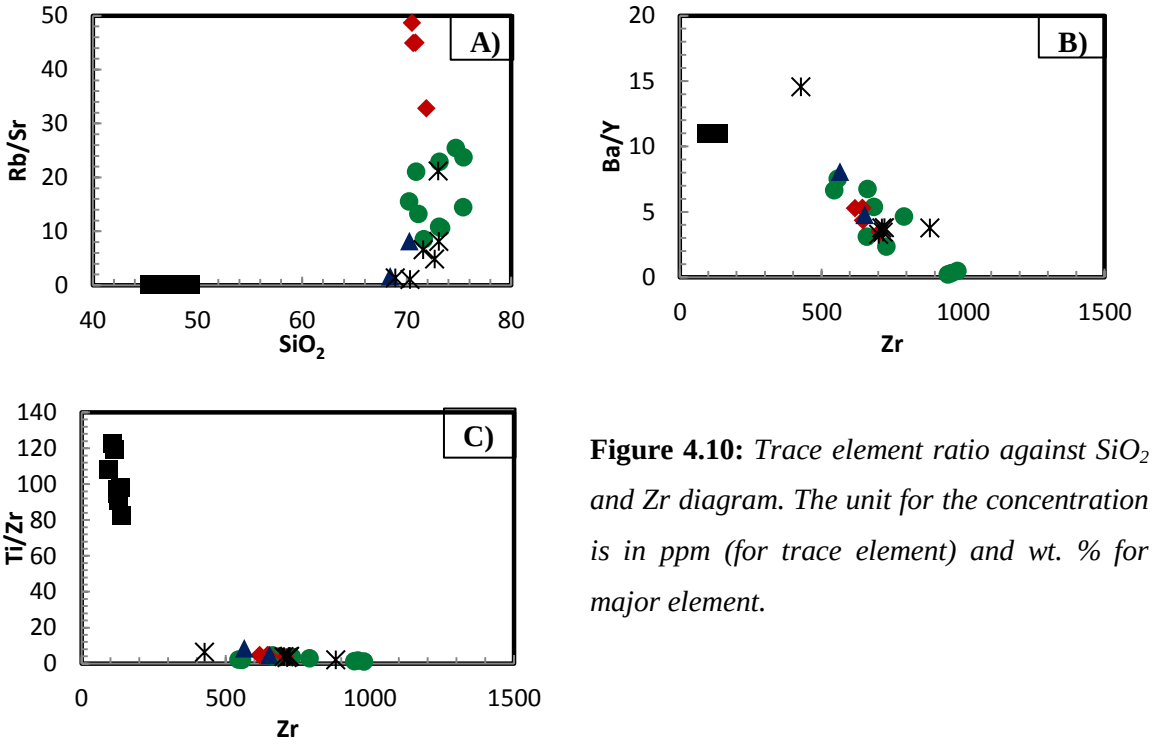

Figure 4.10: *Trace element ratio against SiO_2 and Zr diagram. The unit for the concentration is in ppm (for trace element) and wt. % for major element.*

Rare Earth Element (REE) analysis is made for the mafic and silicic volcanic products separately (Fig.4.11). The analysis shows abundance of Light REE (LREE) relative to chondrite in the two groups of volcanic product. The REE value of concentration is normalized to chondrite according to values of Boynton (1984). The enrichment of the LREE in mafic rock range, in terms of $(La/Yb)_N$, between 4.9-6.4. The gentle slope in HREE show the source for mafic rock is garnet free. The pattern of the REE diagram show parallel for all of the samples but one sample shows a slight departure from the general pattern of the samples. This indicates their derivation from similar source. The parallelity of the relative enrichment shows a systematic accumulation or removal of mineral phases. The Eu concentration of mafic lavas shows a slight positive anomaly (Eu/Eu*~1.1) that likely comes from accumulation of plagioclase feldspar. For the silicic volcanic products the REE analyses are made for selected samples of rhyolite, ignimbrite, obsidian and pumice to decrease the complexity. The REE diagram pattern of the silicic rock shows enrichment in the LREE and gentle HREE. The enrichment of LREE range between, in terms of $(La/Yb)_N$, 4.1-8.7. Similar to mafic samples the silicic samples show parallel pattern in the REE diagram. On all samples there is a negative anomaly on Eu (Eu/Eu*<1). This is a typical indication for the fractionation of plagioclase feldspar. The strong negative anomaly of Eu is observed in rhyolite samples (Eu/Eu*=0.3). On rhyolite

samples we can observe three ways of trend (negative, positive and flat) on the Ce concentration due to alteration. The flat trend is also shown by samples of ignimbrite, obsidian and pumice.

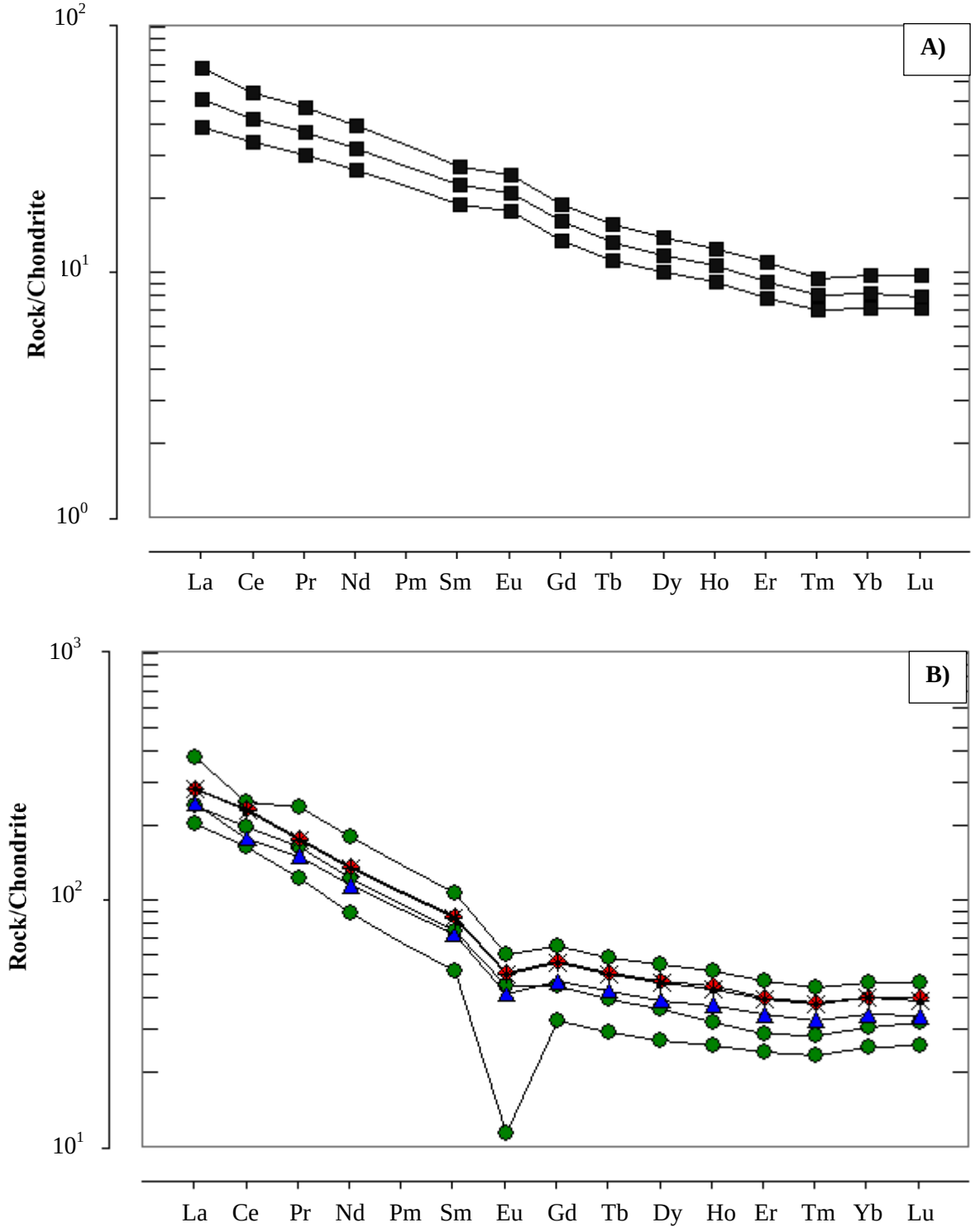

Figure 4.11: *REE variation diagram of representative samples from mafic (**A**) and silicic (**B**) rocks. The concentration value of the rock sample is normalized to chondrite value determined by Boynton (1984).*

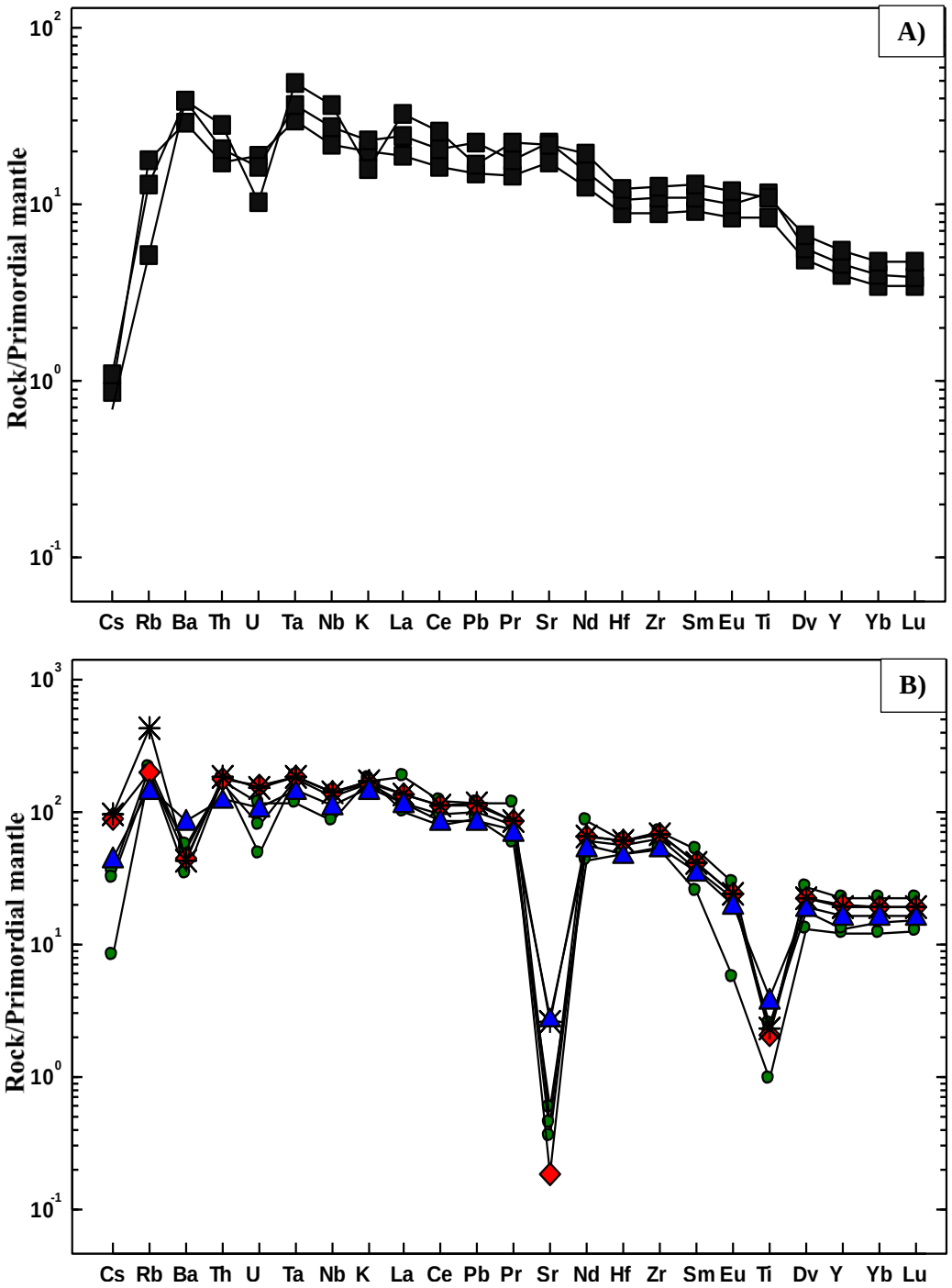

Figure 4.12: *Multi-element variation diagram of representative mafic (**A**) and silicic (**B**) rocks of BMC. The samples are normalized to primordial mantle of value determined by McDonough and Sun (1995).*

The multi-element variation diagram is ploted on Fig.4.12 to further understand the evolution of the BMC. The diagram is prepared based on McDonough and Sun (1995); normalized to primordial mantle plot. The diagram for the mafic material exhibit bell-shaped pattern. The diagram show a positive anomaly at Ba and negative anomaly in K

relative to Nb and Ta. The combination of minor enrichment in Ba and have no troughs at Nb and Ta indicates crustal contamination of the mafic lava during the fractionation process. Over all enrichement in the incompatible elements show fractionation of phases specially plagioclase feldspar. The spidergram for the silicic volcanic products show a trough in Ba, Sr and Ti. The negative anomaly on Ba and Sr show the removal of alkali and plagioclase feldspar from the magma. The troughs on Ti indicate the removal of accessory ilmenite.

4.4. Petrogenesis of Boko Silicic Rocks

Like other peralkaline volcanic centres, the main problem of Boko volcano include explaining the origin of peralkaline silicic rocks, their relationship with basaltic magmas, and the reasons for the paucity of intermediate compositions in the volcanic sequence. This kind of bimodal composition is common in other peralkaline volcanoes of the MER (Peccerillo et al., 2007). The data presented in this study reveal in agreement with previous studies; the Quaternary volcanism in the MER is dominated by a bimodal association of mafic and silicic products, with rare/no intermediate rocks.

To check whether the mafic and silicic rocks are genetically related, the major and trace element geochemistry is very important. The major and trace element against SiO_2 plots, show two clusters of samples distribution with some dispersion of the concentration on each clusters. The two clusters or groups are separated with a wide gap of concentration called daily gap (Peccerillo et al., 2003). The presence of the gap between the two rock types does not preclude the genetic association of the rocks. The diagrams of Nb-Zr, Hf-Th and Ta-Zr (Fig.4.13) form a positive correlation by forming a linear slope of approximately 1 that show the genetic relationship or co-genetic nature of the mafic and silicic rocks. Spidergram and multi-element variation diagram of mafic and silicic rocks selected samples show a parallel pattern with anomalies on different elements.

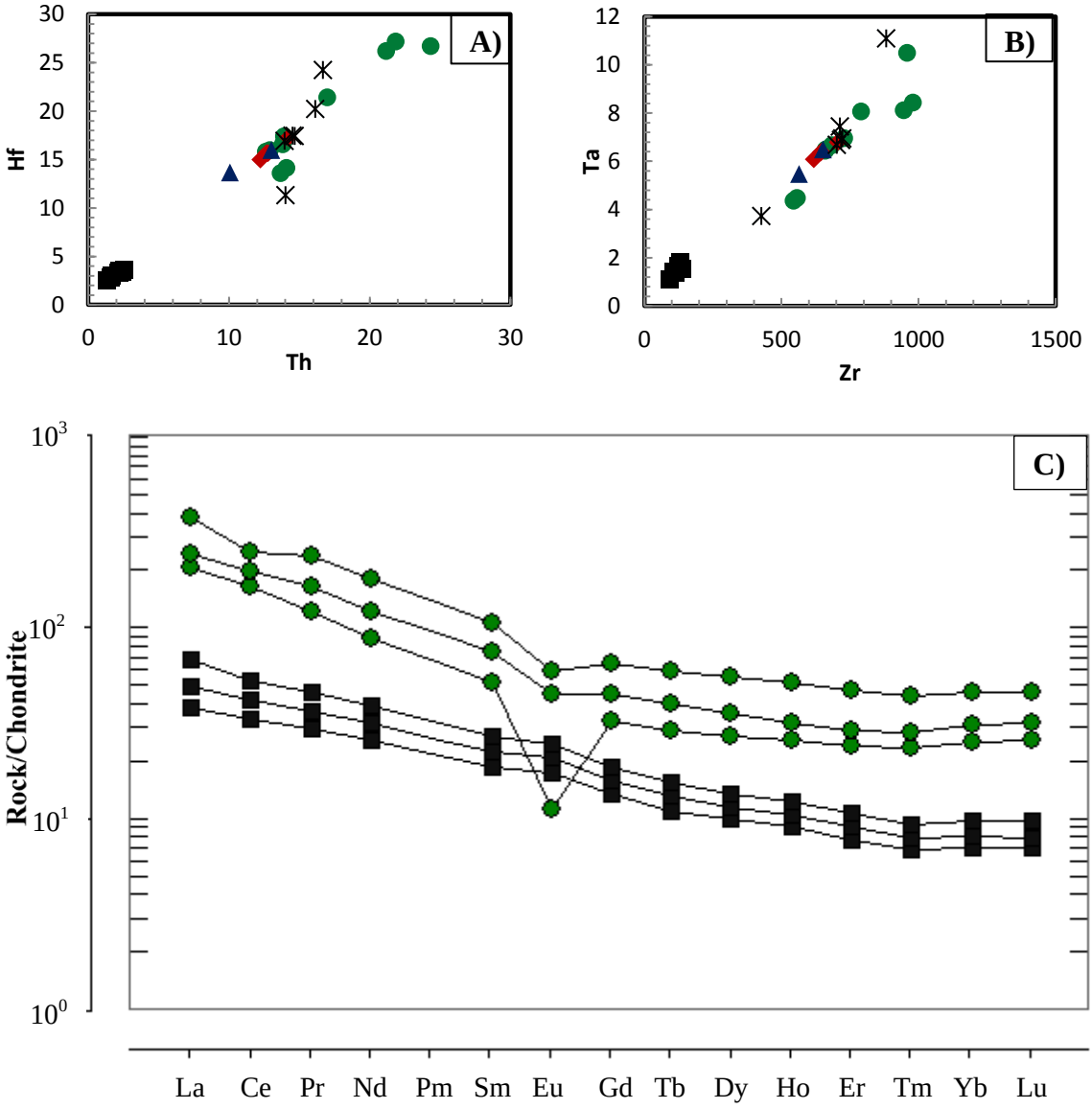
A)
Hf
Th
B)
Ta
Zr
C)
Rock/Chondrite
La
Ce
Pr
Nd
Pm
Sm
Eu
Gd
Tb
Dy
Ho
Er
Tm
Yb
Lu

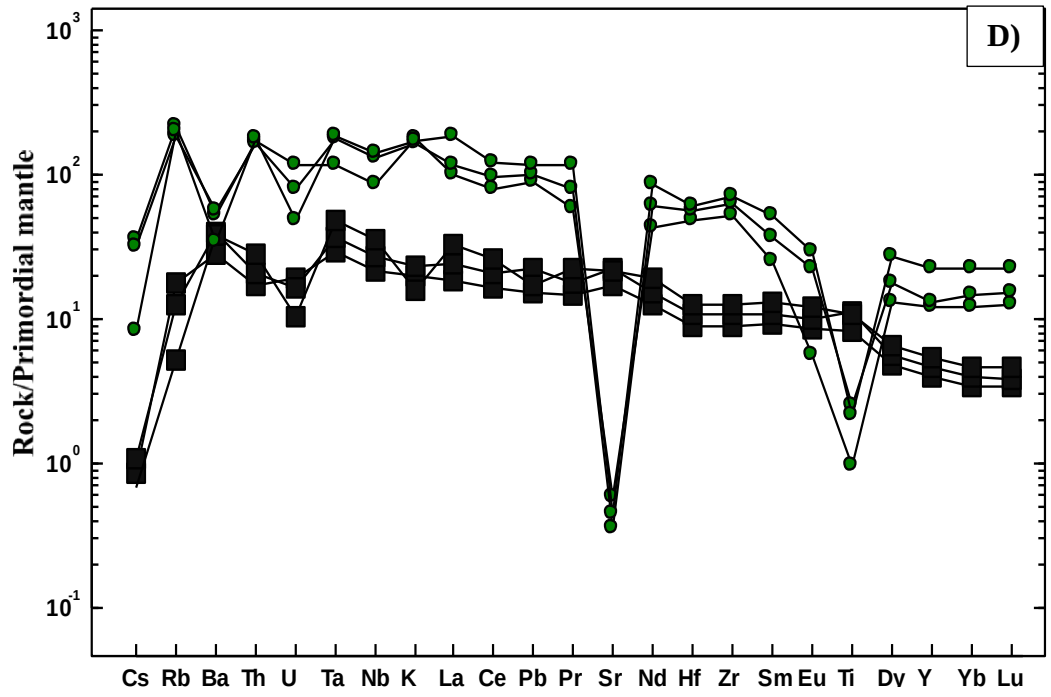

Figure 4.13: *Plots of incompatible trace element against Zr or Th (**A** & **B**), spidergram (**C**) and multi-element variation diagram (**D**).*

Different hypothesis are proposed to explain genesis of peralkaline volcanism (Trua et al., 1999; Peccerillo et al., 2007). The first one is melting of the old continental crust (crustal anatexis) and under plated basalt, second is a two-step process (partial melting followed by fractional crystallization) and third is fractional crystallization with involvement of crustal material. According to Peccerillo et al. (2003) the crustal anatexis alone does not explain the petrogenesis of the peralkaline volcanic product. To asses or evaluate the idea of Peccerillo et al. (2003) geochemistry of Ethiopian Precambrian rock that constitute the basement is compared with analysis result of BMC samples. By the effect of melting process (i.e. partial melting), ratios of incompatible elements (e.g. Rb/Nb and Rb/Zr) become higher in composition in the melt (BMC in this case) relative to the source (Precambrian rock). But this is not true when we compare the incompatible element ratio of BMC to the Precambrian rocks (see on Table 4.1). From the comparison of BMC geochemistry; we can understand crustal anatexis is unlikely process for the formation of peralkaline rocks of Boko. With a similar argument the incompatible element ratio is very low when it compare to the flood basalt. That indicates the partial melting of the Ethiopian flood basalt doesn't explain the petrogenesis of Boko volcanic products.

Table 4.2: *Rb/Nb and Rb/Zr value comparison of BMC samples to Precambrian rock and flood basalt of Ethiopia. The geochemistry data of Northern Ethiopia Precambrian rock is adopted from Mulugeta Alene et al. (2000), Southern and Eastern Precambrian metamorphic rock from Mengist Teklay et al. (1998) and Konso pluton is from Asfawossen Asrat and Barbey (2003). The flood basalt data is adopted from Kieffer et al. (2004).*

	BMC	Flood Basalt	Northern Ethiopia			Southern and Eastern Ethiopia	
			Basic/Intermediate	Acidic	Pluton	Metamorphic rock	Konso Pluton
Rb/Nb	0.13-1.37	0.13-2.16	1-6.33	0-5.56	0.6-12.6	0.2-10.07	1.12-5.81
Rb/Zr	0.023-0.21	0.0072-0.32	0.048-0.5	0-0.37	0.27-1.8	0.015-0.59	0.085-0.65

Based on the trace and major element analysis that discussed on the above two sections (section 4.2 and 4.3) we can understand the petrogenetic model for the formation and evolution of silicic products of BMC. The trace and major element data show a clear fractional crystallization trend that is dominated by removal of different mineral phases at different stage of the fractionation.

The mafic volcanic products strictly show a major and trace element variation that mainly affected by fractionation of mineral phases. From the sharp, steep negative correlation of FeO_t and MgO with SiO_2; the first phase of crystallizing minerals are Fe and Mg bearing mineral phases (eg, Olivine and Pyroxenes). The other phase that fractionate from the system is plagioclase feldspar that evidently indicated by the late dropping of CaO and Al_2O_3 trend line after some concentration of SiO_2. The fractionation of the plagioclase feldspar continues till and after the formation of silicic magma (Fig.4.7 (A)). After fractionation of olivine and pyroxene there is also a minor show of ilmenite and apatite fractionation from the system. Lastly the magma evolution is affected by alkali feldspar fractionation is that implied from the negative correlating trend line of K_2O and gentle Na_2O. In addition to this the dominancy of alkali feldspar phenocryst in highly evolved rhyolite thin section samples also show the late fractionation of alkali feldspar. The fractionation process is also shown by the trace element geochemistry with plots of trace

element ratio against trace element (e.g. Ba/Y against Zr) and major element diagrams that discussed in section 4.3. The plots of the compatible trace element (e.g. V, Cr, Ni and Cu) against SiO_2 and Zr show a negative correlating line, incompatible trace element (e.g. Nb, Zn, Rb, Y and Zn) show a positive trend lines that favors fractionation process. The REE diagram show negative Eu anomaly that support the fractionation of plagioclase feldspar. On multi-element variation diagram the trough on Ba, Sr and Ti also evidenced the fractionation of mineral phases specially alkali feldspar, plagioclase feldspar and accessory ilmenite.

It is well known that both batch and fractional partial melting processes are able to generate liquids with variable enrichments in incompatible elements, but with moderate depletion in compatible elements. In contrast, fractional crystallization is much more efficient in producing compatible element depletion than incompatible element enrichment. Therefore, models of incompatible against compatible trace elements are potentially powerful tools to further discriminate between fractional crystallization and melting processes. Sr against Rb is plotted for this purpose (Fig.4.14 (A)). The plots show a clear process of fractional crystallization with high concentration variation of compatible element (Sr) and low concentration variation of incompatible element (Rb). This is the result of compatible element respond in opposite manner for fractionation/partial melting process relative to incompatible element. The variation in concentration of both Rb and Sr fits the trend of crystallization process on log scale (Fig.4.14). From this the evolution of BMC silicic magma is modeled. For the modeling the parent magma is selected from the Boko samples, sample NBS4,1-B1, which show least differentiation relative to the other samples. The sample has MgO concentration 8 wt. % and Ni-88 ppm. The partition coefficient taken for the model is 4.7-Sr and 0.029-Rb (after Ewart and Griffin, 1994) that best fit the trending line on the plot. For the genesis of peralkaline rock of BMC the mafic magma need at least a degree of fractional crystallization 80%.

According to Peccerillo et al. (2003) in order to get peralkaline rhyolitic rock from fractionation of basaltic material the environment has to be at low pressure ~50 MPa. The result from MELT software at low pressure indicates the first phase that crystallized from the primitive basaltic melt is olivine and clinopyroxene at 1150 ^{o}C (see Fig.4.14 (C)).

Then follow by feldspar, and finally orthopyroxene at 900 ^{o}C. Because the excel interface for MELT software doesn't consider fractionation of crystal phases and crustal assimilation, it is not good to tell the mineral phases percentage. To know the fractionating mineral percentage, mass balance method is applied. The chemical composition of each mineral phase is adopted from Boccaletti et al. (1999) that analyzed from samples collected around the study area. To get less differentiated rhyolitic material of Boko (i.e. sample NBS2,2-O2) the primitive basalt fractionate the following minerals; 20.96% olivine, 14.19% clinopyroxene, 56.07% plagioclase feldspar and 8.26% Fe-Ti oxides. The highly differentiated peralkaline rhyolite rock (i.e. NBS4,1-R1) is derived from the less differentiated one by ~100% alkali feldspar fractionation.

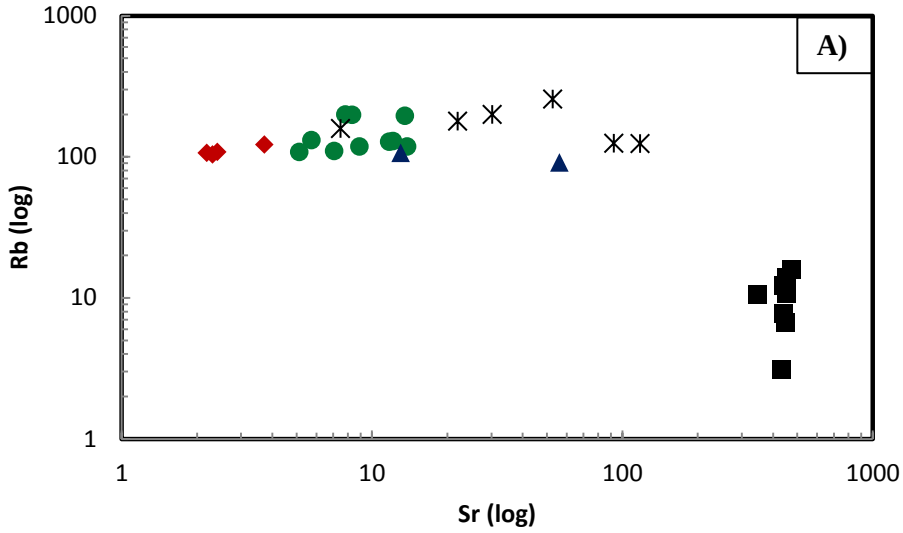

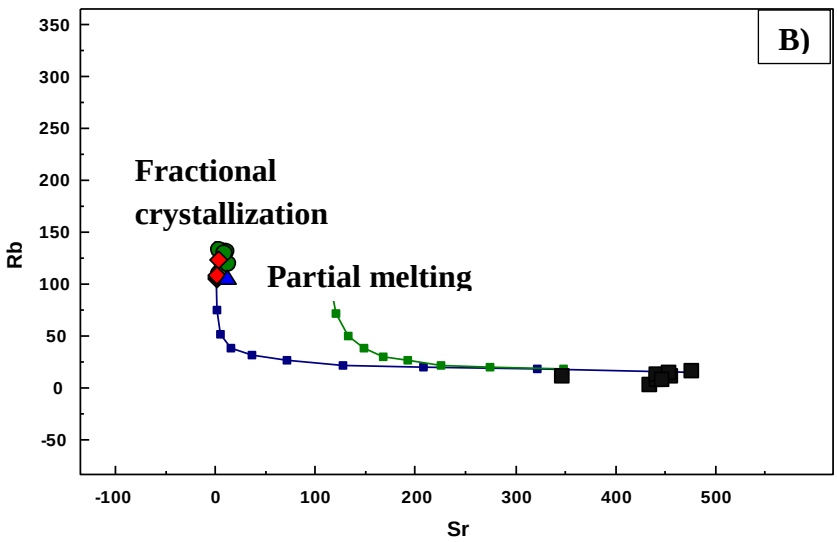

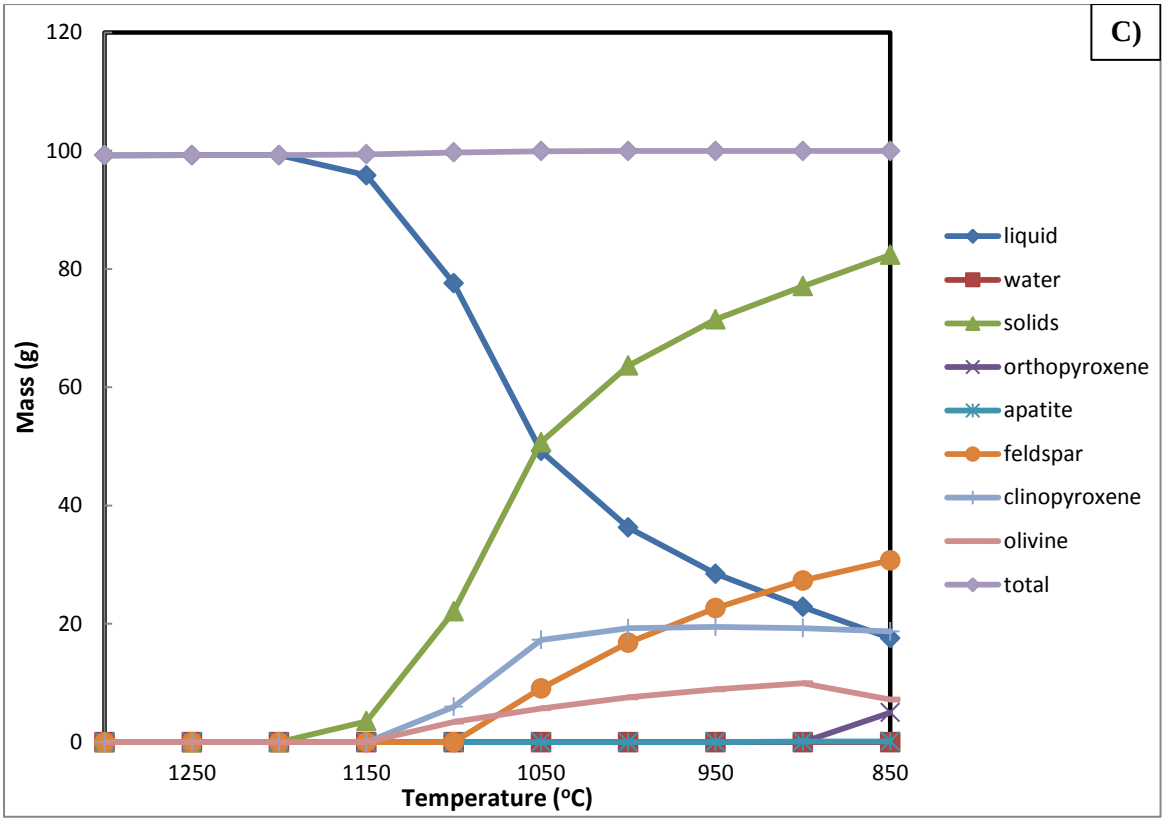

Figure 4.14: *The compatible against incompatible trace element variation diagram in logarithmic scale (**A**) and fractional crystallization model that explain the evolution of silicic volcanic product of BMC (**B** & **C**).*

In addition to the fractionation process crustal material contamination have a slight role in the evolution of the magma. The crustal contaminating material involvement is mainly verified from the contamination index (La/Nb) and little or no troughs of Nb and Ta in spidergram. Some of basaltic Boko samples show La/Nb ratio above 1; with maximum value of 1.2 that indicate contamination by crustal material. The diagram Ce/Pb and La/Nb against MgO and Th/Ta or La/Nb against SiO_2; which show a slight sub horizontal to inclined trend (Fig.4.15) suggest a minor contamination. In general the linking process between the silicic mafic volcanic products of BMC is fractional crystallization with a minor crustal material involvement.

The explanation about the gap between the mafic and silicic rocks is explained by different authors (eg., Peccerillo et al., 2007). Peccerillo et al. (2007) prescribe at shallow levels, magmas can fractionate in predominantly small magma bodies (dikes) and some larger magma chambers (e.g., nested calderas). On large magma chambers zoned reservoirs are produced with a peralkaline silicic upper layer and basalts at the bottom,

which is evidenced by geophysical investigation (eg., Rezene Mahastente et al., 1999). In this system, eruption preferentially taps the silicic layer, giving rise to the abundant silicic activity, whereas mafic melts reach the surface when fractures intersect the lower layer of the shallow chamber or reach some deep under plated basalt reservoirs. On Fig.4.14 (C) we can observe with a narrow temperature range the magma change from basic to acidic composition. That narrow temperature range is the field of intermediate magma formation. In another word the opportunity of forming an intermediate magma is very low during the fractionation process that rich to peralkaline magma.

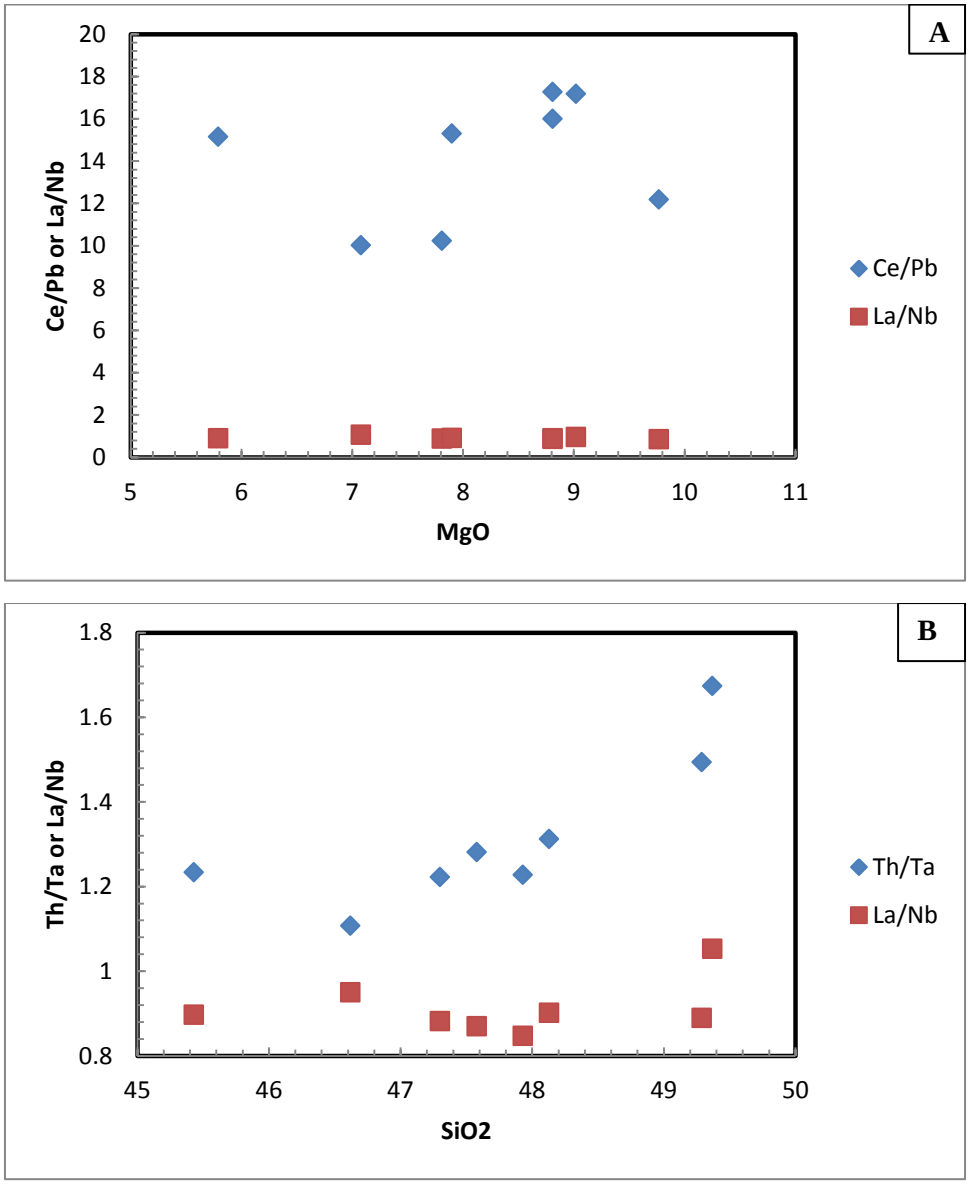

Figure 4.15: *Ce/Pb & La/Nb against MgO (**A**) and Th/Ta & La/Nb against SiO_2 (**B**) diagrams of mafic rock samples of Boko volcano.*

Chapter Five

5. Soil CO_2 Degassing and Eruptive History of BMC

5.1. Introduction

Different researches conducted in the last two decades show the importance of CO_2 degassing from active volcanoes to the atmosphere (Chiodini et al., 1998). Because of most volcanoes are associated with CO_2 degassing it's important to monitor and study related weakness zone for the transportation of fluids on active volcanoes by depending on CO_2 efflux spatial variation. The present study on the CO_2 degassing is basically relying on the insitu CO_2 concentration and flux measurement undertaken during the month February, 2016. Due to the influence of the meteorological parameters on the soil gas flux measurement result (Granieri et al., 2003) the surveys were carried out during dry season with stable weather conditions. The measurement is done by using portable gas analyzer; PP system equipped with SRC-1 chamber and EGM+4 (measuring range of 0–30,000 ppm, accuracy <1% of reading) that use accumulation chamber method. According to Tonani and Miele (1991), the accumulation chamber method is the best way to measure soil CO_2 values of volcanological-geothermal interest, as it is an absolute method that does not require either assumptions or corrections depending on soil characteristics.

The surveyed area covers 90 Km^2 and was investigated by 163 sample points. For the measurement of soil CO_2 the sampling technique applied is preplanned GPS points and systematic sampling. The preplanned GPS points are mainly applied on areas that show a similar CO_2 concentration and flux but for areas that show a bit variation in the measurement result the sample spacing is made a bit closer (up to 30 m). The preplanned GPS points have a sample spacing of 1000 m and 500 m. The 1000 m sample spacing is for areas those are expected to be lower measurement result and similar value of CO_2 concentration and flux. In order to understand the spatial variation of the CO_2 flux in the area, distribution of the samples are plotted by using ArcGIS, histogram-log probability diagrams are plotted by using SGeMS and the total amount of CO_2 degassing is estimated

by Sichel's t estimator method. SGeMS (Stanford Geostatistical Modeling Software) is an open-source computer package for solving problems involving spatially related variables.

5.2. CO_2 Flux and Concentration Distribution

Surface manifestations of deep geothermal activities are in the form of fumaroles, geysers, hot springs, hot grounds, steam, etc. (Tigistu Haile et al., 2000). According to Tigistu Haile et al. (2000) Boko thermal field is a vapor-dominated, dry type geothermal system tapping the deep-seated heat reservoirs of the shallow acidic volcanic center of Quaternary volcanics of the rift floor. Hydrothermal alterations of the major rock units in the area are witnessed by the surface manifestations of silica and extensive kaolinization that are suggestive of such an environment (Tamiru Alemayehu and Tigistu Haile, 2008; Tigistu Haile et al., 2000). Different works (Tamiru Alemayehu and Tigistu Haile, 2008; Tigistu Haile et al., 2000; Tamiru Alemayehu and Vernier, 1997) indicate that the Boko geothermal field heat source is a shallow magma chamber and the water mainly comes from meteoric source.

The hydrothermal alteration is dominantly restricted to the fault that runs along NE-SW direction on back side of Boko ridge. While an automated mapping approach using the spectral signature of these alteration facies (e.g., Crowley and Zimbelman, 1997) would be feasible to know the specific zones of alteration. The zones of hydrothermal alteration is well presented by the map of 5/7 band ratio combination developed by an ENVI software that clearly show clay minerals that are formed from the hydrothermal alteration process. The satellite image used is Landsat ETM+; downloaded from the site http://earthexplorer.usgs.gov/ with a capture date of February 26, 2015. Depending on the spectral signature 5/7 band ratio that show uniquely by filtering areas which have high water content. So in this case both clay rich rocks and vegetation looks like the same in the band ratio image. To differentiate the clay rich lithologies and the land covered by vegetation, field observation is used during development of geological map of the study area and NDVI image is developed to compare between the two images. On the NDVI image (Fig.5.1 (B)) the deep greenish color stands for vegetation rich spots. On the bottom right of the NDVI and 5/7 band ratio image, the area which show high reflectance is Wonji sugar plantation that is covered by dense sugar cane. In addition to the NDVI, from field observation, rather than the Wonji sugar plantation, other areas are covered by

scarce vegetation on the top of Boko ridge and NE-SW linearly aligned vegetation that found on the north eastern part of the area. From the observation as you see on the map (5/7 band ratio map) intensity of whitish in color shows the degree of the alteration and the enrichments of clay minerals in that specific spot. The intensity is high on the grid near to Easting 530000 m and Northing 940000 m that area is at which Boko fumarole is situated (Fig.5.1 (A) indicated by a box). The clay minerals that make the rhyolitic rock redish in color are also presented on the petrographic description; those are described as redish stains and included in the groundmass modal proportion. In addition to the petrographic description, the Ce concentrations for rhyolite rocks show erratic variation that comes due to the alteration process. The distribution of the clay enrichment shows geometry of circular to elliptical shape by following mainly the Boko ridge. Boko ridge is one of important morphological evidence for the occurrence of collapse event in the eruptive history.

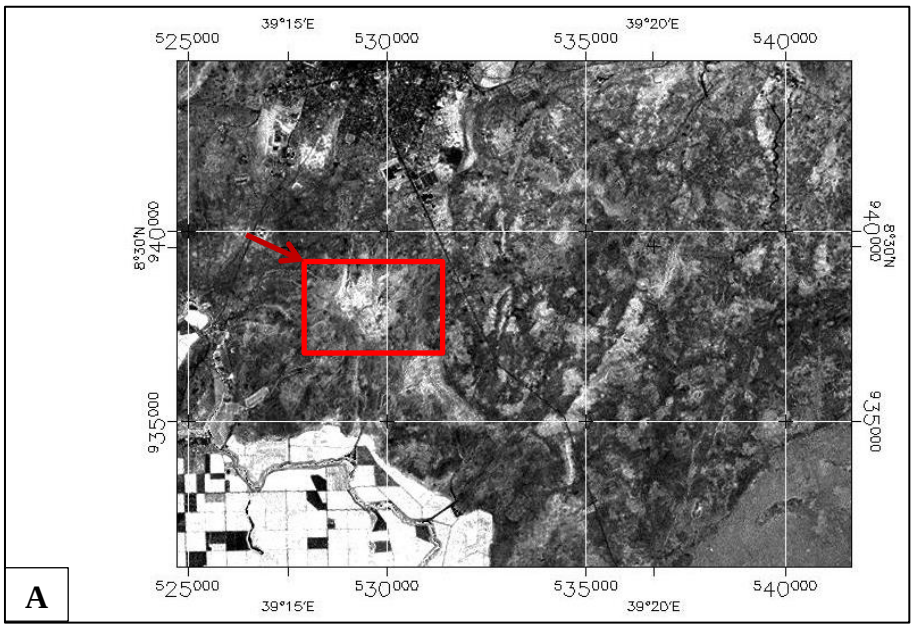

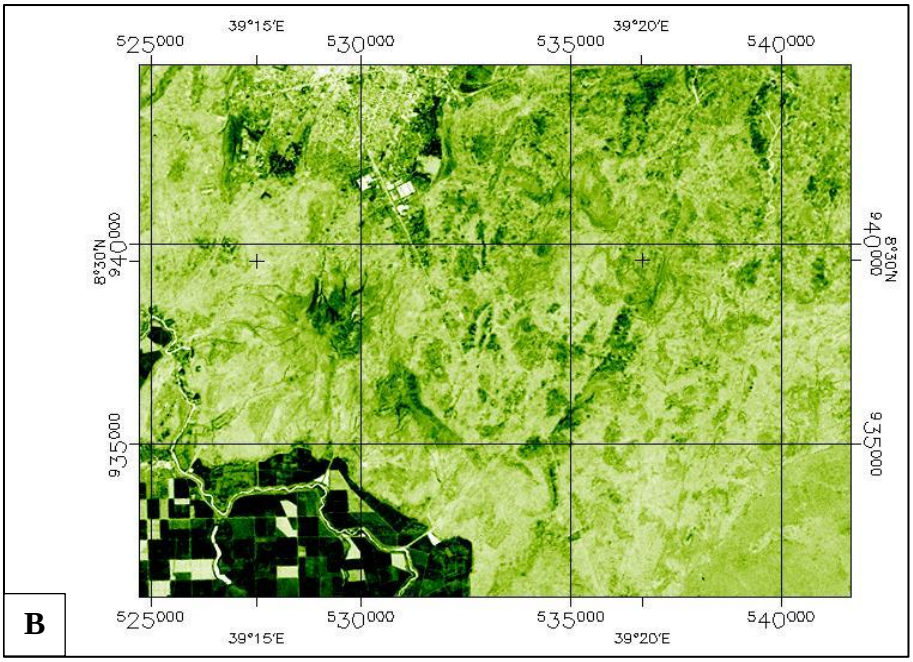

Figure 5.1: ***A****) 5/7 band ratio image. The rectangle indicated by the arrow is the Boko fumarole site.* ***B****) NDVI image and* ***C****) Photo picture of rhyolitic lava dome that is highly affected by the hydrothermal alteration near to Boko fumarole.*

At BMC the CO_2 degassing is explained by its concentration and flux value. The concentration and flux values show a slight variation. Selected sample points are presented on Table 5.1 but all 163 sample points flux and concentration values are fully presented on appendix IV. Concentration varies between 380 to 952 ppm and the flux

measurement range between 0 to 10.61 g m^{-2} d^{-1}. CO_2 flux value is an important parameter for studying the permeability of the measuring ground. Due to the low solubility of carbon in magmas, CO_2 is often released deep within the magmatic system. As a result there is a significant diffuse flux of magmatic gases through the volcanic edifice and surrounding area, which then contribute to soil gas emanation. In particular, numerous studies have been focused on the CO_2 soil diffuse degassing from quiescent active volcanoes. Most of these studies showed that gas is not released uniformly from the whole volcanic apparatus, but rather from relatively restricted regions, which were named diffuse degassing structures (DDS) (Chiodini et al., 2001 cited in Cardellini et al., 2003). By applying the procedure proposed by Sinclair (1974), a combination of two overlapping populations can be identified in the probability plot of the flux values. This bimodal distribution suggests the existence of two sources (biogenic and volcanic-hydrothermal) feed overall soil CO_2 diffuse degassing.

Table 5.1: *Selected representative CO_2 concentration and flux values.*

Way Pts.	Easting (m)	Northing (m)	Concentration (ppm)	Flux (g m^{-2} d^{-1})
12_15	537667	933560	423	0
19	537171	935036	418	0
TA_39	536120	940081	412	0.038016
TBA_14	532444	939086	402	0.076032
8	535151	933036	435	0.114048
3_24	532038	934592	426	0.19008
TBA_42	531692	935523	469	0.988416
TA_17	536754	935560	413.9	1.026432
TBA_26	529809	937266	541	2.128896
48	530047	937059	452	3.079296
TBA_20	530537	937211	790	6.994944
TBA_21	530527	937155	952	10.606464

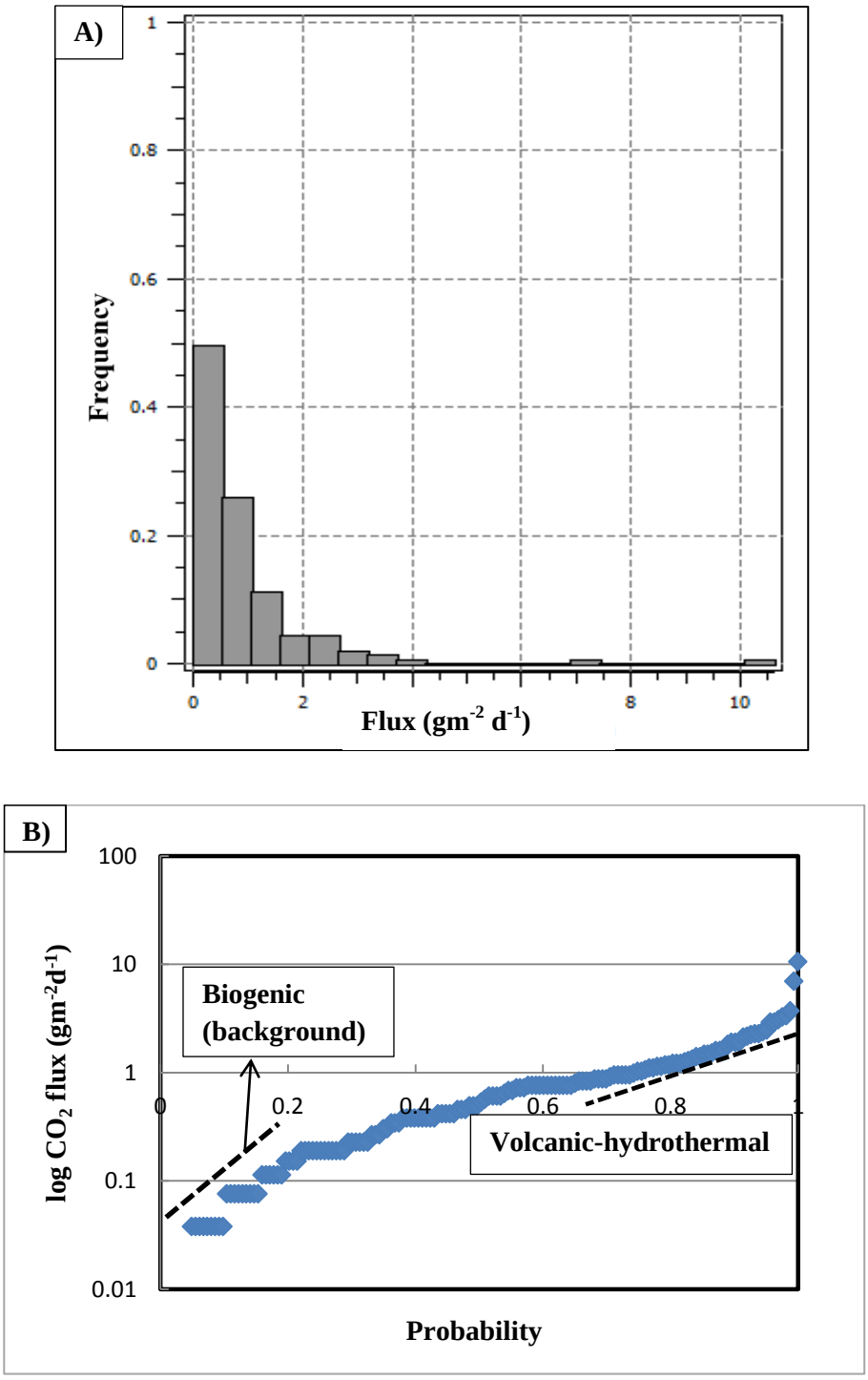

Figure 5.2: *Histogram (**A**) and log-probability (**B**) plot of CO_2 flux.*

The sample points that show a flux value above 1 g m^{-2} d^{-1} has a percentage of 25.15% from the total measurement and with an arithmetic mean of 2.14 g m^{-2} d^{-1}. The other population which shows a mixing between the two extreme populations takes the major proportion of the sample points with a percentage of 58.28% and the average value is 0.49 g m^{-2} d^{-1}. The second population covers 15.34% of the total sample points and it

have an average value of 0.041 g m^{-2} d^{-1}. The percentage distribution is also presented in form of frequency on the histogram plot (Fig.5.2). The flux values above 1 g m^{-2} d^{-1} mainly related to fault zones and the geothermal activity. As you see on the flux value distribution map (Fig.5.3) the values above 1 g m^{-2} d^{-1} that is painted by red is localized on the NNE-SSW major faults and on the caldera rims. The high value that is measured on near to the main road that runs from Nazret to Assela is another prospecting zone of a geothermal field in the BMC. Measurement that is taken 1000 m outside of the active volcano show a measurement value of flux 0.1 g m^{-2} d^{-1} that is taken as the background value for the flux that mainly comes from a biogenic source. The caldera floor that shows a low value of flux with a range below 0.1 g m^{-2} d^{-1} is mainly feed by a biogenic activity. But the rest of the area has a direct association to the geothermal activity and the diffuse degassing structures. Locally the CO_2 degassing varies in small amount. According to different authors (eg. Schöpa et al., 2011), the permeability variation at local scale may come from: lithological and topographic control. The topographic control is mainly seen on remnant of the caldera rim; Boko ridge. The influence of the topographic effect is explained by the conceptual model for the movement of fluids on Boko geothermal field by Tamiru Alemayehu and Vernier (1997). Tamiru Alemayehu and Vernier (1997) proposed that the geothermal fluid pass through the weakness found between each pile of flow bands and joints observed on the rhyolitic lava dome by following the topography. The effect of the lithologies are difficult to justify because of, it needs detail subsurface investigation at different spots. But we can see the subsurface lithological variation has a major role on the difference of CO_2 flux value within the caldera floor.

With respective to the spatial distribution of CO_2 flux measurement we can observe the three zones which show high value. The map on Fig.5.3 show that the highest flux value are measured close to the main fumarole fields suggesting that in that area CO_2 travels mostly with rising hydrothermal steam. The defusing structure found outside the caldera show intense degassing and extends with a general NNE-SSW direction along the northwestern caldera rim limit. The values are also high on the inner part of the caldera rim which is associated to morphological/topographic effect according to previous works (Frondini et al., 2004). The other zone is near to the left side of the road Nazret to Assela. This anomalous zone is also indicated by integrated geophysical investigation technique made by Tamiru Alemayehu and Tigistu Haile (2008). In this zone there is no any surface

manifestation of hydrothermal alteration. This kind of scenario is visible on Ohaaki West geothermal field (New Zealand) that suggests "blind" areas of sub-surface thermal activity (Rissmann et al., 2012). The third zone is found on the eastern margin of the area that might be related to buried ring fault covered by the pyroclastic material and post caldera collapse volcanic products.

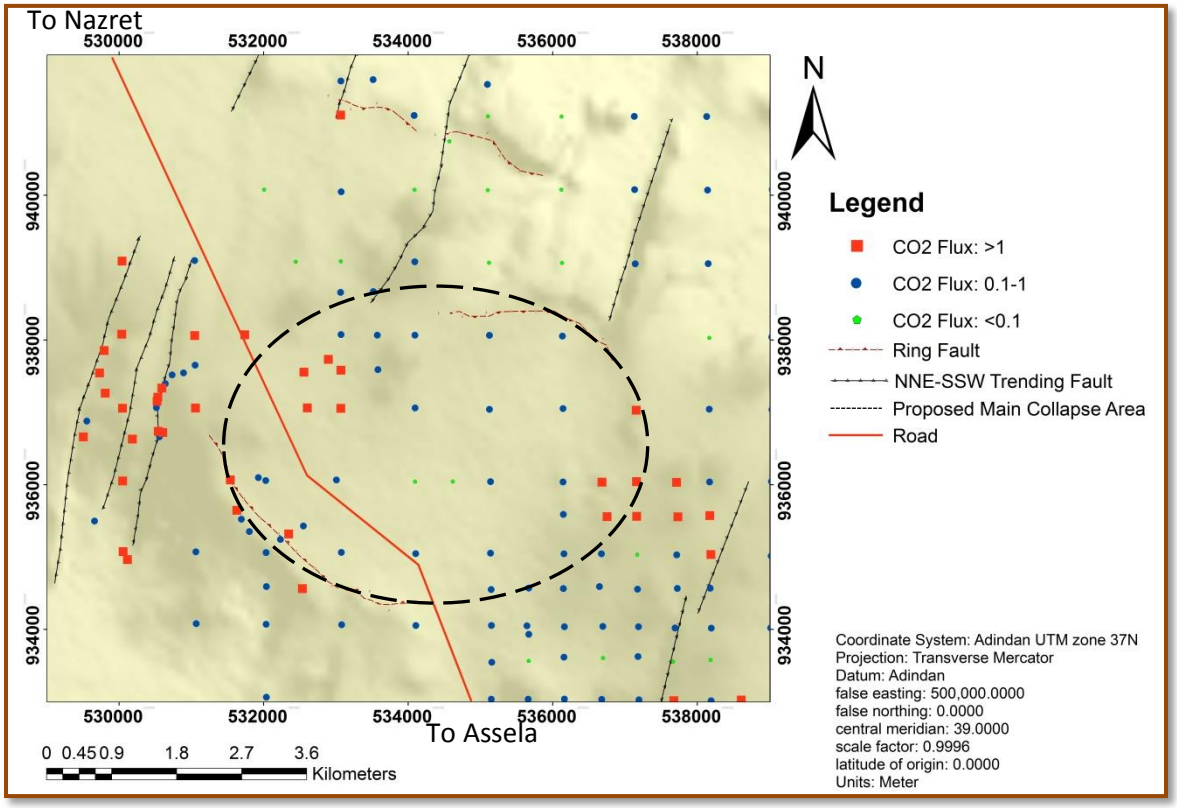

Figure 5.3: *Structural map overlay on digital elevation model that show the distribution of the CO_2 degassing survey points and the proposed main collapse area. The CO_2 flux values are expressed in g m^{-2} d^{-1}.*

By taking into account the sample spacing and areas which are difficult to access, the total CO_2 degassing to the atmosphere is estimated. According to Chiodini et al. (1998) total degassing can be calculated by multiplying the average flux value by the area of study. The estimation is for all population, when we come to each population the volcanic-hydrothermal source takes the major proportion. The calculation for each population is estimated by means of the Sichel's t estimator (after David, 1977). An evaluation of the area covered by each population (S_i) is obtained by multiplying the study area (S=90 Km^2=90,000,000 m^2) by the corresponding proportion of the population, f_i, (i.e.,$S_i = f_i S$). The total CO_2 output associated to each population is then

estimated multiplying S_i by mean of each population (M_i). The total CO_2 release from the entire studied area can be obtained summing the contribution of each population (i.e.,$\sum Sf_iM_i$). The calculation result shows volcanic-hydrothermal source takes the major proportion of 48.44 t d^{-1} and the other populations are presented on the Table 5.2. As a result of diffuse CO_2 flux occurs passively over wide areas and sparse sampling the total efflux of CO_2 is may be underestimated. The summation result of the two population gives BMC has a total degassing amount of 74.71 t d^{-1}. The CO_2 degassing from the volcanic-hydrothermal source is very minimal when it compares to Aluto volcano (57 t d^{-1} within 0.8 Km^2; Hutchison et al., 2015).

Table 5.2: *CO_2 concentration and flux value for the two populations and the overlapping flux value. The total CO_2 degassing is expressed in tonnes per day (td^{-1}).*

Populations	Mean CO_2 Concentration, ppm	Mean CO_2 Flux, g m^{-2} d^{-1}	Proportion, %	Total CO_2 Output, t d^{-1}
Biogenic	412.8	0.041	15.34	0.57
Mixed (overlapped)	428.8	0.49	58.28	25.70
Volcanic-hydrothermal	501.3	2.14	25.15	48.44
Total				74.71

5.3. Caldera Edifice

A caldera is wide topographic basin that results from collapse event and normally has inward-facing caldera walls or scarps surrounded by an elevated topographic rim (Sigurdsson et al., 2015). Several previous studies have suggested that BMC has undergone a caldera forming event (Tigistu Haile et al., 2000; Tamiru Alemayehu and Tigistu Haile, 2008; Tamiru Alemayehu and Vernier, 1997; Boccaleti et al., 1999). Taking together the presence of a remnant caldera rim, the occurrence of mafic cones along the proposed ring structure, the presence and correspondence of hydrothermal alteration to these zones and local peaks in CO_2 degassing; can support the presence of caldera.

The caldera edifice in the case of Boko is difficult to outline. Morton et al. (1979) suggest the Boko caldera to cone diameter ratio is probably close to 1, so that the caldera collapse led to the destruction of the cone remnant. The field observation tells the complex is highly affected by erosional process, post caldera eruptions and tectonic activities. This is typical of peralkaline volcanic edifices which undergo repeated phases of caldera collapse and caldera-filling volcanism (Cole et al., 2005).

The erosional process mainly affects and still affecting the pyroclastic volcanic products on the western side of the area. On that portion there are some remnants of the pyroclastic volcanic products. The eastern part of the area is mainly affected by a tectonic and volcanic activity. The mafic cones strictly follow some kind of a ring structure if you observe the geological map of the complex carefully. That might be emplacement of mafic cones feed through the ring fault. In that case it shows to some extent the outline of the caldera on the south eastern portion of the study area. This kind of setup is observed in Aluto volcano (Hutchison et al., 2015). The CO_2 flux measurement result also confirms the presence of a weakness zone that increases the overall permeability at that area. The major faults that trend NNE-SSW are the other post collapse event that obscures the ring structure mainly on the south western margin of the study area. From the field observation, satellite image analysis, digital elevation model analysis and CO_2 flux value distribution the caldera main collapse boundary is outlined in Fig.5.3 and Fig.5.4. The caldera edifice outline is also evidenced by the absolute bouguer anomaly map of the area that is developed by Tamiru Alemayehu and Tigistu Haile (2008). The caldera main collapse has an elliptical geometry with major axis of 6 Km along E-W direction and minor axis of 4 Km along N-S direction. The caldera has an ellipticity (short/long axis ratio) of 0.667. The nesting nature of the ring fault indicates the existence of wider caldera collapse in addition to the main collapse zone. The subsidence area displays E–W elongation similar to that proposed for other volcanoes in the MER (e.g. Rampey et al., 2010; Hutchison et al., 2015).

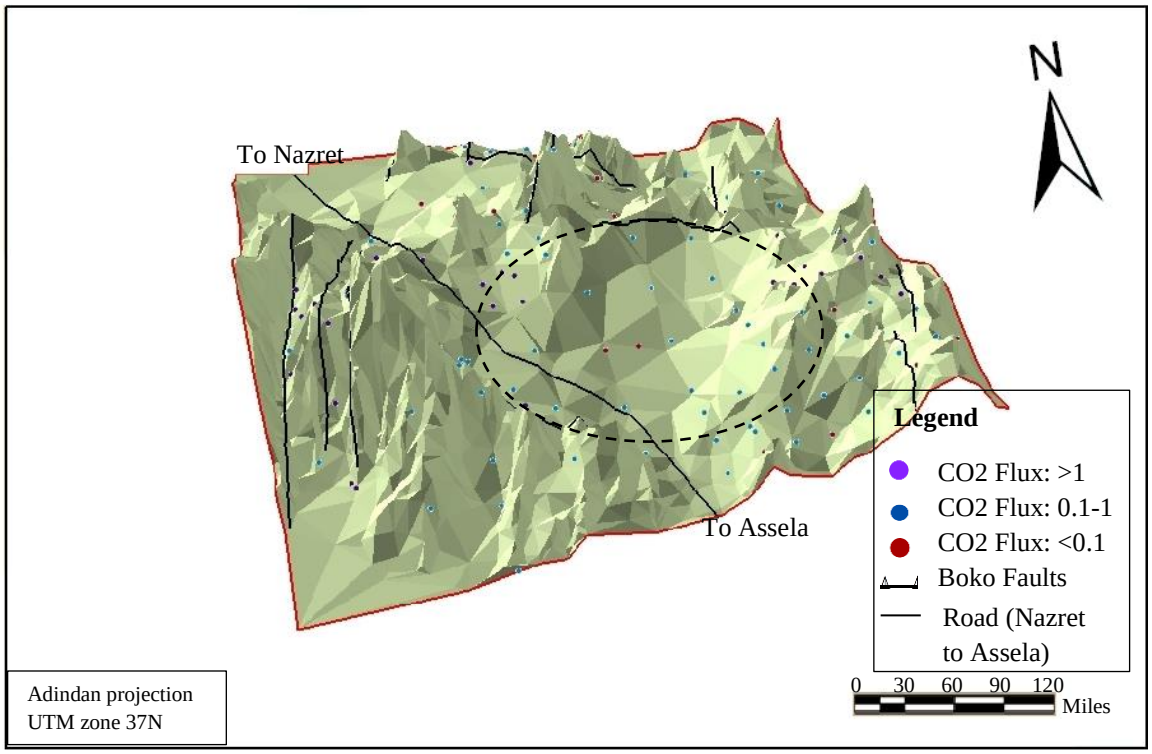

Figure 5.4: *Three dimensional digital elevation model of BMC with proposed main collapse area shown by a broken line that forms an ellipse shape.*

5.4. Correlation and Eruptive History of BMC

The composite stratigraphy of BMC is correlated with the regional stratigraphy made by Boccaletti et al. (1999) by depending on the petrological and geochemical characteristics of the rocks (Fig.5.5). The correlation result indicates rhyolitic lava flow, pumice flow, ignimbrite, lower pumice fall, rhyolitic lava dome and obsidian correlate to Boku-Tede unit. Bofa basalt of the regional stratigraphy is mainly composed of transitional basalt with large laths of plagioclase phenocryst. Because of this Lower basalt is correlated to Bofa unit. Upper ash flow correlate with poorly welded lithics comprising regional unit called Dera-Sodore unit. Finally the last volcanic products; scoria and upper basalt correlated to Melkasa unit or Wonji unit (of Alula Damte et al., 1992). The upper basalt and scoria are transitional to weakly subalkaline but the regional correspondent, Wonji unit of Alula Damte et al. (1992) is alkaline. But the petrographic analysis and field observation suggest the correlating regional stratigraphy is Melkasa unit for the upper mafic volcanic product. As a result, detail geochemistry analysis of the recent basalt is recommended for the future.

The radioactive dating after Bigazzi et al. (1993) and Morton et al. (1979) that is presented in Boccaletti et al. (1999) suggest the age of each major units; 0.51-0.83 Ma: Boku-Tede unit, 0.44-0.61 Ma: Bofa unit and 0.61-0.23 Ma: Melkasa unit. From the composite stratigraphy and correlation result, Boko caldera forming eruption activity occurred between 0.51-0.83 Ma. The stratigraphic arrangement of the volcanic products in the Boku-Tede unit tells the nature of the eruption is non-explosive at first then explosive and finally become non-explosive. After that massive eruption post Boko caldera eruptive activities are followed. The post Boko caldera eruptive activity emplaces; lower basalt (at the age of 0.44-0.61 Ma), upper ash flow and scoria then upper basalt (0.16-0.23 Ma).

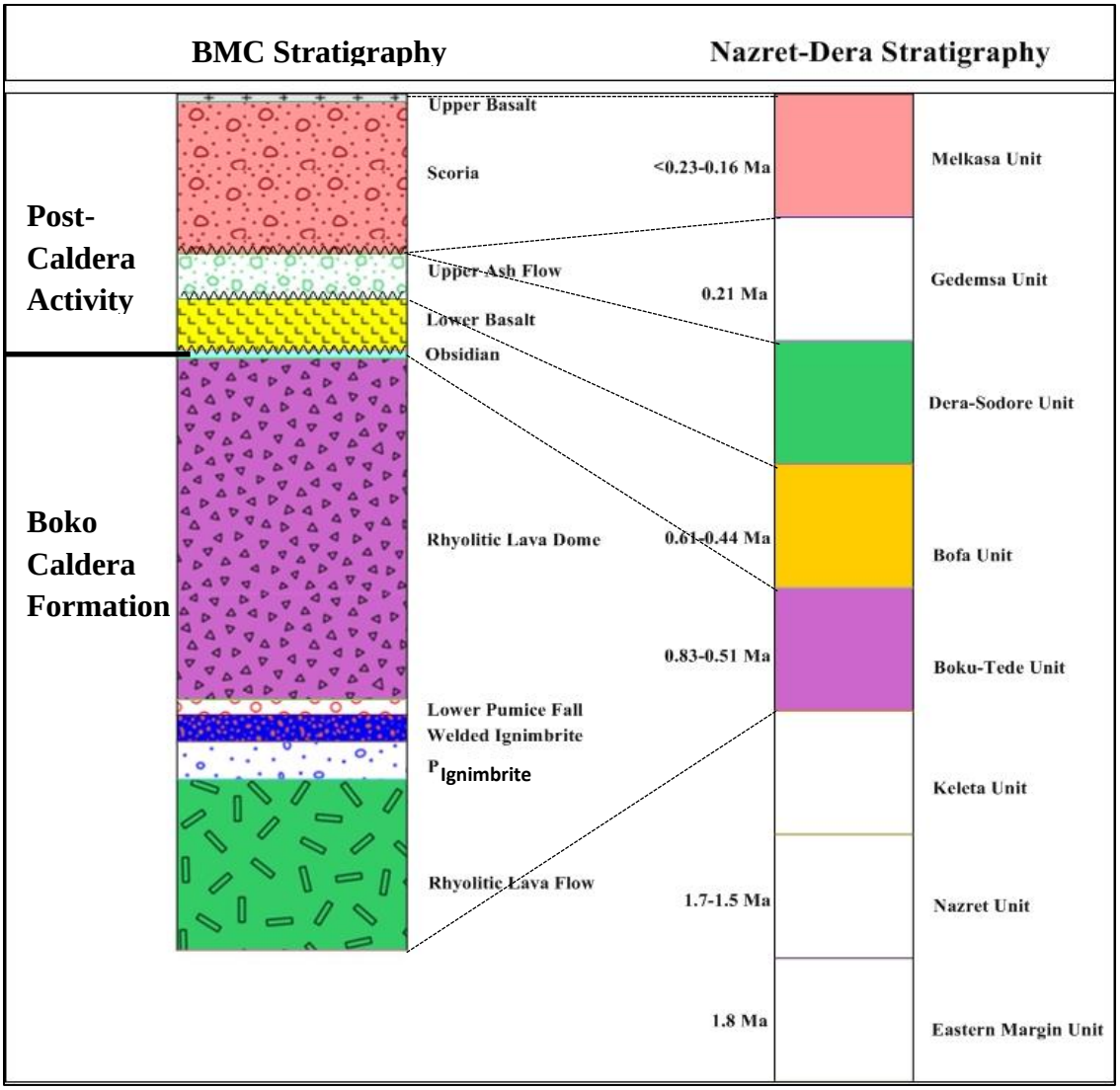

Figure 5.5: *Litho-stratigraphic correlation between BMC and Nazret-Dera area. The Nazret-Dera area stratigraphy is developed by Boccaletti et al. (1999).*

Chapter Six

6. Conclusion and Recommendation

6.1. Conclusion

A combination of remote sensing, field mapping, petrography, structural analysis, geochemistry and soil CO_2 degassing surveys provide new perceptions about eruptive history and magmatic evolution of the Boko magmatic complex. The main outcomes of this study are:

1. Boko magmatic complex is composed of volcanic products sourced from two main episodes of volcanic activity; Boko caldera forming eruptive activity and post caldera eruptive activity. The Boko caldera forming activity is non-explosive at initial phase then explosive and finally again become non explosive. This eruptive activity occurred during 0.51-0.83 Ma. The main volcanic products are rhyolitic lava flow, pumice flow, ignimbrite, lower pumice fall, rhyolitic lava dome and obsidian. The post caldera forming volcanic activity occurred during 0.16-0.61 Ma. This activity gives a main volcanic rocks; lower basalt, upper ash flow, scoria and upper basalt.

2. The geological structures observed on the study area are flow banding, joints and NNE-SSW trending major faults that imitate the regional tectonic structure of the Main Ethiopian Rift. The major fault displaces the youngest, basaltic unit that indicates the tectonic process is active after 0.16 Ma.

3. The geochemistry tells the rocks are mainly bimodal, which lacks intermediate composition. The chemical compositions are mainly basaltic and silicic. The basalts are transitional to weakly subalkaline and the silicic rocks are dominantly peralkaline rhyolite.

4. The geochemistry result imply the two groups of the rock; basaltic and peralkaline rhyolite has the same source. The major element Harker diagram, trace element modeling, REE variation diagram and multi element variation diagram of the two rock groups imply the rocks are linked by a fractional crystallization process with

minor contamination. In order to form Boko peralkaline rocks, the basaltic rock need to crystallize by 80% degree of crystallization.

5. The soil CO_2 degassing measurement result show the CO_2 degassing is generated from biogenic and volcanic-hydrothermal source. The total flux from the two sources is 74.71 t d^{-1}. The mean of CO_2 flux of the biogenic is 0.041 g m^{-2} d^{-1} and volcanic-hydrothermal is 2.14 g m^{-2} d^{-1}. The CO_2 degassing and surface manifestations indicate Boko still has an active volcanic process beneath the volcano.

6. The combination of remote sensing, soil CO_2 flux value distribution, field mapping and structural data analysis suggest the main collapse zone of Boko caldera has a dimension of 6 Km (E-W) by 4 Km. The major axis is along E-W which is in agreement with the regional stress direction.

6.2. Recommendation

Measurement of CO_2 flux in geothermal prospects has proven to be a useful technique in the tool kit for the exploration geologist/geochemist during the early stages of geothermal exploration. The technique is relatively low cost and provides results in real time allowing for dynamic adaptation of the survey design in response to results. In case of our country, CO_2 degassing is not commonly applied technique for geothermal exploration. Applying this technique may be useful to improve uncertainties in initial stage of geothermal exploration, especially in case of blind geothermal field. The future research opportunity in Boko magmatic complex includes detail work on the eruptive history that includes; the ejecting energy, angle and distance of the pyroclastic material. Isotope analysis is a strong tool to understand magma evolution. So isotope geochemistry is suggested for further substantiation of the source and petrogenesis of the peralkaline rocks.

Reference

Abbate, E. and Sagri, M. (1980). Volcanites of Ethiopian and Somali Plateaus and major tectonic lines. *Atti Convegni Lincei* **47**:219-227.

Alula Damte, Boccaletti M., Mazzuoli R, Getaneh Assefa and Tortorici L. (1992). Geological map of the Nazareth Dera Region (Main Ethiopian Rift). Scale 1:50,000. S.E.L.C.A., Florence, Italy.

Asfawossen Asrat and Barbey, P. (2003). Petrology, geochronology and Sr–Nd isotopic geochemistry of the Konso pluton, south-western Ethiopia: implications for transition from convergence to extension in the Mozambique Belt. *International Journal of Earth Sciences* **92**(6):873-890.

Aspinall, W., Auker, M., Hincks, T., Mahony, S., Nadim, F., Pooley, J., . . . Syre, E. (2011). Volcano hazard and exposure in GFDRR priority countries and risk mitigation measures. *Volcano Risk Study 0100806-00-1-R*.

Bastow, I., Stuart, G., Kendall, J. and Ebinger, C. (2005). Upper-mantle seismic structure in a region of incipient continental breakup: northern Ethiopian rift. *Geophysical Journal International* **162**(2):479-493.

Bekele Abebe, Acocella, V., Tesfaye Korme and Dereje Ayalew (2007). Quaternary faulting and volcanism in the Main Ethiopian Rift. *Journal of African Earth Sciences* **48**(2):115-124.

Bekele Abebe, Boccaletti, M., Mazzuoli, M., Bonini, M., Tortorici, L. and Trua, T. (1998). Geological map of the Lake Ziway-Asela region (Main Ethiopian Rift). scale 1: 50,000. *Cons. Naz. delle Ric., ARCA, Florence*.

Bigazzi, B., Bonadonna, F., Di Paola, G. and Giuliani, A. (1993). K-Ar and fission track ages of the last volcano tectonic phase in the Ethiopian Rift Valley (Tullu Moye area). *Geology and mineral resources of Somalia and surrounding regions. Istituto Agronomico Oltremare, Firenze, Relazioni Monografie* **113:**311-322.

Boccaletti, M., Bonini, M., Mazzuoli, R., Bekele Abebe, Piccardi, L. and Tortorici, L. (1998). Quaternary oblique extensional tectonics in the Ethiopian Rift (Horn of Africa). *Tectonophysics* **287**(1):97-116.

Boccaletti, M., Mazzuoli, R., Bonini, M., Trua, T. and Bekele Abebe (1999). Plio-Quaternary volcanotectonic activity in the northern sector of the Main Ethiopian

Rift: relationships with oblique rifting. *Journal of African Earth Sciences* **29**(4):679-698.

Bonini, M., Corti, G., Innocenti, F., Manetti, P., Mazzarini, F., Tsegaye Abebe and Pecskay, Z. (2005). Evolution of the Main Ethiopian Rift in the frame of Afar and Kenya rifts propagation. *Tectonics* **24**(1).

Bonnefille, R. (2010). Cenozoic vegetation, climate changes and hominid evolution in tropical Africa. *Global and Planetary Change* **72**(4):390-411.

Bosworth, W., Strecker, M. and Blisniuk, P. (1992). Integration of east African Paleostress and present-day stress data: Implications for continental stress field dynamics. *Journal of Geophysical Research: Solid Earth (1978–2012)* **97**(B8):11851-11865.

Boynton, W. (1984). *Cosmochemistry of the rare earth elements.* Elsevier.

Calais, E., Ebinger, C., Hartnady, C. and Nocquet, J. (2006). Kinematics of the East African Rift from GPS and earthquake slip vector data. *Special Publication-Geological Society of London* **259:**9-22.

Cardellini, C., Chiodini, G. and Frondini, F. (2003). Application of stochastic simulation to CO_2 flux from soil: mapping and quantification of gas release. *Journal of Geophysical Research: Solid Earth* **108**(B9).

Chiodini, G., Cioni, R., Guidi, M., Raco, B. and Marini, L. (1998). Soil CO_2 flux measurements in volcanic and geothermal areas. *Applied Geochemistry* **13**(5):543-552.

Chiodini, G., Frondini, F., Cardellini, C., Granieri, D., Marini, L. and Ventura, G. (2001). CO_2 degassing and energy release at Solfatara volcano, Campi Flegrei, Italy. *Journal of Geophysical Research: Solid Earth* **106**(B8):16213-16221.

Chorowicz, J. (2005). The east African rift system. *Journal of African Earth Sciences* **43**(1):379-410.

Cole, J., Milner, D. and Spinks, K. (2005). Calderas and caldera structures: a review. *Earth-Science Reviews* **69**(1):1-26.

Corti, G. (2009). Continental rift evolution: from rift initiation to incipient break-up in the Main Ethiopian Rift, East Africa. *Earth-Science Reviews* **96**(1):1-53.

Crowley, J. and Zimbelman, D. (1997). Mapping hydrothermally altered rocks on Mount Rainier, Washington, with airborne visible/infrared imaging spectrometer (AVIRIS) data. *Geology* **25**(6):559-562.

Daly, E., Keir, D., Ebinger, C., Stuart, G., Bastow, I. and Atalay Ayele (2008). Crustal tomographic imaging of a transitional continental rift: the Ethiopian rift. *Geophysical Journal International* **172**(3):1033-1048.

David, M. (1977). *Geostatistical ore reserve estimation (Developments in Geomathematics 2)*. Elsevier, New York, 364 pp.

Dereje Ayalew, Di Vito, M., Isaia, R., Orsi, G. and Gezahegn Yirgu (2003). The Gedemsa caldera (Main Ethiopian Rift): an example of interplay among regional tectonism, volcanism and volcano-tectonics. **In**: *EGS-AGU-EUG Joint Assembly*, PP. 5919.

Di Paola, G. (1971). Geology of the Corbetti Caldera area (Main Ethiopian Rift Valley). *Bulletin Volcanologique* **35**(2):497-506.

Ebinger, C., Bechtel, T., Forsyth, D. and Bowin, C. (1989). Effective elastic plate thickness beneath the East African and Afar plateaus and dynamic compensation of the uplifts. *Journal of Geophysical Research: Solid Earth (1978–2012)* **94**(B3):2883-2901.

Ebinger, C. and Casey, M. (2001). Continental breakup in magmatic provinces: An Ethiopian example. *Geology* **29**(6):527-530.

Ebinger, C., Deino, A., Tesha, A., Becker, T. and Ring, U. (1993). Tectonic controls on rift basin morphology: evolution of the Northern Malawi (Nyasa) Rift. *Journal of Geophysical Research: Solid Earth (1978–2012)* **98**(B10):17821-17836.

Ebinger, C., Tilahun Yemane, Harding, D., Samson Tesfaye, Kelley, S. and Rex, D. (2000). Rift deflection, migration, and propagation: linkage of the Ethiopian and Eastern rifts, Africa. *Geological Society of America Bulletin* **112**(2):163-176.

Ewart, A. and Griffin, W. (1994). Application of proton-microprobe data to trace-element partitioning in volcanic rocks. *Chemical Geology* **117**(1):251-284.

Fontijn, K., Elburg, M., Nikogosian, I., van Bergen, M. and Ernst, G. (2013). Petrology and geochemistry of Late Holocene felsic magmas from Rungwe volcano (Tanzania), with implications for trachytic Rungwe Pumice eruption dynamics. *Lithos* **177:**34-53.

Frondini, F., Chiodini, G., Caliro, S., Cardellini, C., Granieri, D. and Ventura, G. (2004). Diffuse CO_2 degassing at Vesuvio, Italy. *Bulletin of Volcanology* **66**(7):642-651.

Gasparon, M., Innocenti, F., Manetti, P., Peccerillo, A. and Tsegaye Abebe (1993). Genesis of the Pliocene to Recent bimodal mafic-felsic volcanism in the Debre

Zeyt area, central Ethiopia: volcanological and geochemical constraints. *Journal of African Earth Sciences (and the Middle East)* **17**(2):145-165.

Gezahegn Yirgu, Ebinger, C. and Maguire, P. (2006). The afar volcanic province within the East African Rift System: introduction. *Geological Society, London, Special Publications* **259**(1):1-6.

Gidey Woldegabriel, Aronson, J. L. and Walter, R. C. (1990). Geology, geochronology, and rift basin development in the central sector of the Main Ethiopia Rift. *Geological Society of America Bulletin* **102**(4):439-458.

Giordano, F., D'Antonio, M., Civetta, L., Tonarini, S., Orsi, G., Dereje Ayalew, . . . Isaia, R. (2014). Genesis and evolution of mafic and felsic magmas at Quaternary volcanoes within the Main Ethiopian Rift: Insights from Gedemsa and Fanta'Ale complexes. *Lithos* **188:**130-144.

Granieri, D., Chiodini, G., Marzocchi, W. and Avino, R. (2003). Continuous monitoring of CO_2 soil diffuse degassing at Phlegraean Fields (Italy): influence of environmental and volcanic parameters. *Earth and Planetary Science Letters* **212**(1):167-179.

Gregory, J. (1896). *The Great Rift Valley*. John Murray, London.

Gupta, R. P. (2013). *Remote sensing geology*. Springer Science & Business Media.

Hayward, N. and Ebinger, C. (1996). Variations in the along-axis segmentation of the Afar Rift system. *Tectonics* **15**(2):244-257.

http://earthexplorer.usgs.gov/ accessed on 06.02.2016

http://en.climate-data.org/location/2108/ accessed on 26.01.2016.

Hutchison, W. (2015). Past, present and future volcanic activity at restles calderas in the Main Ethiopian Rift. Unpublished Phd. thesis, University of Oxford, Oxford, Uk, 285 PP.

Hutchison, W., Mather, T. A., Pyle, D. M., Biggs, J. and Gezahegn Yirgu (2015). Structural controls on fluid pathways in an active rift system: A case study of the Aluto volcanic complex. *Geosphere* **11**(3):542-562.

Irvine, T. and Baragar, W. (1971). A guide to the chemical classification of the common volcanic rocks. *Canadian journal of earth sciences* **8**(5):523-548.

Keir, D., Ebinger, C., Stuart, G., Daly, E. and Atalay Ayele (2006). Strain accommodation by magmatism and faulting as rifting proceeds to breakup:

seismicity of the northern Ethiopian rift. *Journal of Geophysical Research: Solid Earth (1978–2012)* **111**(B5).

Keranen, K. M., Klemperer, S. L., Julia, J., Lawrence, J. F. and Nyblade, A. A. (2009). Low lower crustal velocity across Ethiopia: Is the Main Ethiopian Rift a narrow rift in a hot craton? *Geochemistry, Geophysics, Geosystems* **10**(5).

Kieffer, B., Arndt, N., Lapierre, H., Bastien, F., Bosch, D., Pecher, A., . . . Jerram, D. A. (2004). Flood and shield basalts from Ethiopia: Magmas from the African superswell. *Journal of Petrology* **45**(4):793-834.

Klerkx, J., Theunissen, K. and Delvaux, D. (1998). Persistent fault controlled basin formation since the Proterozoic along the Western Branch of the East African Rift. *Journal of African Earth Sciences* **26**(3):347-361.

Leakey, R. E. (1973). Evidence for an advanced plio-pleistocene hominid from East Rudolf, Kenya. *Nature* **242**(5398):447-450.

Le Bas, M. J., Le Maitre, R., Streckeisen, A. and Zanettin, B. (1986). A chemical classification of volcanic rocks based on the total alkali-silica diagram. *Journal of Petrology* **27**(3):745-750.

Macdonald, R. (1974). Nomenclature and petrochemistry of the peralkaline oversaturated extrusive rocks. *Bulletin Volcanologique* **38**(2):498-516.

Macgregor, D. (2015). History of the development of the East African Rift System: A series of interpreted maps through time. *Journal of African Earth Sciences* **101:** 232-252.

Mackenzie, G., Thybo, H. and Maguire, P. (2005). Crustal velocity structure across the Main Ethiopian Rift: results from two-dimensional wide-angle seismic modelling. *Geophysical Journal International* **162**(3):994-1006.

Maguire, P., Keller, G., Klemperer, S., Mackenzie, G., Keranen, K., Harder, S.,…Khan, M. (2006). Crustal structure of the northern Main Ethiopian Rift from the EAGLE controlled-source survey; a snapshot of incipient lithospheric break-up. *Geologycal Society, London, Special Publications* **259**(1):269-292.

McDonough, W. F. and Sun, S.S. (1995). The composition of the Earth. *Chemical Geology* **120**(3):223-253.

Mengist Teklay, Kröner, A., Mezger, K. and Oberhänsli, R. (1998). Geochemistry, Pb-Pb single zircon ages and Nd-Sr isotope composition of Precambrian rocks from

southern and eastern Ethiopia: implications for crustal evolution in East Africa. *Journal of African Earth Sciences* **26**(2):207-227.

Mohr, P. (1971). Ethiopian Rift and plateaus: some volcanic petrochemical differences. *Journal of Geophysical Research* **76**(8):1967-1984.

Mohr, P. (1983a). The Morton-Black hypothesis for the thinning of continental crust—revisited in western Afar. *Tectonophysics* **94**(1):509-528.

Mohr, P. (1983b). Volcanotectonic aspects of Ethiopian rift evolution. *Bulletin Centre Recherches Elf Aquitaine Exploration Production* **7:**175-189.

Mohr, P. and Zanettin, B. (1988). The Ethiopian flood basalt province. **In**: *Continental flood basalts*, pp. 63-110: Springer, Netherlands.

Morley, C. (1999). Tectonic evolution of the East African Rift System and the modifying influence of magmatism. *Acta vulcanologica* **11:**1-20.

Morton, W. (1979). Riftward younging of volcanic units in the Addis Ababa region, Ethiopian rift valley. *Nature* **280:**284-288.

Mulugeta Alene, Ruffini, R. and Sacchi, R. (2000). Geochemistry and geotectonic setting of Neoproterozoic rocks from northern Ethiopia (Arabian-Nubian Shield). *Gondwana Research* **3**(3):333-347.

Mulugeta Dugda, Nyblade, A. and Julia, J. (2007). Thin lithosphere beneath the Ethiopian Plateau revealed by a joint inversion of Rayleigh wave group velocities and receiver functions. *Journal of Geophysical Research: Solid Earth (1978–2012)* **112**(B8).

Mulugeta Dugda, Nyblade, A., Julia, J., Langston, C., Ammon, C. and Simiyu, S. (2005). Crustal structure in Ethiopia and Kenya from receiver function analysis: implications for rift development in eastern Africa. *Journal of Geophysical Research: Solid Earth (1978–2012)* **110**(B1).

Pearce, T. (1970). Chemical variations in the Palisade Sill. *Journal of Petrology* **11**(1):15-32.

Peccerillo, A., Barberio, M., Gezahegn Yirgu, Dereje Ayalew, Barbieri, M. and Wu, T. (2003). Relationships between mafic and peralkaline silicic magmatism in continental rift settings: a petrological, geochemical and isotopic study of the Gedemsa volcano, central Ethiopian rift. *Journal of Petrology* **44**(11).

Peccerillo, A., Donati, C., Santo, A., Orlando, A., Gezahegn Yirgu and Dereje Ayalew (2007). Petrogenesis of silicic peralkaline rocks in the Ethiopian rift: geochemical

evidence and volcanological implications. *Journal of African Earth Sciences* **48**(2):161-173.

Rampey, M. L., Oppenheimer, C., Pyle, D. M. and Gezahegn Yirgu (2010). Caldera-forming eruptions of the Quaternary Kone volcanic complex, Ethiopia. *Journal of African Earth Sciences* **58**(1):51-66.

Reimer, G. (1980). Use of soil-gas helium concentrations for earthquake prediction: Limitations imposed by diurnal variation. *Journal of Geophysical Research: Solid Earth* **85**(B6):3107-3114.

Rezene Mahatsente, Jentzsch, G. and Jahr, T. (1999). Crustal structure of the Main Ethiopian Rift from gravity data: 3-dimensional modeling. *Tectonophysics* **313**(4):363-382.

Ring, U. (2014). The East African Rift System. *Austrian J Earth Sci* **107**(1):132-146.

Rissmann, C., Christenson, B., Werner, C., Leybourne, M., Cole, J. and Gravley, D. (2012). Surface heat flow and CO_2 emissions within the Ohaaki hydrothermal field, Taupo Volcanic Zone, New Zealand. *Applied Geochemistry* **27**(1):223-239.

Rollinson, H.R. (1993). *Using geochemical data: evaluation, presentation, interpretation*: Routledge.

Rooney, T., Furman, T., Bastow, I., Dereje Ayalew and Gezahegn Yirgu (2007). Lithospheric modification during crustal extension in the Main Ethiopian Rift. *Journal of Geophysical Research: Solid Earth (1978–2012)* **112**(B10).

Schöpa, A., Pantaleo, M. and Walter, T. (2011). Scale-dependent location of hydrothermal vents: Stress field models and infrared field observations on the Fossa Cone, Vulcano Island, Italy. *Journal of Volcanology and Geothermal Research* **203**(3):133-145.

Schrenk, F., Bromage, T. G., Betzler, C. G., Ring, U. and Juwayeyi, Y. M. (1993). Oldest Homo and Pliocene biogeography of the Malawi rift. *Nature* **365**(6449):833-836.

Segal, D. B. (1983). Use of Landsat multispectral scanner data for the definition of limonitic exposures in heavily vegetated areas. *Economic Geology* **78**(4):711-722.

Sigurdsson, H., Houghton, B., McNutt, S., Rymer, H. and Stix, J. (2015). *The encyclopedia of volcanoes*: Elsevier.

Sinclair, A. (1974). Selection of threshold values in geochemical data using probability graphs. *Journal of Geochemical Exploration* **3**(2):129-149.

Stamps, D. S., Calais, E., Saria, E., Hartnady, C., Nocquet, J. M., Ebinger, C. J. and Fernandes, R. M. (2008). A kinematic model for the East African Rift. *Geophysical Research Letters* **35**(5).

Tadiwos Chernet (1995). Petrological, geochemical and geochronological investigation of volcanism in the Northern Main Ethiopian Rift-Southern Afar transition region. Unpublished Phd. Thesis, Miami University, Ohio, USA.

Tamiru Alemayehu and Tigistu Haile (2008). Geophysical exploration of the Boku geothermal area, Central Ethiopian Rift. *Geothermics* **37**(6):586-596.

Tamiru Alemayehu and Vernier, A. (1997). Conceptual model for Boku hydrothermal area (Nazareth), Main Ethiopian Rift Valley. *SINET: Ethiopian Journal of Science* **20**(2):283-291.

Tigistu Haile, Tamiru Alemayehu and Ranieri, G. (2000). Geophysical, Geological and Hydrogeological Investigations of Boku thermal field, Nazareth, Ethiopia. **In:** *Twenty-Fifth Workshop on Geothermal Reservoir Engineering*, pp. 1-8. California, USA.

Tonani, F. and Miele, G. (1991). Methods for measuring flow of carbon dioxide through soils in the volcanic setting. **In**: *International Conference on Active Volcanoes and Risk Mitigation*, IAVCEI, Naples, Italy.

Trua, T., Deniel, C. and Mazzuoli, R. (1999). Crustal control in the genesis of Plio-Quaternary bimodal magmatism of the Main Ethiopian Rift (MER): geochemical and isotopic (Sr, Nd, Pb) evidence. *Chemical Geology* **155**(3):201-231.

Tsegaye Abebe, Mazzarini, F., Innocenti, F. and Manetti, P. (1998). The Yerer-Tullu Wellel volcanotectonic lineament: A transtensional structure in central Ethiopia and the associated magmatic activity. *Journal of African Earth Sciences* **26**(1):135-150.

Weissel, J. K. and Karner, G. D. (1989). Flexural uplift of rift flanks due to mechanical unloading of the lithosphere during extension. *J. geophys. Res* **94**(B10):13919-13950.

White, W. M. (2013). *Geochemistry*. John Wiley & Sons.

Wolfenden, E., Ebinger, C., Gezahegn Yirgu, Deino, A. and Dereje Ayalew (2004). Evolution of the northern Main Ethiopian rift: birth of a triple junction. *Earth and Planetary Science Letters* **224**(1):213-228.

Zanettin, B., Justin-Visentin, E., Nicoletti, M. and Petrucciani, C. (1978). The evolution of the Chencha escarpment and the Ganjuli graben (lake Abaya) in the southern Ethiopian rift. *Neues Jahrbuch fur Geologie und Palaonotologie,Monash* **8:**473-490.

Appendix I

Petrographic Analysis

Sample code RP-1 (NBS4,1-R1)				
Minerals	**Modal Proportion (%)**	**Phenocryst maximum grain Size (mm)**	**Phenocryst average grain shape**	**Rock name**
Porspaces	2			Aphanitic Rhyolite
Fe-Ti oxides	2	0.08	Anhedral	
Quartz	3	0.08	Anhedral	
Alkali feldspar	4	0.24	Subhedral	
Groundmass	99			

Sample code RP-2 ($NBS_{1,1\text{-}T}^{R}{}_{1}$)				
Minerals	**Modal Proportion (%)**	**Phenocryst maximum grain Size (mm)**	**Phenocryst average grain shape**	**Rock name**
Quartz	5	0.16	Subhedral	Porphyritic Rhyolite
Alkali feldspar	8	1.1	Subhedral	
Porespaces	9			
Groundmass	79			

Sample code RP-3 (NBS3,1-R3)				
Minerals	**Modal Proportion (%)**	**Phenocryst maximum grain Size (mm)**	**Phenocryst average grain shape**	**Rock name**
Olivine	1	0.15	Anhedral	Porphyritic Rhyolite
Porespaces	1			
Fe-Ti oxides	4	0.3	Anhedral	
Quartz	5	0.64	Subhedral	
Alkali feldspar	13	0.36	Subhedral	
Groundmass	77			

Sample code RP-4 (NBS4,1-B3)				
Minerals	**Modal Proportion (%)**	**Phenocryst maximum grain Size (mm)**	**Phenocryst average grain shape**	**Rock name**
Alkali feldspar	1	0.16	Subhedral	Porphyritic Basalt
Clinopyroxene	1	0.1	Anhedral	
Orthopyroxene	1	0.14	Anhedral	
Fe-Ti oxides	4	0.04	Anhedral	
Olivine	9	0.6	Anhedral	
Pore Spaces	16			
Plagioclase feldspar	31	1.5	Subhedral	
Groundmass	38			

Sample code RP-5 (NBS2,2-R2)				
Minerals	**Modal Proportion (%)**	**Phenocryst maximum grain Size (mm)**	**Phenocryst average grain shape**	**Rock name**
Quartz	4	0.2	Anhedral	Porphyritic Rhyolite
Alkali feldspar	7	0.42	Subhedral	
Fe-Ti oxides	7	0.08	Anhedral	
Porspaces	15			
Groundmass	68			

Sample code RP-6 (NBS5,1-B2)				
Minerals	**Modal Proportion (%)**	**Phenocryst maximum grain Size (mm)**	**Phenocryst average grain shape**	**Rock name**
Alkali feldspar	1	0.04	Subhedral	Porphyritic Basalt
Clinopyroxene	2	0.2	Anhedral	
Pore spaces	9			
Fe-Ti oxides	12	0.1	Anhedral	
Olivine	12	0.9	Subhedral	
Plagioclase feldspar	31	0.7	Subhedral	
Groundmass	33			

Sample code RP-7 (NBS5,1-B1)				
Minerals	**Modal Proportion (%)**	**Phenocryst maximum grain Size (mm)**	**Phenocryst average grain shape**	**Rock name**
Clinopyroxene	2	0.36	Subhedral	Porphyritic Basalt
Fe-Ti oxides	4	0.08	Anhedral	
Olivine	14	0.8	Subhedral	
Plagioclase feldspar	15	0.64	Subhedral	
Pore spaces	18			
Groundmass	48			

Sample code RP-8 (NBS4,1-I_1)				
Minerals	**Modal Proportion (%)**	**Phenocryst and Lithic fragment maximum grain Size (mm)**	**Phenocryst and Lithic fragment average grain shape**	**Rock name**
Clinopyroxene	1	0.14	Subhedral	Rhyolitic Ignimbrite
Orthopyroxene	1	0.2	Subhedral	
Fe-Ti oxides	2	0.14	Suhhedral	
Alkali feldspar	8	0.68	Subhedral	
Quartz	17	1.84	Anhedral	
Lithic fragment	20	1.9 (Basalt) & 1.2 (Rhyolite)	Anhedral	
Groundmass	52			

Sample code RP-9 (NBS3,1-R2)				
Minerals	**Modal Proportion (%)**	**Phenocryst maximum grain Size (mm)**	**Phenocryst average grain shape**	**Rock name**
Clinopyroxene	1	0.76	Anhedral	Porphyritic Rhyolite
Olivine	1	0.24	Anhedral	
Porespaces	3			
Fe-Ti oxides	3	0.16	Anhedral	
Alkali feldspar	9	0.36	Subhedral	
Quartz	9	0.84	Subhedral	
Groundmass	76			

Sample code RP-10				
Minerals	**Modal Proportion (%)**	**Phenocryst maximum grain Size (mm)**	**Phenocryst average grain shape**	**Rock name**
Orthopyroxene	1	0.36	Subhedral	Aphanitic Basalt
Alkali feldspar	1	0.44	Subhedral	
Pore spaces	4			
Olivine	5	0.98	Subhedral	
Fe-Ti oxides	15	0.08	Anhedral	
Plagioclase feldspar	24	0.64	Subhedral	
Groundmass	50			

Appendix II

Structural Data

Name		Orientation		Average spacing between consecutive flow bands (cm)	Lithological Unit
		Strike	Dip		
Flow Banding (Viscosity layering)	L1	235	60SE	0.2	Rhyolitic lava dome
	L2	285	50NE	1	Rhyolitic lava dome
	L3	280	70NE	2	Rhyolitic lava dome
	L4	355	40NE	2	Rhyolitic lava dome
	L5	240	20SE	2	Rhyolitic lava flow
	L6	080	20SE	2	Rhyolitic lava flow
	L7	130	89NE	3	Rhyolitic lava dome
	L8	030	88SE	1	Rhyolitic lava dome
	L9	330	89NE	1	Rhyolitic lava dome
	L10	020	35SE	1	Rhyolitic lava flow
	L11	0	65W	1	Rhyolitic lava dome

Name		Orientation		Aperture (cm)	Lithologic Unit
		Strike	Dip		
Joints	J1	065	89NW	0.1	Rhyolitic lava flow
	J2	150	85NE	0.3	Rhyolitic lava flow
	J3	120	85NE	2	Rhyolitic lava flow
	J4	030	80SE	21	Rhyolitic lava flow
	J5	040	85SE	5	Rhyolitic lava flow
	J6	120	85NE	24	Rhyolitic lava flow
	J7	040	70SE	60	Rhyolitic lava flow
	J8	090	85SW	4	Rhyolitic lava flow
	J9	075	80SE	0.1	Pumice fall
	J10	240	70SE	0.2	Pumice fall
	J11	050	50SE	0.2	Pumice fall
	J12	005	90	0.1	Pumice fall
	J13	195	85SE	0.2	Pumice fall

Name		Orientation		Rock Unit
		Strike	Dip	
	F1	010	85NW	Lower basalt
	F2	020	87NW	Lower basalt
	F3	030	70NW	Lower basalt
	F4	028	88NW	Rhyolitic lava dome
Faults	**F5**	030	87NW	Rhyolitic lava dome
	F6	035	60NW	Upper basalt
	F7	045	65NW	Upper basalt
	F8	040	89NW	Rhyolitic lava dome
	F9	020	88NW	Rhyolitic lava flow
	F10	026	70SE	Rhyolitic lava flow

Appendix III

Geochemistry Data

Major elements in elemental form (wt. %)

Calculated by a formula, Conversion Number*W_i; where W_i is the wt. percentages of oxide.

Conversion Number=MW_i*A_i/MW_g; where MW_i- molecular weight of cations, A_i- number of cations in the oxide formula and MWg are the molecular weight of oxide i.

	Ti	P	K	P/K	Ti/K
NBS4,1-B1	1.3129	0.144019	0.381874	0.377137	3.438119
NBS5,1-B2	1.372878	0.152747	0.556207	0.274622	2.468285
NBS2,1-S1	1.205015	0.157111	0.556207	0.282469	2.166486
NBS4,1-B2	1.139069	0.148383	0.83016	0.17874	1.372108
NBS2,1-B1	1.181035	0.152747	0.713938	0.21395	1.654255
NBS4,1-B3	1.157054	0.126562	0.763747	0.165712	1.51497
NBS5,1-B1	1.318922	0.183296	0.489794	0.374231	2.692807
NBS5,1-S1	1.013172	0.16584	0.481493	0.344428	2.104231
Conversion Number	0.59951	0.43642	0.83016		

Trace element ratio

	Rb/Sr	Ba/Y	Ti/Zr	$(La/Yb)_N$	Eu/Eu*	Y/Nb	La/Nb	Rb/Nb	Rb/Zr	Ce/Pb	La/Nb	Th/Ta
NBS2,2-R4	23.7	0.5	1.2	4.1	0.3	0.9	0.9	1.8	0.2	8.1	0.7	2.6
NBS2,2-R2	13.2	2.4	3.6	7.2	0.7	1	1	1.3	0.2	11.5	1.2	2
NBS2,2-R3	15.5	6.7	4.5	6.9	0.8	0.6	0.6	1.3	0.2	10.5	0.9	2
NBS1,1-TR1	21	3.1	3.9	6.5	0.7	1	1	1.3	0.2	11.9	1	2
NBS2,2-R1	8.5	5.4	3.7	6.5	0.7	0.7	0.7	1.4	0.2	12.5	0.9	2.1
NBS4,1-R1	25.4	0.3	1.6	5.7	0.3	0.6	0.6	1.4	0.2	7.9	0.6	2.3
NBS3,1-R3	10.6	7.5	2	7.6	0.3	0.8	0.8	2.3	0.2	7.2	1.2	3.2
NBS1,2-RT2	22.9	4.6	2.9	4.8	0.7	0.6	0.6	1.2	0.2	9.9	0.6	2.1
NBS3,1-R1	14.4	0.2	1.3	6.6	0.2	0.9	0.9	1.8	0.2	14.5	1	2.6

NBS3,1-R2	10.9	6.7	2.1	7.2	0.3	0.9	0.9	2.3	0.2	9.9	1.2	3.1
NBS2,2-O2	44.9	5.3	4.7	6.1	0.8	0.9	0.9	1.3	0.2	11.4	0.9	2
NBS4,1-O1	48.7	4.4	4.6	6	0.8	0.9	0.9	1.2	0.2	11.3	0.9	2
NBS1,2-O1	44.9	5.3	4.5	6.3	0.8	0.9	0.9	1.3	0.2	11.3	0.9	2
NBS2,2-O1	32.8	3.5	3.6	6.2	0.7	0.9	0.9	1.3	0.2	11.1	1	2.1
NBS4,1-i1	1.6	8.1	8.4	6.3	0.7	1	0.9	1.2	0.2	11.2	1	1.8
NBS2,2-i1	8.1	4.8	4.6	7.6	0.7	0.9	0.9	1.2	0.2	11.7	1.2	2
NBS1,1-P2	4.9	3.4	3.8	6.2	0.7	0.9	0.9	2.7	0.4	11	0.9	2.1
NBS1,1-P1	6.6	3.8	3.9	6.2	0.7	0.9	0.9	2.1	0.3	11	1	2.1
NBS2,2-P1	1.1	14.6	6.3	8.7	0.4	0.7	0.7	3	0.3	6.5	1.2	3.8
NBS2,2-P2	8.1	3.8	3.2	7.4	0.7	1	1	1.8	0.3	11.2	1.2	2.2
NBS4,1-P1	1.4	3.8	1.9	6.1	0.8	0.9	0.8	0.8	0.1	14.2	0.8	1.5
NBS1,2-P1	21.2	3.3	3.8	6.4	0.7	1	1	1.8	0.2	10.9	1	2.1
NBS4,1-B1	0.01	10.9	98.3	6.2	1.1	1	1	0.1	0.02	17.3	0.9	1.2
NBS5,1-B2	0.02	13.2	119.1	5.5	1.1	1.1	1.1	0.4	0.1	10.2	0.9	1.2
NBS2,1-S1	0.02	12	97.1	6.2	1.1	1	1	0.5	0.1	16	0.9	1.3
NBS4,1-B2	0.03	19.8	82.7	6.4	1.1	1.2	1.2	0.8	0.1	10	1.1	1.7
NBS2,1-B1	0.03	15.2	94.7	6.3	1.1	1	1	0.6	0.1	15.3	0.9	1.3
NBS4,1-B3	0.03	12.4	91	5.6	1.1	1.1	1.1	0.7	0.1	15.2	0.9	1.5
NBS5,1-B1	0.02	12.3	122.6	5.9	1.1	1.2	1.2	0.4	0.1	17.2	0.9	1.1
NBS5,1-S1	0.03	11.1	108	4.9	1.1	1.2	1.2	0.7	0.1	12.2	0.9	1.2

Molecular CIPW norm of the samples (in wt. %) and Agpaitic Index (AI)

	Albite	**Diopside**	**Hypersthene**	**Quartz**	**Olivine**	**Nepheline**	**AI**
NBS2,2-R4	28.85	0.54	7.22	32.97	0	0	1.26
NBS2,2-R2	32.33	0.7	11.47	24.03	0	0	1.27
NBS2,2-R3	32.86	1.56	9.87	22.19	0	0	1.09
NBS1,1-TR1	31.13	1.55	9.96	24.45	0	0	1.06
NBS2,2-R1	28.64	2	10.18	26.74	0	0	1,08

NBS4,1-R1	24.05	1.29	8.87	34.49	0	0	1.02
NBS3,1-R3	41.55	0.66	3.74	23.04	0	0	1.37
NBS1,2-RT2	26.12	1.51	10.93	31.02	0	0	1.14
NBS3,1-R1	28.31	0.98	6.86	32.79	0	0	1.29
NBS3,1-R2	41.8	0.98	3.81	22.56	0	0	1.36
NBS2,2-O2	32.34	1.39	9.59	23.66	0	0	1.03
NBS4,1-O1	30.69	1.38	10.04	24.03	0	0	1
NBS1,2-O1	32.13	1.39	9.54	23.6	0	0	1.02
NBS2,2-O1	27.25	1.42	10.13	27.61	0	0	1.04
NBS4,1-i1	41.92	4.75	8.14	15.86	0	0	1.28
NBS2,2-i1	29.48	3.73	9.74	23.77	0	0	1.03
NBS1,1-P2	16.92	0	12.16	34.65	0	0	1.63
NBS1,1-P1	13.79	0	12.89	32.67	0	0	1.65
NBS2,2-P1	14.72	0	7.59	32.01	0	0	2.14
NBS2,2-P2	14.81	1.74	10.31	31.12	0	0	1.22
NBS4,1-P1	14.7	17.62	6.17	26.84	0	0	0.81
NBS1,2-P1	15.82	0	11.3	32.1	0	0	1.34
NBS4,1-B1	18.13	13.99	0	0	24.05	1.73	
NBS5,1-B2	22.29	17.98	0	0	20.03	0.12	
NBS2,1-S1	22.4	17.92	0	0	21.66	0.1	
NBS4,1-B2	25.38	15.88	4.92	0	15.72	0	
NBS2,1-B1	23.27	16.69	1.37	0	19.54	0	
NBS4,1-B3	26.32	13.87	4.47	0	14.05	0	
NBS5,1-B1	18.76	21.21	0	0	21.21	1.98	
NBS5,1-S1	19.46	21.7	2.74	0	19.48	0	

Appendix IV

Soil CO_2 Concentration and Flux Data

Way Pts.	Easting (m)	Northing (m)	Concentration (ppm)	Flux ($g\ m^{-2}\ d^{-1}$)
12_15	537667	933560	423	0
TA_1	538186	933582	408	0
TA_4	539022	933022	395	0
TA_20	539036	939056	402	0
TA_22	539047	941091	400	0
TA_28	538167	938033	405	0
19	537171	935036	418	0
TA_39	536120	940081	412	0.038016
TA_42	535102	940074	413	0.038016
TBA_6	535667	933568	419	0.038016
10_13	536697	933609	412	0.038016
TBA_10	534617	936047	420	0.038016
74	532006	940080	432	0.038016
94_95	534593	942004	410	0.038016
95	535093	942018	421	0.038016
86	535104	941094	415	0.038016
TA_37	536123	942012	418	0.076032
TA_38	536123	941090	410	0.076032
TA_40	536129	939068	415	0.076032
TA_43	535118	939071	412	0.076032
33	534094	936045	419	0.076032
TBA_13	534571	940748	413	0.076032
76	534088	940081	415	0.076032
67	533068	939089	411	0.076032
TBA_14	532444	939086	402	0.076032
8	535151	933036	435	0.114048
12	537194	933028	406	0.114048
TA_14	536675	935045	419.7	0.114048
TA_35	537131	941089	406	0.114048
TA_44	535126	938064	408	0.114048
9_21	535148	934551	422	0.114048
TA_36	537132	942024	415	0.152064
TA_41	536136	938053	421	0.152064
TA_45	535126	937042	411	0.152064
11_19	536648	934593	427	0.152064
TA_6	538180	934569	409	0.19008
TA_15	536149	935590	418.5	0.19008

TA_31	536143	937052	420	0.19008
TA_52	532038	933063	401	0.19008
TBA_7	535670	933933	429	0.19008
9_11	535645	934051	432	0.19008
20	536157	935045	414	0.19008
11	536164	934038	409	0.19008
11_13	536695	934041	412	0.19008
34	535141	936042	406	0.19008
86_95	535097	941531	408	0.19008
3_24	532038	934592	426	0.19008
13_15	537693	934021	409	0.228096
TA_58	531061	935072	420	0.228096
TA_65	531046	939098	421	0.228096
9	535153	934055	435	0.228096
9	535670	934572	431	0.228096
35	536144	936038	423	0.228096
TA_33	537144	939052	410	0.266112
TA_48	534092	939080	417	0.266112
TBA_8	532033	934071	402	0.266112
19_18	537717	935030	435	0.304128
21	535140	935054	443	0.304128
18	538173	936039	438	0.342144
TBA_9	537181	933625	401	0.342144
54_55	533573	938067	434	0.342144
10	536163.1	933037.7	398	0.38016
TBA_4	538195	934018	409	0.38016
TA_5	539018	934021	401	0.38016
TA_8	539025	935016	401	0.38016
TA_18	539035	937038	403	0.38016
TA_23	539041	9342024	401	0.38016
TA_26	538144	940072	406	0.38016
TA_29	538167	937043	401	0.38016
TBA_15	530892	937546	436	0.38016
TA_49	533073	940049	437	0.418176
13_18	537726	934568	441	0.418176
008_9	535157	933546	448	0.418176
11_20	536148	934564	412	0.418176
19_13	537175	934557	397	0.418176
13	537187	934037	394	0.456192
31	532029	936058	443	0.456192
24	532033	935063	440	0.456192
TBA_1	537178	932516	404	0.494208
TA_34	537134	940078	404	0.494208

TA_46	534097	937061	436	0.494208
TA_57	534105	935048	439	0.532224
47_52_2	531051	937652	444	0.57024
10_12	536679	933034	399	0.608256
TA_50	534083	941102	442	0.608256
92	533064	941999	438	0.608256
TBA_17	530733	937518	448	0.608256
54_67	533064	938657	463	0.646272
TBA_29	529552	936879	449	0.684288
2	531067	934081	449	0.684288
54	533072	938075	454	0.722304
TBA_37	533582	937591	456	0.722304
TBA_43	531802	935352	462	0.722304
8 _10	535662	933037	478	0.76032
TA_2	538194	933015	400	0.76032
TA_9	539028	936044	405	0.76032
TA_19	539033	938041	401	0.76032
TA_21	539040	940079	403	0.76032
TA_24	538134	942025	398	0.76032
TA_25	538131	941087	407	0.76032
TA_27	538153	939056	403	0.76032
TA_32	537150	93804	450	0.76032
TA_47	534093	938067	432	0.76032
TA_53	533076	935064	450	0.76032
94	534082	942009	446	0.76032
TBA_47	532551	935430	452	0.798336
TBA_18	530640	937397	493	0.836352
48_47	530516	937066	468	0.836352
TBA_24	530559	936662	453	0.836352
TBA_40	531926	936097	464	0.836352
TA_54	533007	936065	441	0.874368
TA_56	534106	934054	453	0.874368
10_11	536157	933617	380	0.874368
TBA_44	532033	935063	476	0.874368
TBA_36	533518	938669	510	0.912384
TA_51	533080	934065	470	0.9504
TBA_11	533069	941579	458	0.9504
TBA_12	533515	941599	455	0.9504
TBA_31	529660	935498	458	0.9504
TBA_45	532233	935244	459	0.9504
TBA_42	531692	935523	469	0.988416
TA_17	536754	935560	413.9	1.026432
TBA_33	532538	934564	467	1.026432

TBA_46	532348	935321	468	1.064448
TA_10	538177	935574	470	1.102464
26	530056	935077	464	1.102464
TA_3	538612	933025	399	1.14048
TA_30	537159	937032	400	1.14048
TBA_3	537678	933017	477	1.178496
TBA_25	530185	936631	480	1.178496
TBA_19	530593	937337	483	1.216512
TBA_30	529506	936662	472	1.216512
45	533069	937057	477	1.216512
TBA_22	530606	936724	512	1.254528
TA_59	530049	936053	481	1.292544
TBA_41	531541	936069	484	1.33056
TBA_2	537678	933017	491	1.406592
TA_13	537734	935558	423.8	1.406592
88	533066	941109	491	1.482624
24_31	531630	935647	495	1.482624
TA_61	531047	938063	465	1.52064
TA_16	536685	936037	411	1.596672
TBA_35	532897	937734	495	1.596672
TBA_32	530117	934967	498	1.634688
TBA_5	538192	935036	502	1.824768
TA_55	532020	937060	513	1.9008
TA_62	531739	938073	460	1.9008
TA_64	530042	939091	530	1.9008
TBA_26	529809	937266	541	2.128896
TBA_27	529730	937545	532	2.166912
TBA_38	533071	937583	530	2.242944
TA_60	531057	937060	490	2.28096
TA_63	530038	938082	525	2.28096
TBA_28	529793	937856	531	2.395008
TBA_34	532558	937557	567	2.47104
TA_12	537164	935564	408	2.927232
20_19	537163	936044	399	2.927232
48	530047	937059	452	3.079296
TA_11	537715	936033	418	3.269376
TBA_39	532606	937064	583	3.345408
TBA_23	530544	936739	614	3.725568
TBA_20	530537	937211	790	6.994944
TBA_21	530527	937155	952	10.606464